

Advances in zeolite imidazolate frameworks (ZIFs) derived bi-functional oxygen electrocatalysts and their application in zinc-air batteries

Yasir Arafat^a, Muhammad Rizwan Azhar^{a,b}, Yijun Zhong^a, Hussein Rasool Abid^{a,b}, Moses O. Tadé^a, Zongping Shao^{a, c,*}

^aWA School of Mines: Minerals, Energy and Chemical Engineering (WASM-MECE), Curtin University, Perth, WA 6102, Australia.

^bSchool of Engineering, Edith Cowan University, 270 Joondalup Drive, Joondalup, WA 6027 Australia.

^cState Key Laboratory of Materials-Oriented Chemical Engineering, College of Chemical Engineering, Nanjing Tech University, Nanjing 211816, China.

*Corresponding author. E-mail: zongping.shao@curtin.edu.au

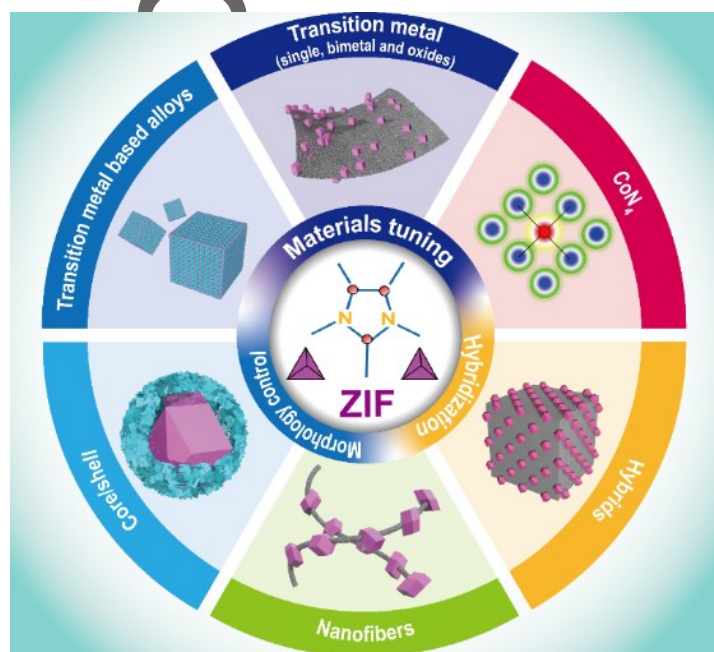
Abstract

Secondary Zn-air batteries (ZABs) are recognized as the one of the most promising power sources for the future with lucrative features of low cost, high energy density, non-flammable, eco-friendly, and high safety. However, the widespread implementation of the secondary ZABs in our daily life is still hampered by the sluggish oxygen redox reactions (oxygen evolution/reduction reactions) and expensive air electrodes. The deployment of cost-effective and highly efficient air electrodes to substitute the precious metals (Pt/Ir), is highly challenging, however, most-wanted. Zeolitic Imidazolate Frameworks (ZIFs), a subclass of metal organic frameworks, are an emerging functional materials, which demonstrate several outstanding features like high surface area, high conductivity (upon pyrolysis), open pore structure, more exposed facets, versatile compositions (C, N, transitional metal elements,...), homogeneous distribution of the elements inside the frameworks on atomic scale, and favourable chemical stability. Through varying the metal centres or organic moiety and by employing different synthesis protocols, ZIFs with fairly different properties could be obtained. As the ZIFs are adaptable so desired functionalities may be further indoctrinated into ZIFs through pre-treatment, in-situ treatment, and post treatment. Thus, ZIFs are ideal precursors or the starting materials for the preparation of variety of bi-functional air electrodes for ZABs by materials tuning, morphological control, or materials compositing. As a result, multiple useful compositions and favourable morphologies have been developed using ZIFs precursors. Here, the recent advances of ZIFs-based materials is critically surveyed with the perspective of synthesis, morphology, structure and properties, and correlated them with performance indicators of ZABs. Finally, the major challenges and future prospects of ZIFs linked with the application in the ZABs are discussed.

This is the author manuscript accepted for publication and has undergone full peer review but has not been through the copyediting, typesetting, pagination and proofreading process, which may lead to differences between this version and the [Version of Record](#). Please cite this article as [doi: 10.1002/aenm.202100514](https://doi.org/10.1002/aenm.202100514).

This article is protected by copyright. All rights reserved.

Keywords: Zeolitic Imidazolate Frameworks (ZIFs), Metal Organic Frameworks (MOFs), transition metals, air electrode, oxygen reduction reaction (ORR), oxygen evolution reaction (OER), Zn-air batteries (ZABs)



1. General introduction

The fast growth in human population and the quick cultural advancement of human society leads to the tremendous increase in energy demand.^[1] During the past, fossil fuels were used as the main energy sources, while their excessive use based on the conventional combustion technology releases excessive greenhouse gases into the environment, causing adverse impact on the sustainability of ecosystem. To cope with the challenges of stringent environmental legislations and the reliance on fossil fuels, renewable energies, viz., wind and solar, which are more sustainable, have come forward to power the next generations. Therefore, photovoltaic systems and wind-turbine generators have been coupled with the power grids to harness the “green” electricity.^[2] Despite their ubiquitous availability, the renewable energies are intermittent. Therefore, it is imperative to integrate some appropriate energy storage systems (batteries) into the grid infrastructure for the storage of harvested energy and to even out the energy fluctuations. Nevertheless, the stored energy from a battery-integrated grid holds a minor share of just 30 min in comparison to the 46 days obtained from oil storage. It implies that the energy storage capacity from a battery integrated grid is 2000 folds smaller in contrast with the oil storage.^[3] Moreover, it is also projected that the application of multiple storage systems may rise to 17 times higher than the current scenario by 2030.^[4] Consequently, it is

inevitable to develop some leapfrog strategy in the energy storage systems to substitute the fossil fuels and to meet the future demands.^[5]

Considering the pros and cons, Zn-air batteries (ZABs) have garnered a great deal of attentions because of their high energy and power density as a result of free-oxygen supply from the surrounding air and high capacity of metallic zinc anode.^[6] Theoretically, the reversible energy density of ZABs can reach as high as 1085 Wh kg⁻¹, which is fivefold larger in contrast with traditional Li-ion batteries (200–250 Wh kg⁻¹). In addition, ZABs are cost effective, hazard-free, and environmentally benign.^[6e, 7] Regardless of above mentioned merits, commercialization of ZABs was obstructed by the inadequate energy conversion efficiency and short lifespan.^[8] In fact, these deficiencies stemmed from the intrinsically sluggish kinetics of the air electrode for both oxygen reduction reaction (ORR) and oxygen evolution reaction (OER), that are happened during the cell discharge and charge processes, respectively. To surpass the energy barrier, the incorporation of efficient bi-functional electrocatalysts into air electrode that can effectively promote the OER and ORR over the air electrode is critical, and thus highly wanted.^[9]

In the early stages, precious metals like Pt as ORR electrocatalysts and ruthenium or iridium oxides as OER electrocatalysts had been extensively employed in air electrode for ZABs to achieve the bi-functional activities. However, due to high price and scarcity, these precious metals do not comply the commercial requirement of electrocatalysts for ZABs. In addition, such electrocatalysts show insufficient cyclic stability. Therefore, it is inevitable to devise some alternative bi-functional electrocatalysts for ZABs, which should have high activity for both OER and ORR, superior durability and low cost. Carbonaceous materials (for instance, carbon nanotubes, graphene and porous carbon) are recognized as promising electrode materials out of their lucrative properties, like large surface area, high electronic conductivity and reasonable electrochemical durability.^[10]

Metal organic frameworks (MOFs) are emerging materials constructed from the metal nodes and organic moiety that are bridged in a three-dimensional porous network extending from microporous to mesoporous.^[11] Due to their well-organized porous architecture, exceptionally large surface area, high porosity, low density and high electrical conductivity (upon carbonization),^[12] MOFs are preferred over other porous carbon-based materials and zeolites for various applications, such as gas adsorption and storage, waste water treatment, catalysis, sensing, energy conversion and storage, etc. Moreover, MOFs are highly flexible in compositions, which can be fine-tuned to achieve the desired features. On the basis of these characteristics, MOFs qualify for electrochemical applications, in particular for batteries. During the last decade, a plethora of research activities have been conducted on MOFs towards the applications in batteries. It is also reflected from **Fig. 1a**, that the integration of MOFs-based electrocatalysts in the batteries has been progressively rising. Notably,

zeolitic imidazolate frameworks (ZIFs), as the prominent class of MOFs, are prioritized for the electrochemical applications. Upon the pyrolysis, ZIFs generate metal-nitrogen bonds and nitrogen-doped porous graphitic carbon network. This self-doped nitrogen provides additional properties, which are lucrative for electrochemical applications. Therefore, ZIFs may be regarded as the ideal starting materials for the development of positive electrodes for batteries, including ZABs. Actually, in the last decade, ZIFs have also been tremendously employed in the batteries and continuously pursued a rising trend (**Fig. 1b**), yet there is a huge potential for applying ZIFs derived materials in ZABs. As metal doped carbon, nitrogen doped carbon together with high surface area and graphitic carbon tend to be favourable for catalyzing both OER and ORR, ZIFs are considered as the most suitable precursors for the development of efficient air electrode for ZABs.

Herein, we present an in-time comprehensive overview of the recent advances in the development of diverse oxygen electrocatalysts with versatile compositions derived from ZIF-based precursors, and their applications as air electrode for ZABs are emphasized. By virtue of flexibility, ZIFs precursors have been adapted into variety of compositions including N, P, S non-metal elements doped metal-free carbon, transition metal doped carbon, single atom modified carbon, alloy/ carbon composite, transition metal oxide/carbon composite, and CoN_4 /carbon composite, and different morphological structures, such as core-shell structures, and nonwoven nanofibers, as air electrodes for ZABs to achieve the customized functionalities. As well, the development of bifunctional electrocatalysts by forming ZIFs hybrid materials as air electrode of ZABs was also provided. As the ZIFs transformation into various compositions depends on synthesis conditions and synthesis strategies, therefore, a special emphasis was given to present a synopsis of synthesis strategies and their correlation with electrocatalytic performance and ZABs. This comprehensive overview also showcases the major synthesis conditions for the ZIF-derived materials and performance indicators of ZABs for those materials. Finally, the main challenges and future perspectives of ZIFs associated with the application in the ZABs are discussed. Obviously, this comprehensive overview would assist the researchers to identify the literature gap and to rationally design the ZIFs based optimal oxygen electrocatalyst in terms of high activity and favourable durability.

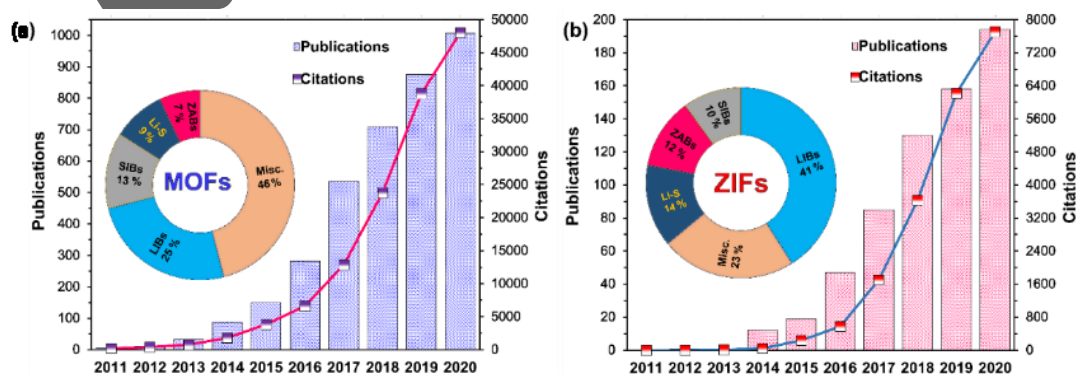


Fig. 1 Number of publications and citations pertaining to (a) metal organic frameworks (MOFs) and (b) zeolitic imidazolate frameworks (ZIFs) for their application in the batteries in the last decade according to the Web of Science (Keywords: (a) Metal organic framework OR MOFs; Batteries (b) Zeolite imidazolate framework OR ZIFs; Batteries). LIBs: Li-ion batteries, SIBs: Sodium-ion batteries, Li-S: Li-sulphur batteries, Misc: Miscellaneous (Inset).

2. Zn-air Batteries, oxygen electrocatalysis, Metal-organic frameworks and Zeolite imidazolate framework

2.1 Zn-air Batteries

Zinc (Zn) is recognized as the fourth plentiful and accessible element in the earth's crust, which constitutes about 300 times larger reserves of Zn in contrast with lithium.^[13] Furthermore, the charging efficiency of Zn is higher with low self-discharging in comparison with aluminium and magnesium-air batteries. It is worth noting that Zn is entirely recyclable, which is an added advantage. On account of inexpensiveness, high energy density, cell voltage, electrochemical reversibility, environmental benignity and inherent safety features in comparison with Mg-air batteries, Li-air batteries and Al-air batteries, Zn may be considered as the most feasible anode material for the development of metal air batteries.^[7a, 14] The production cost of Zn-air batteries is around 10\$ per kwh, which also enhances their attractiveness with respect to the commercial perspective.^[8a]

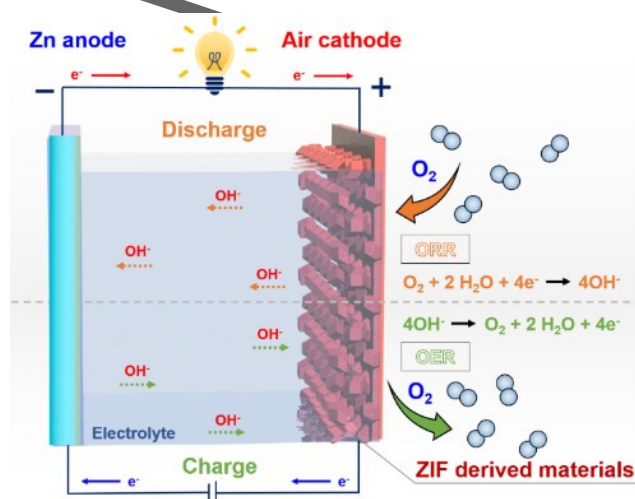


Fig. 2 Schematic of battery assembly configurations and illustration of equations of ORR and OER

2.1.1 Assembly of Zn-air batteries

Secondary Zn-air batteries are assembled by three major parts: air electrode (cathode); Zn metal (anode), and an aqueous alkaline solution (electrolyte) (**Fig. 2**). Air electrode is usually comprised of bilayer, a hydrophilic electrocatalyst layer and a hydrophobic gas diffusion layer.^[15]

This article is protected by copyright. All rights reserved.

Active catalyst is loaded on one side of air electrode with the aid of binding agent. Conductive carbon is also sometimes added in the active catalysts, in case of non-conductive catalysts for enhancing the electronic conductivity. The Zn anode is integrated in the Zn-air assembly as a Zn plate or Zn powder loaded on the electron conducting support. Considering Zn plate undergoes violent reaction and leads to the corrosion in acidic electrolyte, KOH, NaOH and LiOH are generally employed as electrolytes in ZABs.^[16] In most of the cases, 6M KOH solution is favoured as an electrolyte in ZABs because of its compatibility with Zn anode and air electrode containing active catalyst. Meanwhile, KOH electrolyte has low viscosity and high ionic conductivity. The aqueous alkaline electrolyte renders an ionic conductivity of OH⁻ corresponding to 620 mS cm⁻¹.^[17] As the concentration of KOH increases, so does the solubility of ZnO.^[18] Subsequently, the higher concentration of ZnO may lead to generation of surplus Zn(OH)₂⁻⁴ ions, precipitates following the discharge and accelerates the passivation resistance of Zinc anode. Therefore, the optimum concentration of KOH is critical for the reversible restoration of Zn anode. Consequently, a little amount of zinc chloride or zinc acetate is also added into the solution to help the reversible re-deposition of Zn plate (anode).^[19]

2.1.2 Working principle of Zn-air battery

During discharging of ZABs, O₂ from surrounding air diffuses into the air electrode as driven by the difference in atmospheric oxygen partial pressure between external and internal cell; the reduction of O₂ to OH⁻ takes place at three phase boundary (air, electrocatalyst and aqueous alkaline electrolyte solution) with electrons supplied from external circuit on the catalyst surface.^[20] Subsequently, the generated OH⁻ ions migrate to the Zn anode, yielding the soluble Zn(OH)₄²⁻ (zincate) ions till the supersaturation point is reached in the electrolyte. Upon supersaturation, zincate ions spontaneously transform into zinc oxide (ZnO), which are insoluble.

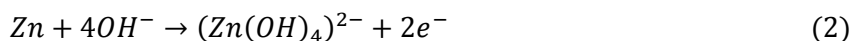
Chemical reactions inside the ZABs during discharging are as follows:^[21]

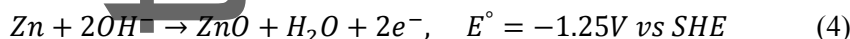
At air electrode (cathode):



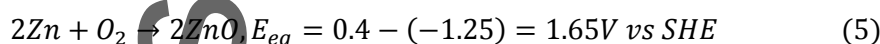
Generally, oxygen reduction undergoes a four electron reaction. However, some detrimental reactions may also occur, leading to the generation of superoxide via two-electron pathway.

At Zn electrode (anode):





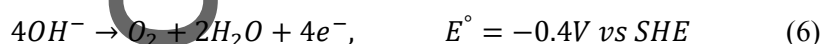
From Eq. (1) and Eq. (4), Overall reaction is described as follows:



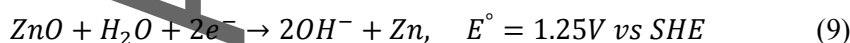
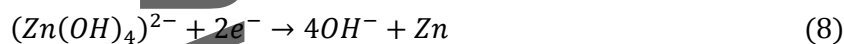
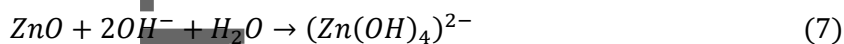
During recharging in the ZABs, the entire phenomenon is reversed accompanied by the evolution of oxygen, thus constituting oxygen evolution reaction (OER). ZnO is converted (reduced) to metallic Zn and deposited back to anode. Wang and co-workers ratified the reversibility of the process by in situ Raman spectroscopy. It can be visualized that an intensifying peak arises at around 413 cm^{-1} in the course of discharging, attributing to the gradual formation of ZnO as illustrated by **Fig.3** (b).^[22] While, this particular peak progressively diminishes upon charging. It is worth mention that reduced Zn does not necessarily deposit exactly on the same place where it had been oxidized. Therefore, it may result in a change of morphologic shape of the Zn anode.^[23]

Charging reactions are as follows:

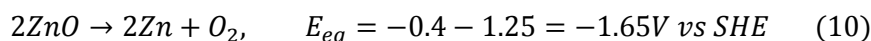
At air electrode (cathode):



At Zinc electrode (anode):



From Eq. (6) and Eq. (9), Overall reaction reaches:



This article is protected by copyright. All rights reserved.

Poisoning of electrolyte by carbonate generation ^[24]



Some parasitic reaction on Zn anode may also occur as follows:

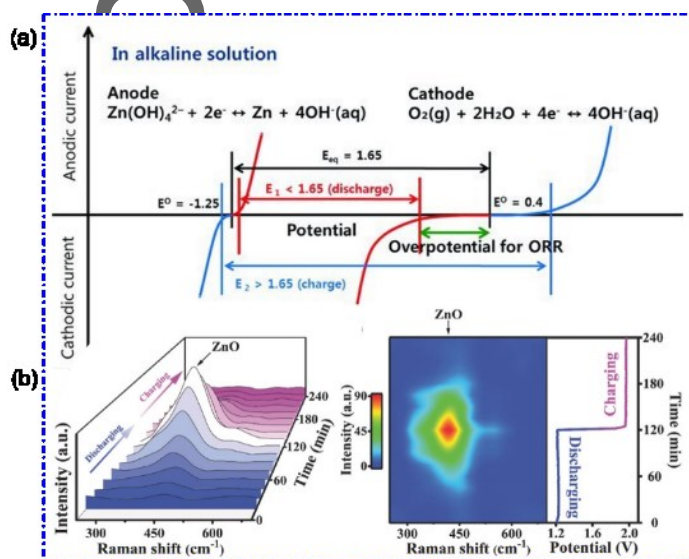


Fig.3 (a) Schematic of polarization curves of zinc-air batteries. The equilibrium potential of the zinc-air cell. The equilibrium potential of ZABs corresponding to 1.65 V (black line), whereas the real voltage during discharging is less than 1.65 V because of sluggish ORR (red line). A large potential is required to charge zinc-air, higher than the equilibrium potential (blue line). Reproduced with permission. ^[25], copyright 2011, Wiley - VCH. (b) In situ Raman spectroscopy patterns and contour plot of zinc-air batteries during charging/discharging. Reproduced with permission. ^[22], copyright 2018 Wiley - VCH.

Fig. 3 (a) illustrates the typical potential-current polarization curve, which manifests the origin of potential losses during oxygen electrocatalysis in a secondary ZAB. ^[25] The theoretical electrochemical equilibrium window is represented by the black vertical lines. It is clear that equilibrium potential of the ZAB should be $E_{eq} = E^0$ (cathode) $- E^0$ (anode) = 1.65 V (Black line). However, in the course of discharging (red line), the actual working potential (E_1) corresponding to <1.65 V. The potential drop may be associated with the activation, ohmic and concentration losses. ^[15] Resultantly, a high overpotential (green line) is required to produce OH^- ions from O_2 by ORR. In comparison, at anode, a little overpotential is sufficient to overcome the resistance of chemical potential state and to activate the zinc oxidation reaction. Thus it implies that overpotential is significantly higher than the open - circuit voltage (E_{eq}) at the cathode as a result of sluggish ORR kinetics. In the course of charging, a larger overpotential (E_2) (Blue line) is still required for the generation of O_2 at air electrode by OER. It is worth mention that a little bit larger overpotential is

required for the regeneration of Zn at anode in contrast with the discharging at anode. This may be accounted for the thermodynamically stable state of zincate intermediates and ZnO, which implies that a larger energy is required to activate the reverse reaction for Zn regeneration.^[26] In a nutshell, the overpotential while charging and discharging at cathode is way bigger in contrast to the one at anode, which implies that the development of some efficient air electrode (cathode) is more crucial for achieving oxygen redox reaction and eventually high performance of ZABs.

On the other hand, ZABs also come across with some fundamental challenges in the course of discharging as well as charging, which deteriorate the performance of ZABs, for instance, hydrogen evolution reaction, passivation, dendrite formation and shape change (Fig. 4 b). Besides, ambient conditions also cause a strong influence on the performance of ZABs, for instance, dry air can expedite the evaporation of electrolyte, whereas excessive humidity in the air may become liable for the flooding of air electrode.^[27]

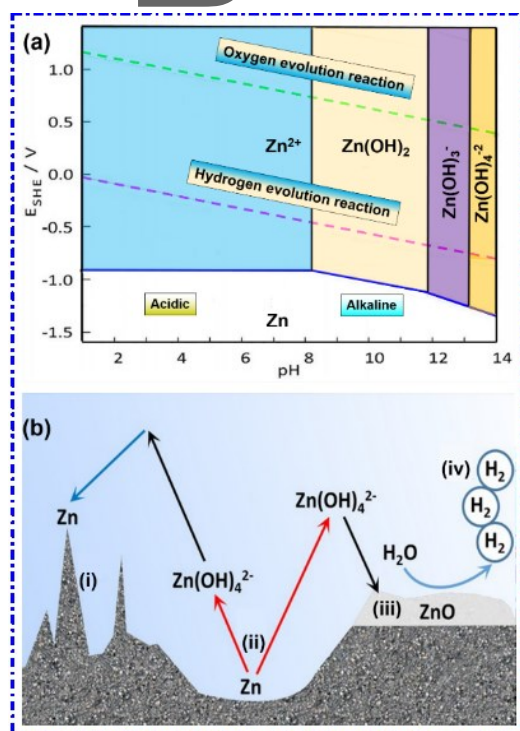


Fig. 4 (a) Pourbaix diagram for zinc–water in electrolyte system as a function of pH in aqueous solution. Adapted with permission^[28], Copyright 2021, Elsevier Ltd. (b) Schematic illustration of performance - limiting issues: (i) dendrite formation, (ii) change of shape, (iii) passivation, and (iv) HER. Reproduced with permission^[29], Copyright 2016, WILEY - VCH.

Briefly, hydrogen evolution reaction (HER) refers to the creation of hydrogen during reaction at zinc anode. In alkaline solution, the redox potential of HER is corresponding to -0.83 V vs. SHE. In comparison, the redox potential of Zn/ZnO (-1.26 V vs. SHE) is less positive, which implies that HER ($Zn + 2H_2O \rightarrow Zn(OH)_2 + \uparrow H_2$) is more thermodynamically feasible in alkaline solution during

recharging cycle.^[30] It is also obvious from the Pourbaix diagram (**Fig. 4a**) that the redox potential of HER is more positive in contrast to zinc, eventually HER dominates over zinc redox potentials. Thus the occurrence of HER causing the corrosion of Zn electrode, generating corrosion product i.e. Zn(OH)₂ and self-discharge of ZABs. Moreover, HER results in the rise in internal pressure, causing the internal swelling and the leakage of electrolyte.^[31] During the charging operation, HER also induces the consumption of electrons, leading to the drop in coulombic efficiency in rechargeable ZABs.^[32]

Dendrite formation is also a major performance-limiting issue. Zinc dendrites are needle-like protrusions of zinc metals which develops as an outcome of electrodeposition during charging mode, may pierce through the separator to the air electrode and ended up into the short-circuit. As a result, it may lead to the drop in cyclic life and overall performance of rechargeable ZABs. Moreover, zinc dendrites are likely to be fragmented and alienated from zinc electrode and causing the capacity losses.^[29]

Shape change of zinc anode is another challenging issue, posing the zinc-anode failure. Shape change is the consequence of spatial redistribution of Zn, when zinc re-deposits (while charging) at some different location after the dissolution of zinc (while discharging). This phenomenon is resulted because of random motion of zincate ions in aqueous electrolyte and non-uniform distribution of current.^[34]

Passivation is defined as the formation of insulating and insoluble film over the electrode surface, which in turn causing an extra resistance and rendering the surface incapable of further discharging. Specifically, when zincate (Zn(OH)₄²⁻) ions as discharging product reached the supersaturation, these ions were transformed into ZnO (**Eq. 2 and 3**). These ZnO precipitates deposited back to the Zn anode surface and inhibiting the transportation of Zn(OH)₄²⁻ and/or OH⁻ ions. Even in the porous Zn electrodes, ZnO precipitates being larger in volume in contrast to the Zn, clog the porous channels. Consequently, Zn anode is not fully utilized and causing the decline in actual energy density (220–300 Wh kg⁻¹), markedly less than the theoretical energy density (1086 Wh kg⁻¹).^[30]

2.2 Oxygen electrocatalysis

Rechargeable ZABs utilize O₂ from air for the electrochemical reactions at the air electrode, governed by two critical electrochemical redox reactions in aqueous alkaline solution, namely ORR during discharging and OER during charging.

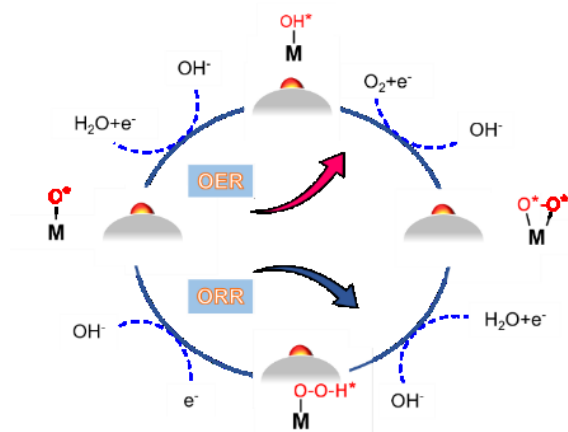
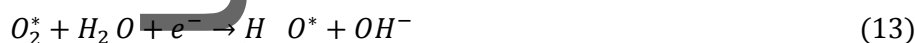
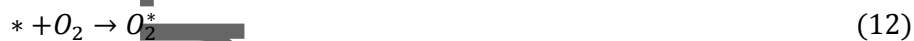


Fig. 5 OER (anticlockwise) and ORR (clockwise) mechanisms.

2.2.1 Oxygen reduction reaction (ORR)

ORR occurs over the air electrode during discharging, which is accomplished by two pathways: two-electron ($2e^-$) pathway or four-electron ($4e^-$) pathway, leading to the two different end-products, HO^{2-} or OH^- respectively. $4e^-$ pathway is preferred over $2e^-$ pathway because $2e^-$ is indirect pathway, leading to the intermediate peroxide products, posing some adverse effects, such as low energy efficiency and instigating the instability due to the high oxidizability of peroxides with high tendency to corrode the carbon-based materials.^[13, 33] Therefore, $4e^-$ dominant pathway is projected as an optimal way of accelerating the O_2 electrocatalysis. In ZABs, ORR activity on air electrode is undertaken by the following steps (**Fig.5**, ORR: clockwise): (i) the diffusion of O_2 through the oxygen permeable cathode layer and adsorption on catalyst containing cathode layer; (ii) the transmission of electrons from Zn anode through external circuit to O_2 , activation and cleavage of the O–O bond leading to the reduction of O_2 at the catalyst/oxygen interface; (iii) hydration and desorption of reduced product (OH^-) via alkaline electrolyte to Zn anode.^[34] ORR activity is hard to ensue because of large bond energy (498 kJ mol^{-1}), which necessitates $4e^-$, consisting of a series of complicated reactions.^[35] Following equations represent the typical ORR mechanism, generally proceed on the metal-based catalysts.

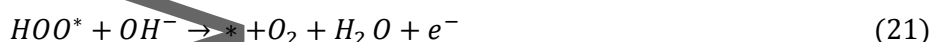


Overall reaction:



2.2.2 Oxygen evolution reaction (OER)

OER is another half reaction and actually a reverse of ORR (**Fig. 5**, OER: anti-clockwise), which is critical reaction in rechargeable ZABs.^[36] In alkaline solution, the evolution of oxygen reaction is accomplished by the transformation (oxidation) of OH^- ions to one molecule of O_2 and two molecules of H_2O with the release of $4e^-$. The transfer of four electrons is not kinetically feasible in a single step, therefore, four electrons are transferred sequentially in four steps.^[9b] The equilibrium potential essential to promote the OER is 1.23V. However, the actual working potential during charging is larger than 1.23V, leading to the energy loss. As OER process is opposite to ORR, therefore, mechanistic steps of OER are represented by the reverse of ORR (Eq.18-22), where HO^* , O^* , HOO^* , and O_2^* indicate oxygen intermediates.



Overall reaction:



As the overpotential at cathode during ORR (discharging) as well as OER (charging) is higher in contrast with the anode (**Fig. 3**). Consequently, the cathode/air electrode plays a major role in deciding the recharge-ability and cyclic stability of ZABs. Therefore, it is inevitable to deploy some efficient air electrode with well-designed architecture, which is capable of suppressing the overpotential (OER/ORR) and catalyze the oxygen electrochemical reactions. Porous carbons have arisen as the most promising materials which can be installed in ZABs to serve as the air electrodes. Among them, metal organic framework (MOFs) have drawn significant interest owing to their fascinating architecture and unique electrochemical features, which are favourable for Zn-air batteries.

2.3 Metal Organic Frameworks (MOFs)

MOFs are emerging materials which have drawn tremendous interest in the last decade with various application potentials, such as gas sensing, gas adsorption, gas separation and energy conversion and storage. MOFs as a prominent division of porous crystalline materials, are constituted by the metal inorganic nodes, usually consisting of secondary building blocks, and organic ligands as struts through the coordination bonds, generating a distinct architecture subject to the synthesis conditions and the nature of the two major constituents (i.e. organic ligands and metal nodes).^[37] Therefore, the infinite number of unique MOFs materials can be assembled by varying the metal nodes and/or organic ligands and synthesis parameters. The first ever MOFs possessing porosity on permanent basis were disclosed by Yaghi and Li in 1995.^[38] To date, researchers have reported a range of MOFs structures as precursors to produce nano-porous carbon materials^[39], possessing large pore volume, large surface area, and high electrical conductivity.^[12] MOFs stand out among conventional porous materials, for instance, zeolites and carbon-based materials, owing to their unique features, such as high surface area, high porosity and low density.^[11b,40] Although, several MOF-derived carbons/metal composites have been served to enhance electrocatalytic activity, however, demonstrate inadequate electrocatalytic performance.^[41] Notably, ZIFs are prioritized among MOFs because of their versatile topologies, customizable functionalities and milder synthesis conditions. Thereafter, the fine-tuning of constituents and synthesis conditions of ZIFs leading to match the desired functionalities in the end-product.^[42] These characteristics of MOFs validate them for electrochemical applications, in particular, for air batteries. ZIFs consisting of organic ligand based on N-containing heterocyclic compounds, comprising abundant uncoordinated N atoms in the network may be a promising material as an air electrode. In contrast to other MOFs, a unique feature of ZIFs is their capability to provide a number of N atoms for the formation of C-N and M-N bonds, which are favourable for ORR activity.^[43] Consequently, zeolitic imidazolate frameworks (ZIFs) may be regarded as an affluent platform to provide nitrogen-rich porous carbon framework.

2.4 Zeolitic Imidazolate Frameworks

2.4.1 General properties

Recently, zeolitic imidazolate frameworks (ZIFs), recognized as a subclass of MOFs, have garnered tremendous attention owing to their unique architecture and fascinating electrochemical features. The framework of ZIFs is generally constructed by the reaction of tetrahedrally-coordinated, divalent transition metal ions (M^{2+} ions: Zn^{2+} , Co^{2+} , ...) as metal nodes, connected by imidazolate anions (Im^-) rings as organic ligand/linker (where N atoms in imidazolate linkers at the 1,3 - positions release proton and coordinate with metal nodes) in the presence of particular solvent (reaction medium), generating an extended 3D network with a periodic arrangement in the form of M-Im-M polyhedral crystal structure.^[44]

Among various MOFs, ZIFs have been regarded as researchers' first choice because of their low cost, structural flexibility, ultra-high surface area, abundant pores, excellent crystallinity, versatile surface geometry and N-rich carbonaceous network. ZIFs display multiple catalytic active sites, which may be associated with the unsaturated sites of coordinated metal ions as well as functional groups of organic moiety (imidazolate ligand).^[45] Concisely, the performance of the ZIF - derived materials is a joint venture of several factors like N-doped porous carbon with large surface area, abundant pores and availability of active sites developing highways for the efficient charge and mass transport. Interestingly, ZIFs are also prioritized over other MOFs by virtue of their tailorable structure, facile synthesis at room temperature and ease of control on fabrication parameters. Unlike other MOFs, ZIFs also exhibit unusual chemical and thermal stability.^[46] For instance, ZIF-8 can be boiled in aqueous and alkaline solution without sacrificing the porosity and crystallinity.^[47] The outstanding stability of ZIFs may be attributed to the strong M-N bonds, which imparts ultrahigh resistance against organic and aqueous alkaline solution.^[48] Besides, the solvent molecules which are capable of potentially attacking the M-N entity, tend to be repelled by the surface structures. Consequently, the structure evolved from the strong connections show excellent thermal stability and their morphology remain intact at a temperature as high as 500°C.^[49] Due to the adjustable physical and chemical properties, ZIFs have been emerged as a new generation of materials with relatively greater prospects of improvement and their utilization in multiple applications.^[50] Thus, the high chemical and thermal stability of ZIFs in relation with other MOFs make them an attractive candidate for their application on industrial scale.

The rich N heteroatoms doped in carbon lattice of ZIFs bring about three kinds of contributions: pyrrolic N, quaternary/graphitic N and pyridinic N contents. Of three types of N, quaternary N/graphitic and pyridinic N species in the carbon lattice promote the π -bonding, which is likely to accelerate the electron transport and the stability of carbon atoms.^[51] Pyridinic N moieties are considered as capable of withdrawing electrons and could be employed as active sites for OER. On the other hand, graphitic N, are known to have the capacity to deliver electrons, which in turn make them the ORR active sites.^[52] The pyridinic N is also beneficial to promote the onset potential^[53] and surface wettability^[54] whereas graphitic N enhances the diffusion - limited properties.^[46b, 54-55] Moreover, the species of graphitic and pyridinic N have also been recognized as active sites for ORR. It has also been demonstrated that ORR mechanism in the presence of pyridinic N proceeds through approximately $4e^-$ pathway.^[31] While, graphitic and pyridinic N species have also been revealed to be active sites towards both OER as well ORR.^[46b, 56] Besides, pyridinic-N develops a strong coupling effect with Co species and may enhance the highest occupied molecular orbital (HOMO) energy, which in turn promotes the ORR activity.^[46b] However, pyridinic-N is likely thermally unstable and transforms into pyrrolic-N and graphitic-N at elevated temperatures because graphitic-N starts to generate at high temperature.^[56c, 57]

This article is protected by copyright. All rights reserved.

The major limitations associated with ZIF derived materials is the loss of control over the morphology, porosity and N content as an outcome of pyrolysis at high temperature ($> 500^{\circ}\text{C}$). As it is inevitable to carbonize the ZIFs to achieve the graphitic carbon (highly electronic conductive), otherwise amorphous porous carbonaceous network. However, the pyrolysis of Co based ZIFs, for instance, ZIF-67 at high temperature leading to the higher degree of graphitization at the expense of N content, porosity and surface area, which would inhibit the mass transport and eventually the electrocatalytic activity.^[46b, 58] On the other hand, the formation of amorphous carbon is resulted after the pyrolysis of ZIF-8. Furthermore, the oxidation state of Co species cannot be controlled during pyrolysis, which would eventually reduce to Co in elemental form. In response, Co metallic species would catalyze the degree of graphitization of carbon and drop in N content and degree of porosity in ZIF-67 derived material.^[59] Thus, we have to make a trade-off between the N-content, degree of graphitization and degree of porosity to reach a balance of lucrative features. Interestingly, it is feasible to integrate the merits of graphitization, surface area and abundant N-content in the final product by developing core-shell structure of ZIFs (ZIF-8@ZIF-67).^[59] Eventually, the hierarchical micro/mesoporous architecture with high surface area ($1276\text{ m}^2\cdot\text{g}^{-1}$) and graphitic carbon could be attained without sacrificing the N content (upto 10.6 wt %).

Specifically, the morphology of ZIFs is isomorphic to classical inorganic zeolites because tetrahedrally-coordinated metal centres subtends at an angle of 145° with bridging imidazole organic ligand in M-Im-M network, which is similar to angle at Si(Al)-O-Si(Al) centres between SiO_2 tetrahedra and oxygen.^[60] The metal centres mimic the role of Si, while imidazolate adopts the role of oxygen and forming the bridge. The longer bond length of M-Im-M in contrast to the Si(Al)-O-Si(Al) leads to a larger pore diameter.^[61] Therefore, ZIFs share many traits of zeolites (mechanical, chemical and thermal stability), which stand them out among other MOFs.^[60d] These virtues in ZIFs are endowed by the metal-nitrogen (M-N) bonds as well as N - doped carbon (provided by the Im group).^[62] In contrast to the classical zeolites, a salient feature of ZIFs is their generous flexibility in designing a variety of architectures simply by developing a robust coordination between metal nodes and organic linker (imidazoles) or their mixture (mixed imidazole) under certain conditions.^[63] Thus, ZIFs are versatile materials, so various ZIFs architecture may be constructed by metal ions with organic imidazole ligand. A great number of ZIFs have been synthesized which exhibit the different topologies of ZIFs such as sodalite (SOD), gmelinite (GME), merlinoite (MER), analcime (ANA), gismondite (GIS), Faujasite (FAU), Chabasite (CHA), Linde Type A (LTA), β - quartz (QTZ) and rhodsite (RHO) to name a few (**Fig.6**). Besides, various ZIFs structures may be synthesized by the mixing of linkers. Notably, 15 structures out of them, for instance, ZIF-60-62, ZIF-68-70, ZIF-73-76 and ZIF 78-82 produce single-phase materials.^[64] There exists several types of ZIFs, possessing versatile characteristics, depending on the multiple metal centres (such as Co, Zn, etc.), synthesis

methods and post synthesis modifications.^[49a, 49b] By now, over 150 ZIFs structures have been reported.^[65]

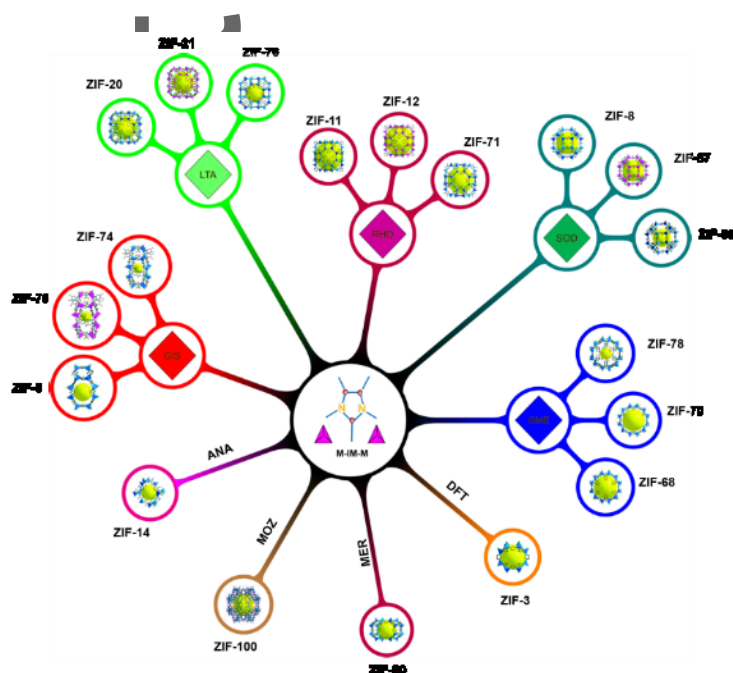


Fig. 6 Crystal structures of ZIFs based on their topology (three-letter symbol). Adapted with permission ^[60d], Copyright 2010, American Chemical Society.

2.4.2 Application of ZIFs in ZABs

The direct employment of ZIFs in electrochemical applications is inadequate because of their poor electronic conductivity. Alternatively, upon the pyrolysis of ZIFs in inert atmosphere, organic moiety is transformed into N-doped porous conductive carbon network, while exposing more facets of metallic species. Following the pyrolysis, a sufficient amount of nitrogen is preserved into the carbon structure.^[66] The presence of N has significant electrochemical relevance because it possesses high electronegativity, oxidation stability and its atomic size resembles with that of carbon. As a result, N atoms, on the one hand, induce charge delocalization on the carbon lattice because of electronegativity difference, and on the other hand, it develops a strong covalent bond with carbon atoms owing to the lowest lattice mismatch. Thus, N heteroatoms withdraw electrons from adjacent C atoms, thereby breaking the electro-neutrality of carbon atoms located in the vicinity, generating positively charged sites by modulating the electronic distribution.^[67] Eventually, positive sites promote the oxygen adsorption and lead to the ORR activity.^[68] Thus, N-doping in carbon is beneficial to significantly promote the electronic transport, mechanical strength and their interaction with reacting species and electrolyte ions.^[69] Besides, the coupling of the metallic species with the ZIF derived carbon also upgrades the rate of charge transfer.^[70] Consequently, ZIF-derived materials have attained the onset potential and half-wave potential ($E_{1/2}$) comparable to that of state-of-the art Pt/C catalyst

and categorized among the top rated one among the noble-metal-free electrocatalysts.^[71] Moreover, ORR mechanism on ZIF-derived materials is a four-electron pathway and is pursued in a multi-step process^[72] as illustrated in **Fig. 7**. Based on these properties, ZIFs have arisen as a research hotspot in the domain of energy conversion and energy storage, in particularly, for ZABs. On account of ease of functionalization, ZIFs can be further tuned to incorporate functional chemical groups with an intention of achieving the novel architecture with intended outcomes.^[73]

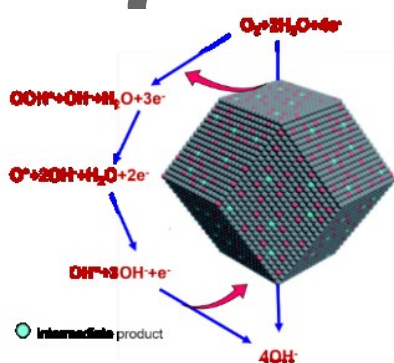


Fig. 7 ORR mechanism on ZIFs. Adapted with permission^[71]. Copyright 2020, The Royal Society of Chemistry

Interestingly, the open framework type architecture of ZIFs also provides a great opportunity to further attune and upgrade the parameters of electrocatalyst related to the electrocatalytic reaction, leading to the enhanced and optimal electrocatalytic performance.^[74] The large pore volume of ZIFs facilitate the swift diffusion of reactants as well as products through their channels. Thus, the porous architecture accompanied by high surface area efficiently enables the transport of electrolyte ions and withstands the volume transformations during charging/discharging.^[75] Intermolecular doping into porous network of carbon and nitrogen can significant influence on the physical and chemical properties and ended up into the active and robust electrocatalyst catalyst.^[76] Based on the aforementioned characteristics, ZIFs are preferred over other MOFs to facilely achieve N-doped porous carbon networks with regular pore structure and high surface area.^[77]

2.4.3 Commonly used ZIFs in Zn-air batteries

A variety of ZIFs-based materials consisting of different functionalities and morphologies have been fabricated by fine-tuning the ZIFs precursors or by manipulating the synthesis strategy. For instance, ZIF-67 and ZIF-8 with a sodalite topology, have been fabricated by employing the same organic ligand (2-methylimidazole) and by varying the coordinated metal nodes because former has Co nodes and latter has a Zn nodes. Both ZIF - 67 and ZIF - 8 have been frequently employed as an air electrodes in ZABs and demonstrated the promising electrocatalytic activities. Although, ZIF-67 and

ZIF-8 were found to have congruent geometrical architecture, however, differ in electrochemical properties (Fig. 8). Briefly, ZIF-67 was formed by the co-ordination between 2-methylimidazole organic linkers and Co^{2+} ion clusters with cubic crystal symmetry ($a = b = c = 16.9589 \text{ \AA}$).^[78] Upon the pyrolysis, ZIF-67 crystals possessing highly graphitic nanoporous carbon, were obtained at the expense of N content and surface area. In contrast to the ZIF-8, the graphitic carbon in ZIF-67 derived carbon was imparted by the catalytic graphitization effect of the uniformly dispersed Co nanoparticles^[59]. On the other hand, ZIF-8 crystal is formed by the co-ordination between 2-methylimidazole as organic linkers and Zn^{2+} ions. Following the annealing of ZIF - 8 at elevated temperature in inert atmosphere, Zn will undergo evaporation, leading to the hydrophilic N - doped microporous carbon together with high surface area, leading to the large mass transport.^[19] However, the carbon derived from ZIF-8 is in amorphous state, leading to the relatively low electronic conductivity and stability.^[79] Actually, the Zn evaporation at high temperature in the ZIF-8 framework would provide more porous sites and free N sites.^[80] Therefore, ZIF-8 derived crystals possess rather large N content (16 wt %) and high surface area ($1499 \text{ m}^2 \text{ g}^{-1}$). Eventually, ZIF - 8 is deemed as the ideal candidate among ZIF family to synthesize metal - free nitrogen - doped porous carbon. On account of tailorable physical and chemical properties, ease of functionalization, permanent porosity, high crystallinity, adjustable composition and structural diversity, ZIFs can be tuned to incorporate functional chemical groups with an intention of achieving the novel architecture with intended outcomes.^[73]

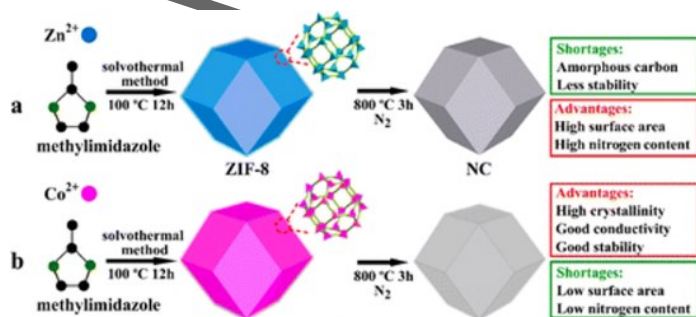
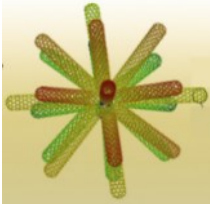
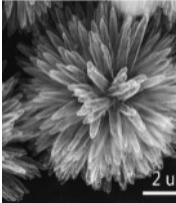
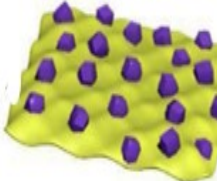
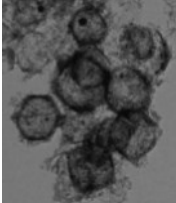


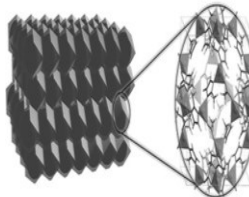
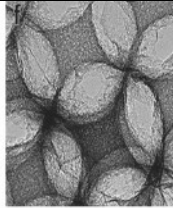
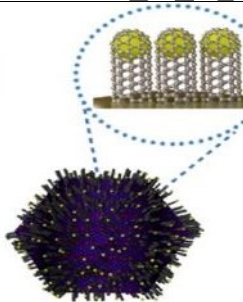
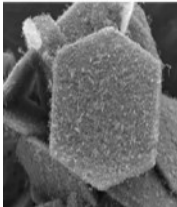
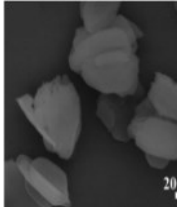
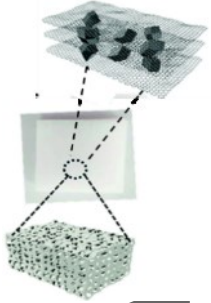
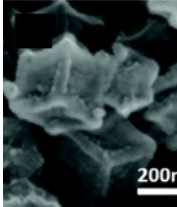
Fig. 8 Schematic of the synthesis scheme of (a) ZIF-8 polyhedrons and NC derivative; (b) ZIF-67 polyhedrons and graphitic carbon derivative. Adapted with permission.^[59] Copyright 2015, The American Chemical Society.

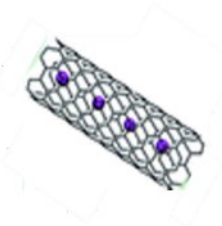
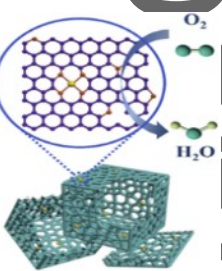
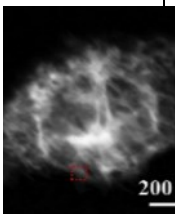
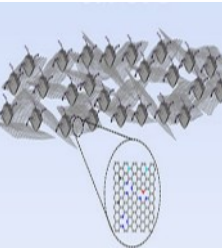
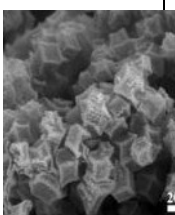
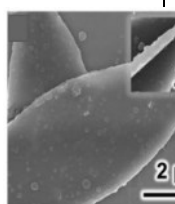
Table. 1 The physicochemical, electrochemical and morphological features of ZIF-derived materials followed by the different treatments

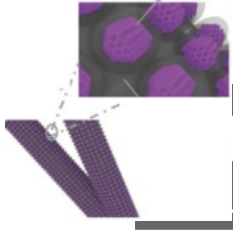
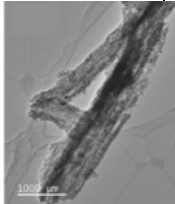
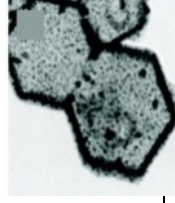
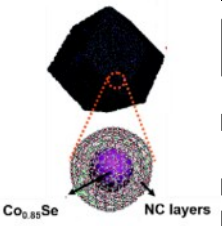
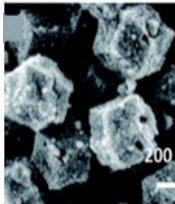
Air electrode	ZIFs Precursor	S.A (m ² g ⁻¹)	Pyrolysis Temp (°C)	Tafel slope		OE R (E _{j=10})	OR R (E _{1/2})	ΔE = E _{j=10} - E _{1/2} (V)	Morphology of ZIF-derived material	Ref.
				OR R	OE R					
Metal free carbon										
 NPCTC-850	ZIF-8	912	850°C (N ₂)	58	115	1.70	0.8	0.90	 [57b]	
 Co@NHCC-800	ZIF-67	911	800 °C (Ar)	-	84.2	1.52	0.79	0.73	 [81]	
	ZIF-8	2546	950 °C (N ₂)	74	-	-	0.8	-		[82]

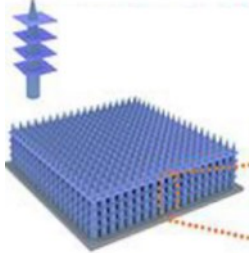
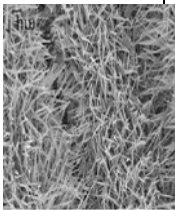
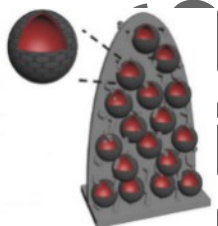
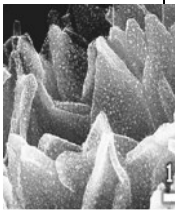
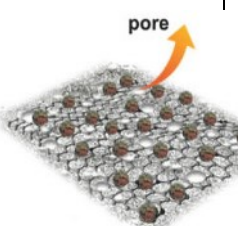
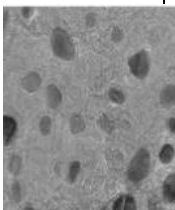
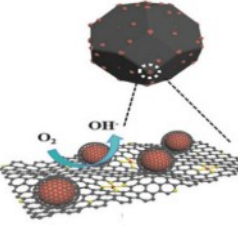
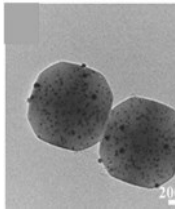
This is the author manuscript accepted for publication and has undergone full peer review but has not been through the copyediting, typesetting, pagination and proofreading process, which may lead to differences between this version and the [Version of Record](#). Please cite this article as [doi: 10.1002/aenm.202100514](https://doi.org/10.1002/aenm.202100514).

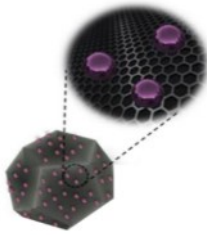
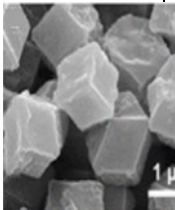
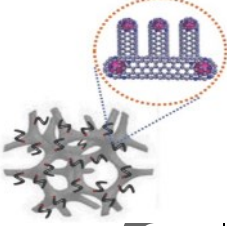
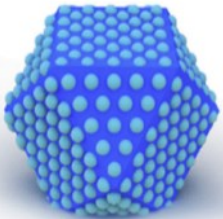
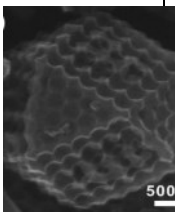
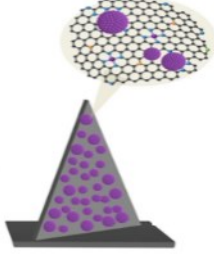
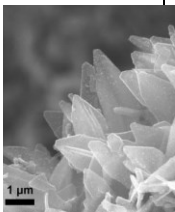
This article is protected by copyright. All rights reserved.

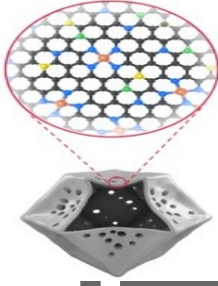
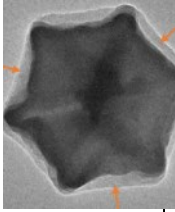
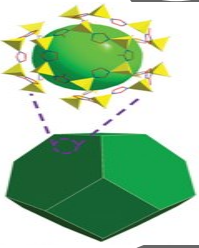
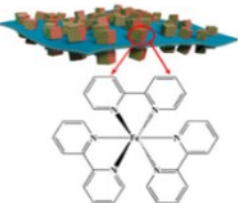
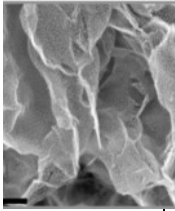
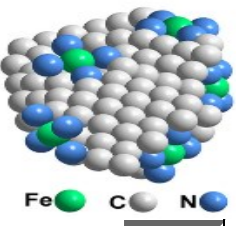
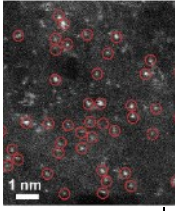
 <p>N-rich C crystals</p>											
Transition metal-doped carbons											
Single TM-doped carbons											
 <p>Co/Zn ZIF-L</p> <p>Co-N-PHCNTs</p>	411	900°C (N ₂)	50.9	63.8	1.62	0.89	0.73		[83]		
 <p>Co-NCS@CNT</p>	396	700 °C (Ar)	79.3	92.9	1.6	0.86	0.74		[84]		
 <p>s-Co@NCP/rGO-800</p>	229	800°C	-	-	-	0.85	-		[85]		

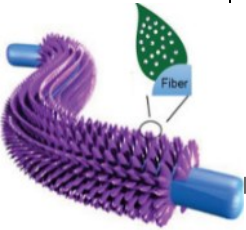
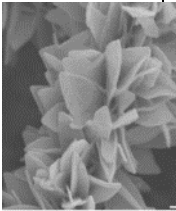
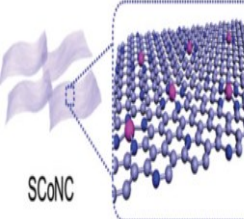
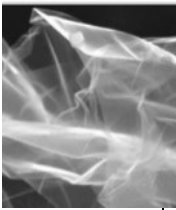
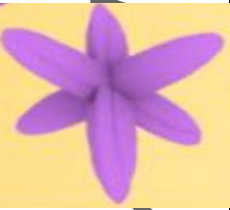
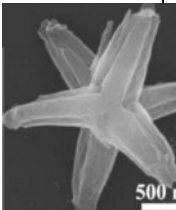
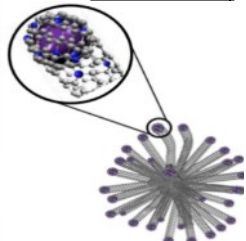
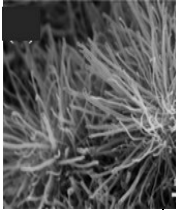
 Co@NCNT	ZIF-67	97	750 °C (inert)	94.8	11.6	1.64	0.828	0.81	 [76]
 Fe/N/C	ZIF-8	834	750 °C (N ₂)	-	-	-	0.89	-	 [86]
 Co/NGC-3	ZIF-67	328	700 °C (N ₂)	61	92	1.63	0.85	0.78	 [87]
 CuCo@NC	ZIF-67	326	900 °C (Ar)	63	95	-	0.866	-	 [88]

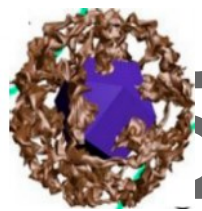
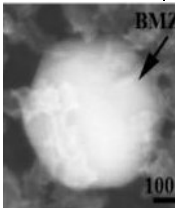
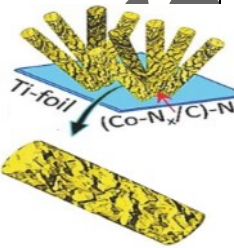
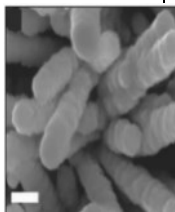
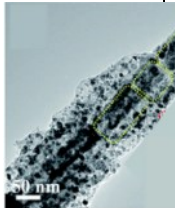
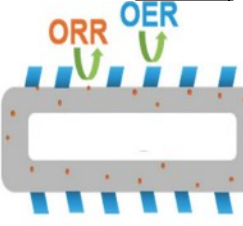
 CoP@mNSP - C	ZIF-67	203	1000 °C (Ar)	61	12 6	1.6 4	0.9 0	0.7 4	 [89]
 CoP/NC-800	ZIF-67	-	800 °C		62	1.5 2	0.7 8	0.7 4	 [90]
 CuCoP-NC-700	ZIF-67	232	700°C (N ₂)	67	62	1.5 7	0.8 72	0.6 98	 [91]
 Co _{0.85} Se@NC	ZIF-67	55	700°C (H ₂ /Ar)		75	1.5 5	0.7 9	0.7 6	 [92]
Transition Metal Oxides									

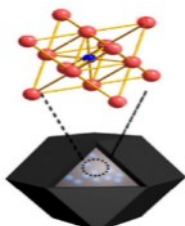
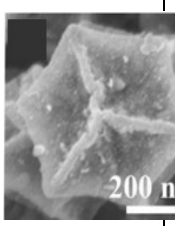
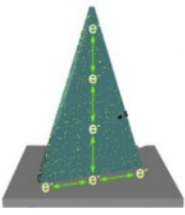
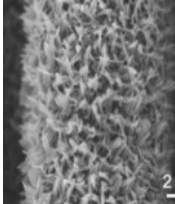
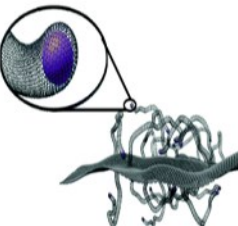
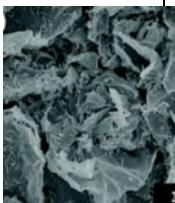
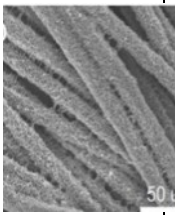
 <p>ZIF-67</p> <p>$\text{Co}_{0.68}\text{Fe}_{0.32}\text{O}@N$ C/CC</p>	-	450 °C (N ₂)	58.9	63.3	1.49	0.81	0.68	 <p>[93]</p>
 <p>ZIF-67</p> <p>NC - Co₃O₄ - 90</p>	12.8	700°C (H ₂ /Ar)	-	-	1.58	0.87	0.71	 <p>[94]</p>
 <p>ZIF-67</p> <p>Co/Co₃O₄@PGS</p>	385	920 °C (Ar)	52.6	76.1	1.58	0.89	0.69	 <p>[95]</p>
 <p>ZIF-8</p> <p>Cu@Fe-N-C</p>	726	900 °C (Ar)	78	-	-	0.892	-	 <p>[96]</p>
Bimetallic transition metals-doped carbons								

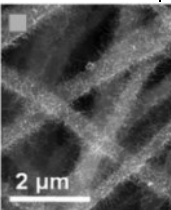
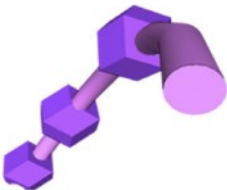
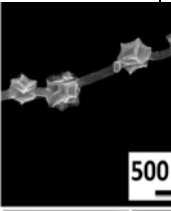
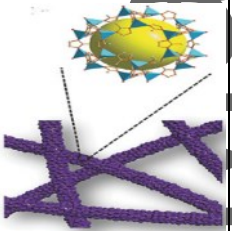
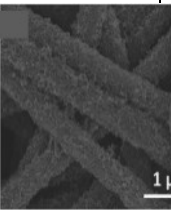
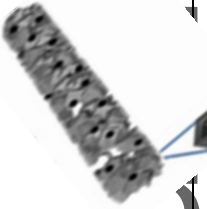
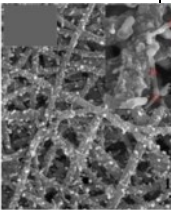
 <p>Mn_{0.9}Fe_{2.1}/CNC</p>	ZIF-8	410	900 °C (N ₂)	93. 3	-	1.6 2	0.7 8	0.8 4	 <p>[3]</p>
 <p>Co - N - CNTs</p>	ZIF - L	250	900 °C (Ar)	-	-	1.6 9	0.9 0	0.7 9	 <p>[97]</p>
Single metal atom modified carbons									
 <p>3DOM-Fe-N-C</p>	ZIF-8	876	900°C (5% H ₂ /95% Ar)	49	-	-	0.8 75	-	 <p>[98]</p>
 <p>NC-Co SA</p>	ZIF-67	319	-	-	-	1.5 8	0.8 6	0.7 2 V	 <p>[99]</p>

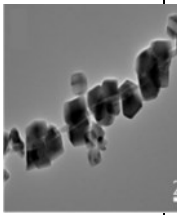
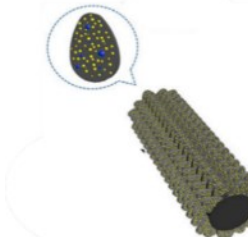
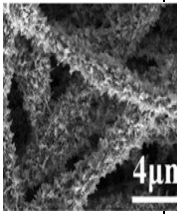
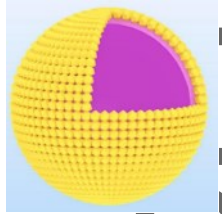
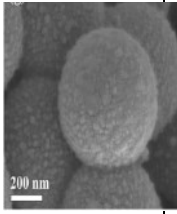
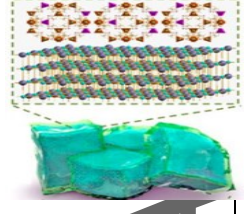
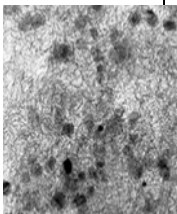
 <p>Fe-SAs/NPS-HC</p>	ZIF-8	-	900 °C (Ar)	36	-	-	0.9 12	-	 <p>[100]</p>
 <p>Fe - N_x - C</p>	ZIF-8	-	900 °C (Inert)	24 3	-	1.8 3	0.9 1	0.9 2	 <p>[101]</p>
 <p>FeN_x-embedded PNC</p>	ZIF-8	1162	-	-	80	1.6 35	0.8 6	0.7 75	 <p>[43c]</p>
 <p>Fe-N-C</p>	ZIF-8	1009	950°C (N ₂)	-	-	1.8 1	0.8 95	0.9 15	 <p>[102]</p>

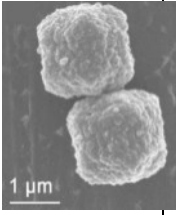
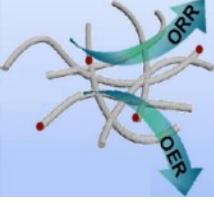
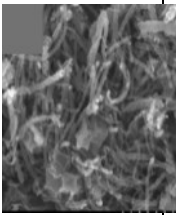
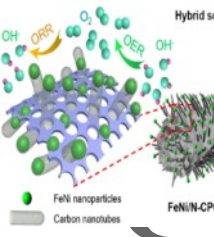
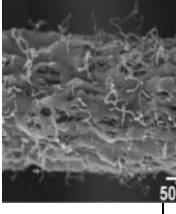
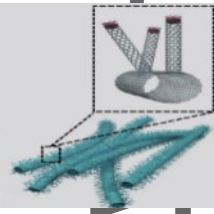
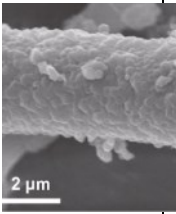
 Co SA@NCF/CNF	ZIF-67	696	850 °C	-	56	1.6 3	0.8 8 V	0.7 5		[103]
 SCoNC SCoNC nanosheets	ZIF-67		750°C (Ar)	70	74	1.5 4	0.9 1	0.6 3		[104]
 Co _{SA} -N-C	ZIF-8 and ZIF-L	570	910°C (N ₂)	-	-	-	0.8 9	-		[105]
Core/Shell										
 3D-CNTA	ZIF-67	108	650°C (N ₂)	-	89	1.5 9	0.7 8	0.8 1		[106]

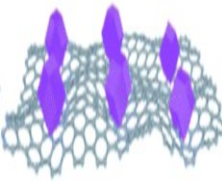
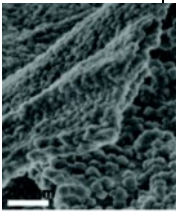
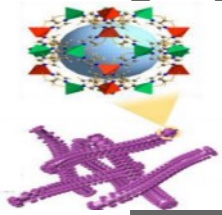
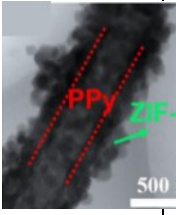
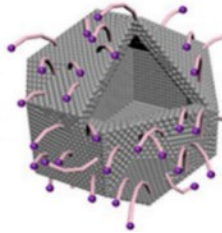
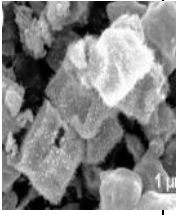
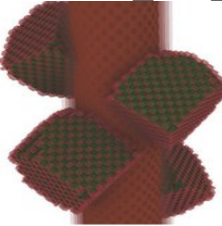
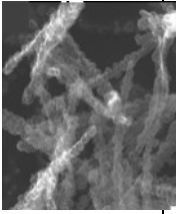
 Fe/N/C@BMZIF	Zn/Co-2MIM(BM ZIFs)	560	900°C (Ar)	59.4	-	1.64	0.85	0.79		[107]
 Co-N _x /C NRA	ZIF-8	-	900°C (N ₂)	66	62.3	1.53	0.877	0.65		[46b]
 MnO@Co-N/C	ZIF-67	125	900°C (Ar)	78	-	1.76	0.83	0.93		[108]
 NiFe-LDH@Fe/CNP	ZIF-8	440	900°C (N ₂)	-	-	1.594	0.867	0.727		[109]
CoN₄/Carbon composite										

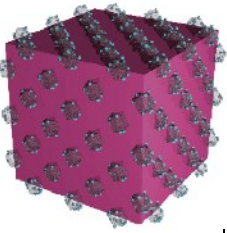
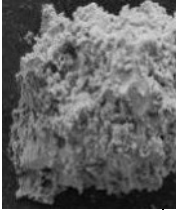
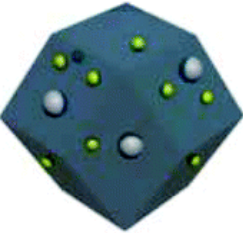
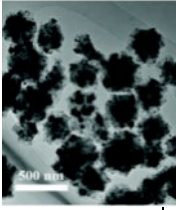
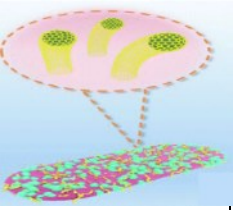
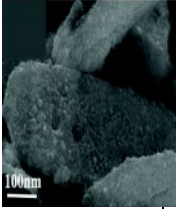
 Co ₄ N@NC-2	ZIF-67	282	900°C (N ₂)	65	68	1.5 19	0.8 4	0.6 79		[110]
 Fe-Co ₄ N@N-C	ZIF-67	-	700°C (H ₂ /Ar)	58	62	-	0.8 3	-		[111]
 Co/Co ₄ N@N-CNTs/rGO	ZIF-8@ZIF-67	-	900°C (Ar)	-	10 3	1.6 1	0.6 8	0.9 3		[112]
 Co ₄ N/CNW/CC	ZIF-67	226	700°C	-	81	1.5 4	0.8 0 V	0.7 4		[113]
Nanofibers from electrospinning										

 CoNC/NCNTs@ CNF	ZIF-8/ZIF-67	261	900°C (N ₂)	92	82	1.6 2	0.7 8	0.8 4	 [114]
 C-PAN@ZIF-67	ZIF-67	292	850°C (Ar)	-	-	-	-	197 mV	 [115]
 CNF@Zn/CoNC	ZIF-67	490	800°C (N ₂)	43. 3	12 4	1.7 0	0.8 2	0.8 8	 [116]
 Fe/N-HCNFs	ZIF-8	279	900 °C (N ₂)	90	11 6	1.6 7	0.8 3	0.8 4	 [117]

 Fe/Co-N/P-9	ZIF-67	137	900 °C	70.6	-	1.66	0.85	0.81	 [118]
 Co ₉ S ₈ -MoS ₂ /N-CNAs@CNFs	ZIF8/ZIF-67	178	800 °C (Ar/H ₂)	84	140	1.57	0.82	0.75	 [119]
Alloys/Carbon composites									
 CoFe/N-HCSs	ZIF-67	200	700 °C (10% H ₂ -90% Ar)	59	58	1.50	0.791	0.71	 [120]
 Fe-ZIF-67@NaCl	ZIF-67	-	750 °C (N ₂)	-	-	1.62	0.98	0.64	 [46a]

 <p>Fe_{0.3}Co_{0.7}/NC cage</p>	ZIF-8	52	800 °C (N ₂)	79	-	-	0.8 8		 <p>1 μm</p>	[121]
 <p>1.5FeNi@NCNT</p>	ZIF-8	490	900 °C (inert)	77	55	1.4 7	0.8 6	0.6 1		[122]
 <p>FeNi/N-CPCF-950</p>	ZIF-8	21	950 °C (Ar)	66	67	1.5 85	0.8 67	0.7 18	 <p>50</p>	[123]
ZIFs-based hybrids										
 <p>CMT@CNT</p>	ZIF-67	354	800 °C (N ₂ /H ₂ , 9/1)	61. 2	43. 3	1.5 58	0.8 8	0.6 78	 <p>2 μm</p>	[124]

 <p>ZnCo-ZIF@GO</p>	ZIF-67	-	-	-	83	1.66	0.76 V	0.90	 <p>[125]</p>
 <p>Co@hNCTs-800</p>	ZIF-67	307	800°C (Ar)	-	-	1.63	0.87	0.76	 <p>[126]</p>
 <p>NiCo₂O₄/Co,N-CNTs NCs</p>	ZIF-67	251	600°C (Ar)	60	61	1.57	0.862	0.707	 <p>[127]</p>
 <p>pCNT@Fe_{1.5}@G/L/CNF + NiFe LDH/NiF</p>	ZIF-8	1220	950°C (Ar)	61.9 ± 3	-	-	0.87	-	 <p>[128]</p>

 <p>BSCF@Co-N-C</p>	ZIF-67	128	750°C (N ₂)	-	99	1.6 3	0.8 0	0.8 3	 <p>[67b]</p>
 <p>CeO₂/Co@N-doped C</p>	ZIF-67	-	-	-	-	1.7 0	0.9 33	0.8 92	 <p>[129]</p>
 <p>Co₉S₈/CeO₂/Co-NC</p>	ZIF-67	122	600°C (N ₂)	56	52	1.6 0	0.8 75	0.7 25	 <p>[130]</p>

3. Recent advances of ZIFs-derived electrocatalysts as air electrodes for ZABs

The catalytic activity of ZIF-derived air electrodes for ZABs may be enhanced by developing some special structures through the materials tuning, morphology control and by the hybridization. A comprehensive summary of physicochemical, electrochemical and morphological features of ZIF-derived materials followed by the various treatments are tabulated in **Table. 1**. Moreover, the performance indicators of ZAB acquired after integrating the different ZIFs derived materials as air electrode into ZABs are presented in **Table. 2**.

3.1 materials tuning

3.1.1 Metal-free carbons

Carbon-based materials featuring flexible physicochemical and structural properties, high conductivity, low cost and abundance are considered among the front-runners to substitute the noble metals as reversible oxygen electrocatalysts.^[131] In contrast to metal loaded catalysts, metal-free carbon catalysts help to avoid the issues of leaching and particle agglomeration, thereby exhibit better long term stability. For the development of carbon-based materials, numerous factors such as effective reactants (OH^- and O_2) transport to active sites and optimum amount of adsorption energy between reaction intermediates and reactants should be taken into account.^[51, 132] Thus, the interconnected hierarchical porous network may lead to the accessible electroactive surface area and plentiful active sites to expedite the mass transport.^[133] In particular, N-doped porous carbons have been recognized as an efficient ORR electrocatalyst because the higher electronegativity of N (3.0) modulate the charge distribution of C (2.5) by withdrawing electron from carbon atoms. In view of above discussion, ZIF-8 may be opted as an ideal precursor to obtain N-doped metal free carbon materials possessing large surface area and highly ordered porous architecture. As ZIF-8 consists of Zn metal and N-containing ligand, which upon carbonization at high temperature ($>908\text{ }^\circ\text{C}$) leads to the metal free N-doped carbon because Zn was carbothermally reduced and evaporated.^[134] Following the pyrolysis of ZIF-8, N-doped and interconnected porous carbon network is attained, which is crucial for the rapid charge transport to ensure the high electrocatalytic performance. Therefore, N-rich carbon has arisen as a substitute to commercial Pt catalysts for accelerating ORR activity in ZABs.^[135]

Several studies have demonstrated that the insertion of another heteroatom like boron^[136], phosphorus^[137], sulphur^[138] and halogens^[139] along with N-doped porous carbon materials further

This is the author manuscript accepted for publication and has undergone full peer review but has not been through the copyediting, typesetting, pagination and proofreading process, which may lead to differences between this version and the [Version of Record](https://onlinelibrary.wiley.com/doi/10.1002/aenm.202100514). Please cite this article as [doi: 10.1002/aenm.202100514](https://onlinelibrary.wiley.com/doi/10.1002/aenm.202100514).

This article is protected by copyright. All rights reserved.

upgrade the electrocatalytic activity as an outcome of tuning of electronic and surface properties [65, 140]. For instance, Li et al. developed metal free, multi branched P, N co-doped cluster of carbon nanotube consisting of well-connected hollow framework via the treatment of ZIF-8 with butyl methylphosphinate, subsequent to two step pyrolysis.^[57b] The resultant cross-linking polymerization developed through the covalent bonds (P–O–P and C–O–P) between monomers and ZIF-8, endowed the electrocatalysts with enhanced mechanical properties. N, P co-doped inherited the morphology of the highly branched CNTs cluster (**Fig. 9 d**). In spite of ultrathin thickness of wall, no prominent collapse and shrinkage visualized after the graphitization, thus the ultrathin structure contributed to the swift electron and mass transport. Nanotube cluster exhibited excellent OER and ORR in ZABs and a stable electrocatalytic performance over 180 cycles at a current density of 5 mA cm⁻² with a 0.15 V rise in overpotential. The enhanced electrochemical performance may be credited to the 3D interconnected hollow geometry and synergistic effect of P, N co-doping.

It may be inferred that P, N co-doped NPCTC-850 catalyst display phenomenal bi-functional activity thus far, among the heteroatom doped metal-free carbon based air electrodes derived from ZIFs for ZABs. Actually, heteroatom doping to ZIF-derived porous carbon matrix induce asymmetrical charge distribution as an outcome of high electron spin density (S) or electronegativity (B, P, N, F, etc.) difference between heteroatoms and carbon. Thus, heteroatom-doping to carbon lattice imbue non-electro-neutral mode by breaking their electro-neutrality of carbon. In the similar fashion, N, P co-doping could induce charge redistribution and generate positive charged sites (C⁺, P⁺). These sites are conducive for the chemisorption of oxygen and intermediates, promoting the ORR activity.^[141] The superiority of N, P co-doping is also confirmed by the theoretical computations because the activation energy (rate limiting step) required for the Langmuir-Hinshelwood mechanism in case of N, P co-doped carbon was the lowest i.e. ~0.5 eV, in contrast to the Pt (0.55 eV) and N doped carbons (0.56–0.62 eV).^[142] As a result, the optimal catalyst NPCTC-850 demonstrated the outstanding ORR performance and outperformed the benchmark Pt/C catalyst in terms of limiting current density and half-wave potential and less onset potential for oxygen evolution reaction (OER) in comparison with IrO₂. The detailed discussion on the heteroatom doping to metal free carbon and their influence on ZABs performance may be referred to our recent review article regarding the metal-free carbon based air electrodes for ZABs.^[31]

Similarly, Qian et al. fabricated metal-free, B-N co-doped highly porous carbon materials using different Zn-based MOFs, including ZIF-8 as the precursors.^[143] Upon the pyrolysis of Zn-based MOFs in the H₂/Ar mixture atmosphere, Zn evaporated and yielding metal-free carbon materials. The surface area of carbon material had significantly improved after Zn evaporation and B and N uniformly distributed within the framework of carbon material because of crystalline structure of MOFs. By virtue of its large surface area and evenly dispersed active sites, ZIF-8 derived carbon

exhibited prominently high onset potentials. However, B-N co-doped ZIF-8 derived carbon was not able to achieve high activity, presented low current densities and eventually, led to the inferior overall ORR catalytic performance in contrast to the rest of derived carbon materials. Furthermore, when the resultant catalyst employed for ZAB, it sustained only for 100 h with a larger potential gap of 1.02 V.

Despite the benefits, when ZIF-8 undergoes high - temperature pyrolysis (>908 °C) for the evaporation of Zn to render metal-free carbon, meanwhile, ZIF loses the carbon species and typical polyhedron morphology as a result of direct pyrolysis. Moreover, majority of N in ZIF ligand was evaporated before incorporating into the graphitic carbon framework, leading to the poor utilization and accessibility of active nitrogen dopants.^[144] consequently, it exhibits the poor electronic conductivity and inferior electrochemical performance.^[79b, 145]

Recently, metal free molten salt - assisted calcination of ZIF-8 emerged as a promising strategy to promote the graphitization degree and uphold the morphology and nitrogen content.^[146] In addition to the multi-functionality, NaCl confining template is preferred because it serves as an intercalating agent for the formation of mesoporous material and it is inexpensiveness, non-toxic and easily removable.^[147] Wang et al. prepared a 3D carbon electrocatalyst in a NaCl - sealed reactor, ZIF - 8@NaCl by in - situ networking of C polyhedrons with nanosheets via high - temperature pyrolysis of ZIF-8 at 900 ° C (**Fig. 9 f**)^[146b]. Confinement of ZIF-derived carbon in the salt reactor imparts a high yield with no considerable loss of active carbon species, which eventually contribute to quick electron and mass transport. Consequently, ZABs employing ZIF - 8@NaCl as the cathode also demonstrated outstanding performance. Similarly, Yan et al. also managed to prepare N-doped, metal-free porous carbon network through the pyrolysis of ZIF-8, templated by NaCl (**Fig. 9 a**)^[148]. Morphology analysis reveals a rhombic dodecahedral shape; a hollow structures surrounded by a thin layers of carbon layer followed by the washing of NaCl template, graphitic walls (SAED images) and uniform distribution of C, N and O (**Fig. 9 b**). As a result, such electrocatalyst enabled the reduction of O₂ (**Fig. 9 c**) with high ORR activity and selectivity possessing a E_{1/2}: 0.86 V and ZAB harvested a large peak power density (272 mW cm⁻²) and long cyclic stability (160 h).

Several researchers have reported that high N content together with richer porous design and higher surface area may further improve the ORR activity because the direct pyrolysis of ZIF-8 yields micropore-dominant architecture, leading to limited mass transfer due to poor exposure of active sites.^[149] Consequently, 3D pore structure and the involvement of hierarchical porous structure like macro, meso- and micro-pores would offer upgraded catalytic performance.^[150] Consequently, Xuan et al. proposed NaCl-assisted exfoliation strategy to prepare three-dimensional, N- doped porous carbons (NHPCs) by the carbonization of ZIF-8.^[151] At an elevated temperature, sodium chloride crystals transformed into a molten state. It functioned as a template and intercalating agent ^[152], infiltrating

through the ZIF-8 derived carbon *via* capillary action to allow the evolution of morphology to interconnected networks of 3D nanosheets from ZIF polyhedrons. The optimum graphitization degree, morphology and type of nitrogen in the derived carbons achieved by fine-tuning the weight ratio of ZIF-8 and sodium chloride as well as the pyrolysis temperatures. The surface studies of chemical states of N atoms conducted using XPS, implied that the molten NaCl salt demonstrated an important role in modulating the coordination of N with C (**Fig. 9 e**). It is worth mention that significant proportions of graphitic - N and pyridinic - N were protected through NaCl - assisted calcination. Graphitic carbon doped with pyridinic and graphitic N are recognized to have excellent OER and ORR electrocatalytic activities.^[56d, 56e, 153] In similar manner, Qian et al. designed an interconnected web - like carbon network followed by the carbonization of NaCl/ZIF - 8 composites.^[146a] Upon carbonization, the molten sodium chloride salt contributed to promote the graphitization of ZIF - 8 derived carbon and integrated them into interconnected carbon fibers enriched with ORR active sites. Subsequently, washing of obtained material led to the creation of macropores after NaCl removal, which served as channels for quick mass transfer, meanwhile Zn evaporation provided micropores.^[39a] It is worth mention that molten salt assisted pyrolysis had suppressed the pyridinic N content by 30% and augmented graphitic N species by 20%. Yang and co-researcher also conducted an effort to circumvent the challenge of inadequate exposure of N dopants using dual - templating strategy by integrating silica template.^[154] They obtained in situ ZIF-8 texturing supported on the silica photonic crystal hard template. Following the direct carbonization with no extra activation to obtain three-dimensional, N - rich carbon photonic crystal structure consisting of numerous tiny macroporous ordered framework. As a result, a permeable cathode with hierarchical macro - meso - microporosity, ultralarge surface area ($2546 \text{ m}^2 \text{ g}^{-1}$) and large total pore volume ($13.42 \text{ cm}^3 \text{ g}^{-1}$), allowing the enough accessibility and exposure of nitrogen dopants. When applied as a cathode material, prominent graphitic - N significantly contributed to promote the ORR activity of primary Zn-air batteries. Morphological studies unveil that subsequent to silica photonic crystal template removal, a replica hierarchical porous carbon framework with interconnected walls obtained (**Fig. 9 g**). It behaves similar to “photonic crystals” possessing distinct optical properties.

Another major concern associated with the pyrolysis of ZIFs is the collapse of porous framework and the fusion of active sites together, thereby causing the unsatisfactory catalytic activities. Consequently, these implications call for devising the strategy to protect the nanostructured polyhedral morphology of ZIF precursor while confining the N content following the pyrolysis. Therefore, Wu et al protected the ZIF polyhedron morphology and N content by confining the ZIF crystals into dense silica nanoparticles. It helped in securing sufficient N content with high surface area, exposing the ample active sites, leading to excellent OER/ORR bi-functional catalytic performance.^[81] Interestingly, after the leaching out of Co species by acid etching, they established

that metal free, ZIF-67 derived N doped carbon predominantly contribute to ORR, wherein the role of Co species was minimal. In case of OER, the role of Co species was trivial because OER activity of the resultant catalyst was comparable before and after acid leaching. Thus, ZIF-67 derived, metal free graphitic carbon self-doped with N (pyridinic N and graphitic N) contribute well to ORR. TEM morphology revealed that typical ZIF-67 polyhedron nanocrystals were greatly secured after pyrolysis under the protection of SiO₂. On the other hand, without SiO₂ encapsulation, large and non-uniform agglomerated particles were observed, which may be ascribed to the collapse and fusion of carbon framework. Nevertheless, N content had significantly reduced accompanied by the considerable rise in potential gap only after 12h of charging/discharging Zn-Air battery performance, even though the polyhedron morphology rather maintained even after the pyrolysis.

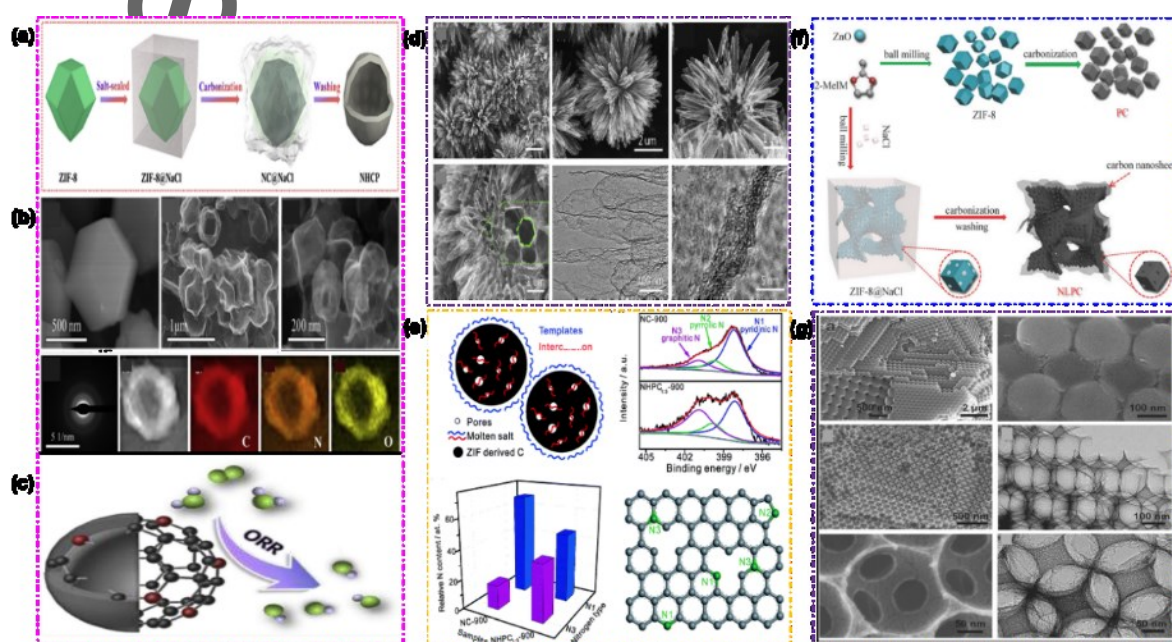


Fig. 9 (a) Schematic illustration of the formation of NHCP. (b) SEM images of ZIF-8-raw and NHCP-1000; SAED image of NHCP-1000; STEM images of NHCP-1000 and corresponding elemental mapping images (c) illustration of ORR activity over NHCP-1000. Reproduced with permission.^[148] Copyright 2020, Elsevier Ltd. (d) Typical SEM images of NPCTC-850. Reproduced with permission.^[57b] Copyright 2018, Elsevier Ltd. (e) Illustration of the NaCl role during the pyrolysis process; XPS analysis of N of NC-900 and NHPC_{1.3}-900; relative content of graphitic-N (N₃) and pyridinic-N (N₁) and Schematic diagram of the NHPC_{1.3}-900. Reproduced with permission.^[151] Copyright 2018, The Royal Society of Chemistry; (f) The preparation of PC and NLPC. Reproduced with permission.^[146b] Copyright 2018, WILEY - VCH; (g) SEM images of the SiO₂ template modified with ZIF - 8 crystal before and after carbonization at 950 °C for 5 h; SEM images with various magnification of BHPC - 950 after hydrofluoric acid (HF) etching and Typical TEM image of BHPC - 950. Reproduced with permission.^[154] Copyright 2017, WILEY - VCH.

3.1.2 Transition metal-doped carbons

3.1.2.1 Single TM-doped carbons

Transition metal (M) based M-N-C catalysts have emerged as a substitute to the precious metals catalysts for Zn-air batteries. It is recognized that the presence of transition metals with conductive type of carbon significantly lowers the oxygen adsorption free energy by promoting the transfer of electron from C to O₂, thus contribute to upgrade the ORR activity.^[155] Among transition metals, cobalt based Co-N-C catalysts have extensively been reported for their bi-functional activity for secondary ZIBs. ZIF-67

has been the most prominent precursor to achieve the Co-N-C catalysts.^[156] ZIF-67 derived Co-N-C catalysts are recognized for their excellent ORR performance.^[157] For instance, Li et al. designed Co/N-doped carbon derived from ZIF-67 by direct calcination at 800 °C under N₂ atmosphere^[158]. They also studied the electrochemical performance of series of Co/N-doped carbon by varying mass of cobalt nitrate hexahydrate/2-methylimidazole and figured out 0.675/5.5 as an optimal electrocatalyst in terms of electrochemical performance. The catalyst demonstrated superior bi-functional activity at current density of 20 mA cm⁻². However, the catalyst was no longer stable because the voltage gap started to rise only after 12h. Therefore, this electrocatalyst may be a promising one for the future research. Likewise, Xia et. al directly fabricated the hollow, Co particles embedded and N-doped carbon nanotube framework as a bifunctional catalyst for OER and ORR after the calcination of a single ZIF-67 precursor. The resultant electrocatalyst possessing robust structure, composition, N-doping and graphitic degree, outperformed the benchmark Pt/C electrocatalyst in terms of electrochemical performance and stability.^[159] For instance, they demonstrated superior half wave and onset potential to their nanocarbons counterparts. Actually, this work paved the way for the development of number of MOF-derived materials for the application in batteries.

Generally, ZIFs tend to collapse during pyrolysis, losing their typical structure and transform them into amorphous carbon^[95, 160], leading to the reduction in surface area and inadequate electronic conductivity.^[155b, 161] Therefore, it is highly desirable to synthesize ZIF derived material possessing high electrochemical active surface area to ensure the accessibility of reactants. Recently, Guan et al. developed Zn/Co (1:1) dual-metal ZIFs by surfactant-assisted method (**Fig. 10 a**), which upon carbonization rendered the embedded Co nanoparticles, N-doped positive-hexagon like carbon nanosheets (**Fig. 10 b-d**).^[83] Additionally, Co nanoparticles encapsulated carbon nanotubes (CNTs) were also grown on the carbon nanosheets (**Fig. 10 e-g**). It is worth mention that Co²⁺ and Zn²⁺ coordination effect and the hydrophilic groups of the surfactants could suppress the growth of ZIFs crystals and control the morphology and crystal size.^[162] Polyvinyl pyrrolidone, on the other hand, served as an encapsulating agent, prevented the vertical growth of ZIFs, led to the 2D hexagon sheets.^[163] This strategy helped to avoid to collapse of the two-dimensional structure. Moreover, the exclusively intertwined CNTs promoted the electrical conductivity, structural stability and exposed the Co active sites. The resultant electrocatalyst demonstrated admirable long-term stability over a period of more than 650h for 2000 charge/discharge cycles (**Fig. 10 i**) with no prominent decline in potential gap as compared to the state-of-the-art Pt/c-RuO₂ catalyst (**Fig. 10 h**). These interesting results with excellent OER as well ORR activity and remarkable stability is one of the finest records among ZIF-derived air cathodes for ZABs. In addition, this report provide new paradigm for the synthesis of 2D ZIF-derived materials for ZABs and other energy storage materials.

Likewise, Chen et al. also designed ZIF-derived one dimensional carbon nanotubes grafted onto the two dimensional carbon framework sheets, followed by the H₂-reductive carbonization by adopting a different strategy.^[84] In fact, they utilized water as a solvent during synthesis, instead of conventional methanol solvent to achieve a unique morphology. Two dimensional nanosheets provided the large surface area with Co nanoparticles were dispersed on the sheet, meanwhile Co nanoparticles were also anchored on the tip of one dimensional carbon nanotubes. Both of these features offered excellent electronic conductivity. From XPS analysis (**Fig. 10 l**), it is obvious that the content of graphitic N and Co-N_x active sites in Co-NCS@CNT were higher than the rest of the catalysts, which are reported to have vital role in upgrading the ORR activity.^[164] In spite of favorable mass transfer endowed by the 1D-on-2D hierarchical architecture of resultant catalyst, rechargeable Zn-air battery was not considerably durable over a longer period. Moreover, graphitic carbon in the ZIF-derived materials was also relatively lower than their counterparts.

In another attempt to escape the issues of breakdown and the aggregation of ZIFs nanocrystals, Jia-Jun Cai et al. fabricated Co encapsulated in N-doped sandwich-like carbon structure.^[85] They obtained the precursor by decorating the layers of graphene oxide and ZIF-67 on sponge template. Following the pyrolysis, the surface of smooth ZIF-67 polyhedron had transformed into rough morphology accompanied by the reduction in size (**Fig. 10 m and n**) and without losing the dodecahedron morphology. On the other hand, the morphology of carbonized ZIF-67 had been collapsed without incorporating sandwich-like structure (**Fig. 10 o**). As per HRTEM (**Fig. 10 p**), Co species were enclosed by amorphous and graphitic carbon. The later was induced by the graphitization effect of Co in the course of pyrolysis.^[165] The homo-dispersion of Co, N and C are illustrated by the mapping (**Fig. 10 q**) and sandwich structure is demonstrated by the schematic (**Fig. 10 r**). They succeeded to upgrade the ORR activity owing to higher accessible surface area and low diffusion resistance and this work provided guideline to configure sandwich-like architecture. However, the catalyst was stable only for 70h and still lacks in OER activity. Likewise, Zhang et al. fabricated Co species anchored in nitrogen-doped carbon nanotubes via carbonization of mixture of dicyandiamide and ZIF-67 at 750 °C.^[76] The catalyst exhibited a decent oxygen reduction reaction (ORR) performance in both alkaline and acidic media, as well as oxygen evolution reaction (OER) in alkaline medium. The bi-functional performance of electrocatalyst was attributed to synergistic effect of nitrogen dopant and Co nanoparticles in unique structure. The performance of resultant catalyst was not so encouraging in terms of recharge-ability and stability (18h).

Besides, the size of the catalyst on nanoscale is crucial to offer greater contact area between catalyst and electrolyte in comparison with their bulk counterparts. In this way, diffusion barrier would be reduced for electrolyte and the strength of active sites.^[166] Li et al. developed an electrocatalyst based on ultrafine Co nanoparticles supported by N doped graphitic carbon.^[87] It was obtained by a facile strategy of tuning ZIF-67 crystal size from 0.93 ± 0.2 to 0.31 ± 0.1 μm by the simultaneous induction

This article is protected by copyright. All rights reserved.

of glucose and graphitic carbon nitride without using any deprotonating agents. The resultant Co/NGC-3 catalyst demonstrated excellent OER performance with a smaller overpotential (396 mV) in attaining a 10 mA cm^{-2} of current density (**Fig. 10 s**), and possessing the lower Tafel slope than their counterparts (**Fig. 10 t**). Moreover, ΔE value of the Co/NGC-3 catalyst was around 0.78V, ratifying their potential as a bi-functional material. Consequently, when the optimal catalyst was employed for Zn-air battery, it exhibited excellent charging/discharging repeatability over a period of 120h with a rise in round-trip overpotential from 0.88 V to 0.91 V (5.7% drop in voltaic efficiency) (**Fig. 10 u**). Thus, it may be evaluated that this work will direct to facilely synthesizing ultrafine metal nanoparticles supported by N doped graphitic carbon provided by ZIF. $\text{Fe-N}_x/\text{C}$ catalysts are known to demonstrate the greatest application prospect for ORR activities.^[167] Unfortunately, ORR performance of reported $\text{Fe-N}_x/\text{C}$ catalysts is still far from the benchmark Pt/C catalysts, which may be linked with limited and inhomogeneous distribution of Fe-N_x active sites, low surface area and improper porous architecture. Interestingly, ZIFs offer a promising platform to fabricate well-organized porous structure accompanied by heteroatom-doped carbon (self-doped N) and high surface area.^[168] Therefore, inspired by the aforementioned traits, Chen et al. employed molecular-confined strategy for the synthesis of Fe/N/C catalyst via carbonization of $[\text{Fe}(\text{CN})_6]^{3-}@\text{ZIF-8}$ precursor (**Fig. 10 j**).^[86] Through this strategy, $[\text{Fe}(\text{CN})_6]^{3-}$ ion could be anchored into the pores of ZIF-8 crystal leading to provide resistance against sintering during carbonization. As a result, catalyst exhibited decent discharge-charge voltage gap, however, it lacked in cycling stability as opposed to the expectations (**Fig. 10 k**). Similarly, Deng et al. develop Fe-N_x incorporated open-porous carbon networks by employing ferric acetylacetonate and ZIF-8 polyhedrons.^[169] The ORR performance of the electrocatalyst was superior to that of benchmark Pt/C in alkaline solution, which may be associated with large surface area and high-density Fe-N_x moieties together with considerably high N content. Based on aforementioned studies, it could be inferred that the introduction of high fraction of g- C_3N_4 and Fe-N_x to ZIF-8 could promote ORR activity for ZABs.

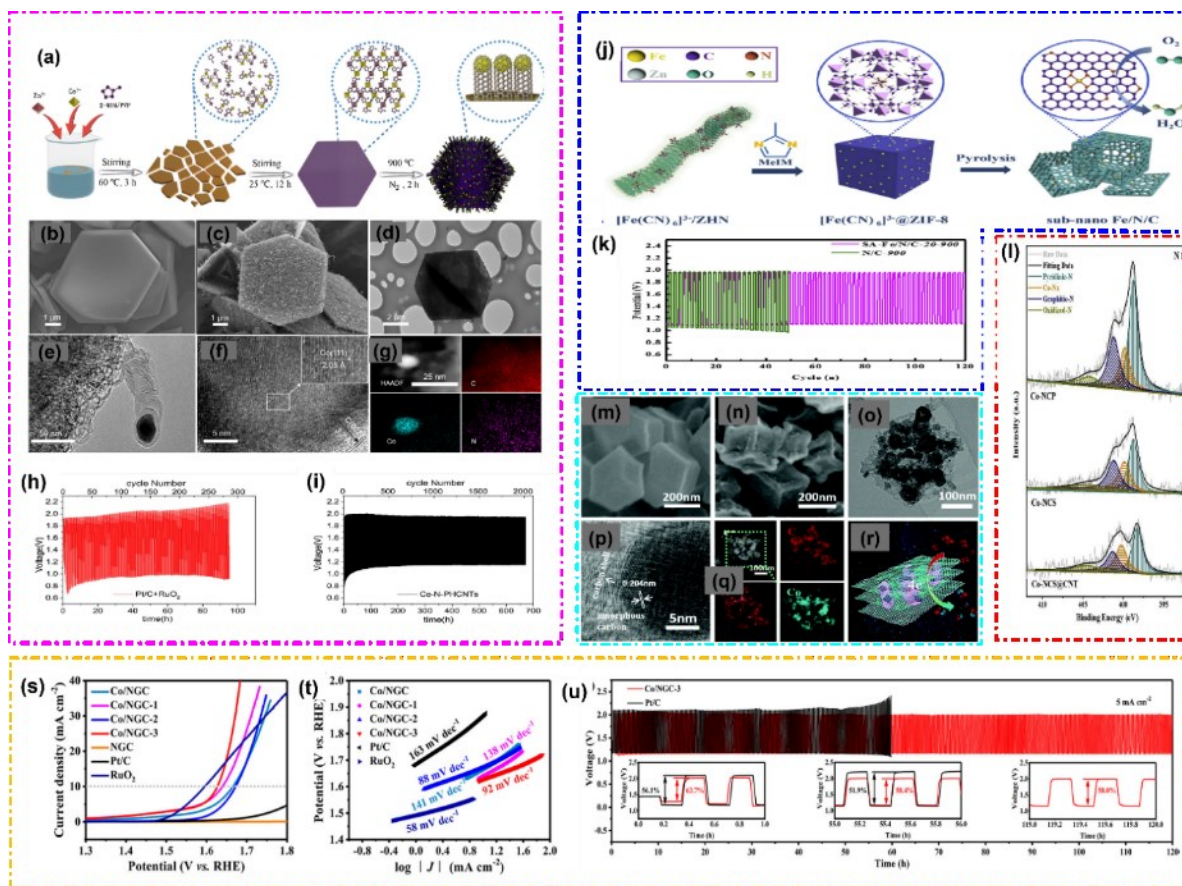


Fig. 10 (a) Schematic illustration of the synthesis of Co-N-PhCNTs. SEM images of (b) Co/Zn (1:1) ZIF-PhS and (c) its resultant Co-N-PhCNTs. TEM images of (d) Co-N-PhCNTs and (e) the Co encapsulated in the tips of the CNT derivative from the carbon layer (f) HRTEM images of Co-N-PhCNTs. (g) HAADF-STEM as well as EDS elemental mapping of Co/Zn (1:1) ZIF-PhS-derived Co-N-PhCNTs. (h) the noble-metal Pt/C + RuO₂ and (i) Co-N-PhCNT electrocatalysts at a current density of 5 mA cm⁻². Reproduced with permission.^[83] Copyright 2019, Elsevier Ltd. (j) Schematic procedure for the synthesis of sub-nano Fe/N/C. (k). Discharge/charge profiles of the Zn-air batteries with a duration of 300 s per cycle at 5 mA cm⁻². Reproduced with permission.^[86] Copyright 2019, Elsevier Ltd. ; (l) N 1s XPS spectra of Co-NCP, Co-NCS and Co-NCS@CNT. Reproduced with permission.^[84] Copyright 2019, Elsevier Ltd. (m) ZIF-67 obtained by s-Co@NCP/rGO and (n) ZIF-67 derived carbon materials in s-Co@NCP/rGO-800. (o) TEM and (p) HRTEM images of ZIF-67 derived from s-Co@NCP/rGO-800 precursor. (q) STEM of s-Co@NCP/rGO-800 with EDS mapping images. (r) The structural illustration of the s-Co@NCP/rGO-800. Reproduced with permission.^[85] Copyright 2020, The Royal Society of Chemistry. (s) OER polarization curves with the rotating speed of 1600 rpm; (t) Tafel plots (u) charging/discharging cycling performance at a current density of 5 mA cm⁻², insets: the initial and after long time cycling testing curves. Reproduced with permission.^[87] Copyright 2020, American Chemical Society

Besides Co, Ni and Fe, Cu is known to be compatible with several redox reactions because of its easily tuneable multiple valences viz. Cu (0), Cu (I), Cu (II) and Cu (III), excellent water stability and outstanding electronic conductivity^[170]. Moreover, theoretical calculations have anticipated that Cu demonstrates the highest ORR activity because it exists in the proximity to Pt at the topmost of volcano-plot.^[171] Therefore, inspired by these features, several studies have utilized Cu doped carbon

based materials like Cu@N-C^[172], Cu-N-C obtained by carbonizing Cu-containing ZIF-8^[173], Cu - N - C obtained by grafting Cu - N complexes, showed excellent ORR catalytic activity. Recently, Chen et al. designed Cu@Cu-N-C catalyst from Cu(OH)₂@ZIF-8, whereas encapsulated Cu(OH)₂ had gradually changed into Cu₂O with the rise in temperature (**Fig. 11 a**).^[170] The catalyst exhibited outstanding ORR catalytic performance, which may be credited to the synergistic effect between Cu nanoparticles and Cu(II)-N_x and large surface area of hollow carbon nanostructures. Likewise, Lai et al., synthesized porous Cu-N/C polyhedrons by pyrolyzing the Cu doped - ZIF - 8, possessing high surface area (1182 m² g⁻¹) and N content (11.05 at%).^[174] Furthermore, optimizing the Cu content may tune the valence state of Cu⁰ and Cu(II) leading to the formation of hybrid coordinated N-Cu(II)-Cu⁰ active sites. Consequently, 25% Cu-N/C catalyst exhibited high ORR activity and stable performance for Zn-air battery. As the ZIFs are susceptible to breakdown, leading to the aggregation following the pyrolysis and presenting the inadequate electronic conductivity.^[155b, 161] Therefore, leaf-like (ZIF-L-Co) architecture may also be designed with Cu incorporated catalysts to curtail aforementioned implications. To this end, Huo et al., reported CuCo - NC catalysts, obtained by the carbonization of a 2D leaf - like Cu(OH)₂/ZIF - L material (**Fig. 11 b**).^[88] Morphological studies reveal that Cu(OH)₂@ZIF - L - Co nanosheets adopt a leaf - like structure (**Fig. 11 c**). After pyrolysis, the catalysts retains their morphology with a reduction in thickness to 180nm. The obtained CuCo - NC catalysts demonstrated excellent ORR and OER activities even superior to that of commercially available Pt/C and IrO₂ catalysts, respectively. The high efficiency of the CuCo - NC catalysts in both ORR and OER is attributed to the synergistic effects of the CuCo alloy, high surface area, and high N content. The constructed Zn-air battery using the CuCo - NC catalyst showed an impressive performance, with a peak power density of 303.7 mW cm⁻², a large specific capacity of 751.4 mAh g⁻¹ at 20 mA cm⁻², a small charge/discharge voltage gap of about 0.84 V at 2 mA cm⁻², and a good recharging stability (**Fig. 11 d**). This work opens up new opportunities for designing and construction of bifunctional oxygen electrocatalysts by using 2D leaf - like Cu(OH)₂/ZIF - L materials for energy storage and conversion. By the same token, recently, Zhang et al. exploited the ZIF-L to design the yolk-shell architecture by employing ZIF-L based core and ZIF-8 based shell to encapsulate the tetraphenyl porphyrinato iron.^[175] The obtained FeCo-C/N air cathode displayed a low overpotential of (353 mV) at 10 mA cm⁻². However, long-time cycling stability of a rechargeable ZABs even at 2 mA cm⁻² was ordinary in contrast to the contemporary air cathodes.

It is customary to add some foreign non-metallic elements, for instance, phosphorus (P), boron (B), sulphur (S), bromine (Br) to ZIFs to upgrade the electrochemical performance in terms of OER and ORR.^[51, 142, 176] ZIFs have been utilized to dope heteroatoms owing to their tailorable architecture, high surface area, inexpensiveness and N-self doping.^[177] During thermal treatments of ZIFs, these non-metallic elements serve in two ways: these heteroatoms modulate the electronic distribution

within the carbon lattice and break their electroneutrality and assisting the kinetic process; Heteroatoms react with metal nodes and transforming them into metal compounds such as CoN_x and Co_xP_y .^[155b, 178] Thus the phosphidation of Co/N-C may lead to CoP/N-C hybrid system, which is a potential bi-functional electrocatalyst.^[179] Feng et al. fabricated hybrid CoP/NC catalyst, derived by combining polyacrylonitrile-cobalt acetate (synthesized by electrostatic spinning) and 2-methylimidazole in ethanol solution, followed by phosphidation.^[90] The morphological analysis revealed the in situ growth of CoP nanoparticles and the surface of PAN-Co(AC)₂ nanofibers was smooth and clean before the growth. On the other hand, the surface of nanofibers turned rough with the growth of ZIF-67 crystals. Thus, the in situ generated CoP nanoparticles onto the carbon nanofibers exhibited improved electronic conductivity and larger exposure of active sites as compared to their counterparts for bi-functional (OER/ORR) activity. However, the bi-functional activity and stability were not so impressive. As bromine possess the highest electronegativity and large atomic radius, therefore it is judicious choice to polarize the adjacent carbon atoms and inducing the partial charge by electronegativity difference. For this purpose, Dilpazir synthesized Br/Co/N Co-doped and defect-riched porous carbon network using ZIF-67 precursor.^[180] They employed dimethyldioctadecyl ammonium bromide surfactant as a capping agent in the course of hydrothermal preparation of ZIF-67, which after calcination produced Br heteroatoms and defective carbon network. As a result, Br/Co/N Co-doped and defect-induced carbon exhibited small potential gap of $\Delta E = 0.60\text{V}$. Likewise, Sun et al. obtained $\text{Co}_9\text{S}_8/\text{C}$ catalyst which was covered with conductive graphene nanosheets was synthesized by a simple solvothermal method and formed a stable double-carbon structure.^[181] $\text{Co}_9\text{S}_8/\text{C}$ catalyst displayed a low potential gap of $\Delta E: 0.88\text{ V}$, however, $\text{Co}_9\text{S}_8/\text{C}$ loaded ZABs could not maintain their activity over a longer period.

Recently, Ahn et al. effectively designed Co based 1D hybrid structure in which ultra small CoP nanoparticles were impregnated into S,P and N co-doped carbon material using ZIF-67 via in-situ synthesis and crosslinking method (**Fig. 11 e**).^[89] Morphological transformation (**Fig. 11 f**) witnessed that the nanoparticle of cobalt phosphide were supported by P, N and S co-doped carbon framework (SEM). Furthermore, S, N, P, C and P were evenly dispersed (EDX). The presence of Co_2P nanoparticles was identified by HRTEM having d - spacing of 0.19 nm (211), which were surrounded by graphitic carbon. In accelerated condition during OER, CoP nanoparticles transformed into CoO and decreases the anodic current supplied to carbon, which in turn ensured the stability of carbon material and retained the high electrocatalytic properties. By comparative analysis, it was revealed that CoP nanoparticles endowed the higher activity as well as stability in contrast to the CoP free carbon-rich catalysts. Eventually CoP nanoparticles anchored in S-, P- and N- co-doped carbon supports presented high bi-functional activity with $E_{1/2}$ of 0.90 V (ORR) and low potential 1.64 V to achieve a current density of 10 mA cm^{-2} (OER) and low potential gap of 0.86V. The resultant catalyst

performed stable charging/discharging performance over a period of 85h at 20 mA cm^{-2} even better than benchmark Pt/C catalyst (**Fig. 11 g**).

Interestingly, CoP nanoparticles may also be incorporated into Cu-N-C catalysts to further improve their electrocatalytic performance.^[182] Resultantly, these bimetallic phosphides demonstrate superb electrochemical features as a result of synergistic effect. However, these bimetallic composites undergo agglomeration and phase separation during high temperature pyrolysis.^[183] Therefore, Zhang et al. inserted Cu(II) ions into ZIF-67 using a polymer-coating method to furnish copper–cobalt phosphides (CuCoP) composite.^[91] Following phosphidation and pyrolysis, CuCoP nanoparticles were isolated by organic ligand and anchored into N-doped carbon frameworks (CuCoP-NC), avoiding the agglomeration and phase separation. Thus, the insertion of Cu into CoP composites can modulated the electronic configuration, subsequently optimized the energy barrier for the reaction and promoting the electrochemical performance.^[184]

In addition to phosphidation, ZIFs precursors may also be used for the production of metal selenide decorated into carbon framework. For instance, Meng and co-workers developed very first time a facile strategy for in situ pairing of $\text{Co}_{0.85}\text{Se}$ nanocrystals into N-doped carbon matrix ($\text{Co}_{0.85}\text{Se@NC}$) by using a technique of direct selenization of zeolitic imidazolate framework-67 (ZIF-67).^[92] As a result, a synergistic effect was developed between $\text{Co}_{0.85}\text{Se}$ and NC, led to an excellent oxygen evolution activity with a small overpotential and a notable stability. Moreover, $\text{Co}_{0.85}\text{Se@NC}$ also significantly contributed to hydrogen evolution reaction (HER) and oxygen reduction reaction (ORR), making it a tri-functional catalyst suitable for both water splitting and ZABs. The obtained $\text{Co}_{0.85}\text{Se@NC}$ catalyst presented a low cell voltage of 1.76 V to achieve a current density of 10 mA cm^{-2} and this catalyst as an air electrode in Zn–air batteries displayed a very small discharge–charge voltage gap of 0.80 V for 180 cycles. It may be evaluated that ZIF-derived Cu@Cu–N–C composite turned out to be the excellent ORR active catalysts which may be associated with the symbiotic interaction between Cu (0) and Cu(II)- N_x moieties. Moreover, when Cu was incorporated into leaf-like (ZIF-L-Co) to end up into CuCo alloy-based CuCo - NC catalyst, which exhibited excellent bi-functional electrocatalytic activity for ZABs. Moreover, when Cu was introduced into CoP, a decent bi-functional activity was generated, which may be credited to the semi-metallic character of CoP. Interestingly, when non-metallic atoms (S, P, Br and Se) were further doped into metallic system of ZIFs, Br doping to ZIF-67 and defect-rich carbon presented phenomenal bi-functional activity with $\Delta E = 0.60\text{V}$ (a bi-functional performance descriptor). Based on these valuable findings, these materials demonstrate bright prospects in designing the scalable and affordable air electrodes for ZABs on commercial scale.

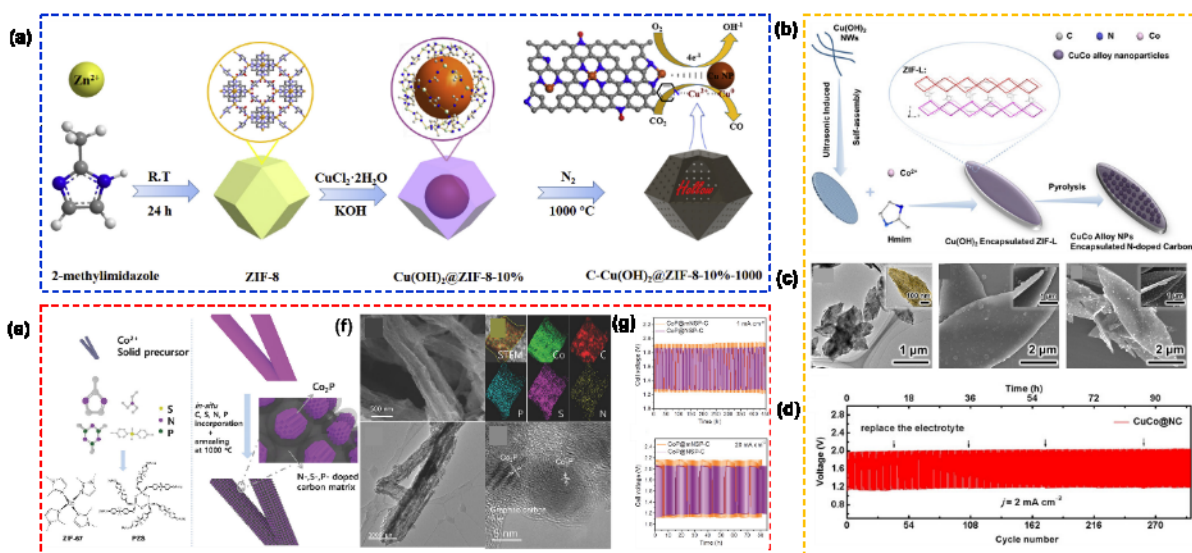


Fig. 11 (a) Schematic showing of evolution from ZIF-8 to C-Cu(OH)₂@ZIF-8-10%-1000. Reproduced with permission.^[170] Copyright 2019, Elsevier Ltd. (b) Schematic illustration of the preparation of CuCo@NC (c) TEM image of leaf-like Cu(OH)₂, SEM image of Cu(OH)₂@ZIF-L and SEM image of CuCo alloy NPs encapsulated N-doped carbon (d) Cyclic stabilities at 2 mA cm⁻² as well as long cycling test. Reproduced with permission.^[88] Copyright 2019, Wiley - VCH (e) Schematic illustration of the preparation of 1D cobalt phosphide embedded into a nitrogen, sulfur, phosphorus codoped carbon matrix (referred to as CoP@mNSP-C) with an integrated in situ zeolitic imidazolum framework - 67 (ZIF-67) conversion and crosslinking of poly(cyclotriphosphazene-co-4,4'-sulfonyldiphenol) (PZS) approaches (f) SEM images, STEM and corresponding elemental mapping images for Co, C, P, S, N of CoP@mNSP-C, TEM and HR-TEM images of CoP@mNSP-C (g) Cyclic stabilities of the ZABs with CoP@mNSP-C and CoP@mNSP-C air electrodes at an applied current density of 1 mA cm⁻² and 20 mA cm⁻². Reproduced with permission.^[89] Copyright 2017, WILEY - VCH.

3.1.2.2 Bimetallic transition metals-doped carbons

In contrast to the single transition metal carbide, bimetallic transition metal carbides have been demonstrated as promising catalysts for ZABs. Bimetallic transition metal carbides based on Co, Ni, Fe, Mo, W etc. have drawn a great deal of interest because these type of bimetals have synergistic effect and modulated the electronic properties, thus enhanced the overall catalytic activity and stability.^[185] Recently, Duan et al. fabricated hierarchical Fe₂Co@N-C bimetallic materials derived from Fe³⁺ and glucosamine-encapsulated ZIF-8/67 as illustrated in Fig. 12 a.^[186] Moreover, they evaluated the ORR and OER performance of FeCoN₈ using DFT computations and free energy diagrams as illustrated in Fig. 12 b. They concluded that the overpotential of FeCoN₈ was less than individual CoN₄ or FeN₄. Bimetallic Fe, Co carbides exhibited E_{1/2} of 0.896 V and a low overpotential (370 mV) at 10 mA cm⁻² for OER. Also, Fe,Co@N-C driven ZABs demonstrated excellent rechargeability with a low potential gap of 0.52V, yet it was not cyclic stable over a longer period (360 cycles for 60 h). Besides ZIF-8 or ZIF-67 precursors, Pendashteh and co-researchers designed Fe/Co based bimetallic air electrode using ZIF-9 as a precursor after Fe doping to Co-ZIF-9 via a

facile in situ solvothermal method as described in **Fig. 12 (c)**.^[187] When the resultant air electrode was assembled in rechargeable ZABs, it resulted high energy density ($1018 \text{ Wh}\cdot\text{kg}_{\text{Zn}}^{-1}$) as well as high specific capacity ($815 \text{ mAh}\cdot\text{g}^{-1}$). Moreover, ΔE , a bifunctional performance descriptor was also low 0.81 V , attributing to the excellent bi-functional activity. The optimal ZIF-9_Fe3_Pyrol catalyst derived from ZIF-9 demonstrated excellent bi-functional activity and was stable for 12h at 2 mA cm^{-2} during roundtrip performance evaluation. It is worth noticing that a very less explored ZIF-9- derived Fe/Co bimetal embedded in N-doped carbon nanotubes demonstrated an excellent bi-functional activity. It implies that some other ZIFs other than ZIF-8 and ZIF-67 (SOD topology) still likely to have the huge potential in achieving the bi-functional activity for ZABs. Therefore, it could also be deduced that besides different treatments of ZIFs and different types of metal nodes, ZIF type also play a major role in achieving the excellent performance of ZABs. Although ZIF-9 derived air electrode display excellent bi-functional activity, however, it was not stable over a longer period. Consequently, a significant improvement is required in ZIF-9 derived Fe/Co bimetal in terms of stability, to serve as an active and stable air electrode.

Interestingly, Changan et al. synthesized Ni_1Co_3 bimetal embedded in N-doped carbon nanotubes using by the introduction of Ni into Co containing ZIF-67 with a molar ratio of $1/3(\text{Ni}/\text{Co})$, demonstrated a remarkable potential gap of $\Delta E: 0.67 \text{ V}$ and charge/discharge cyclic stability for 200 h.^[188] The incorporation of Ni also contributed in controlling the pyridinic N species (42.6%). Obviously, Changan's contribution provided a new toolbox for the development of Ni containing high performing bimetallic ZIF based materials to serve as a bi-functional material for ZABs.

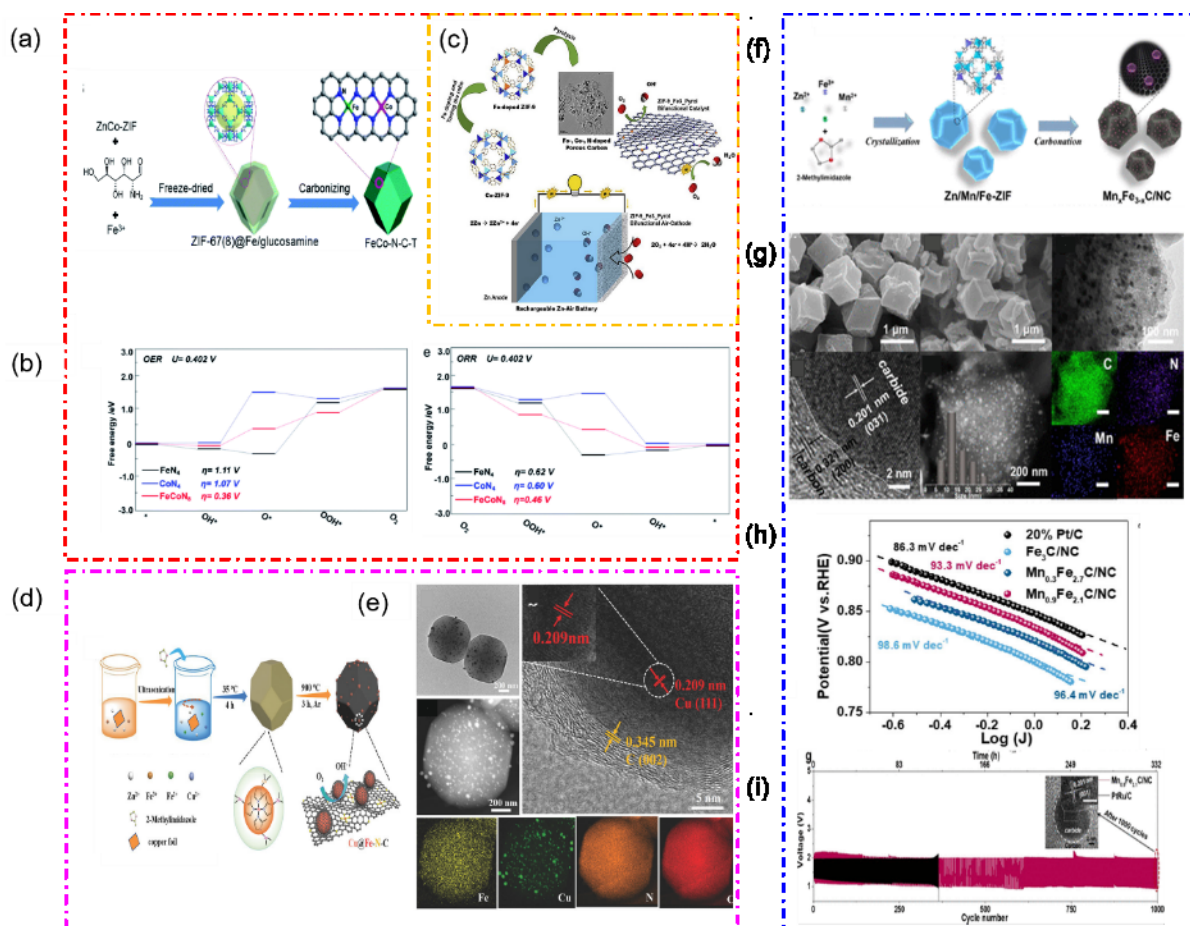


Fig. 12 (a) Synthesis scheme of FeCo-N-C-T (b) Free energy diagram of CoN₄, FeN₄ and FeCoN₈ at the equilibrium potential ($U_0 = 0.402$ V) for ORR and OER and ORR. Reproduced with permission.^[186] Copyright 2020, The Royal Society of Chemistry (c) Synthesis scheme for the preparation of Fe-doped Co-ZIF-9 and their loading in ZABs. Reproduced with permission.^[187] Copyright 2019, Elsevier Ltd. (d) Schematic of the synthesis procedure of Cu@Fe-N-C (e) TEM and HRTEM images of Cu@Fe-N-C and corresponding Fe, Cu, N, and C elemental mappings. Reproduced with permission.^[96] Copyright 2018, WILEY-VCH. (f) Schematic of the process used to synthesize Mn_xFe_{3-x}C/NC catalyst. The magnified view shows the structures of Zn/Mn/Fe-ZIF and Mn_xFe_{3-x}C/NC. (g) SEM and TEM image, high-resolution TEM images of Mn_{0.9}Fe_{2.1}C/NC catalysts, STEM image with its corresponding elemental mappings for C, N, Mn, and Fe. (h) Tafel slopes derived from ORR curves (i) Two-electrode rechargeable ZAB galvanostatic charge-discharge cycles with Mn_{0.9}Fe_{2.1}C/NC catalyst as the air electrode at the current density of 5 mA cm⁻². HR-TEM image of Mn_{0.9}Fe_{2.1}C/NC catalyst after 1000 galvanostatic charge-discharge cycles (inset). Reproduced with permission.^[91] Copyright 2019, American Chemical Society.

Another interesting study conducted by Wang et al. wherein they anchored Co nanoparticles inside the N-doped CNTs after carbonizing the precursor of 2D leaf-like Zn,Co-ZIF.^[97] As a result, the obtained bifunctional catalyst was found successful in both three electrode as well as two-electrode configuration for primary and secondary Zn-air batteries. Despite the narrow potential gap (0.79), the bi-functional activity of Co-N-CNTs catalyst was not excellent over a longer duration.

The development of Co-free bimetallic transition metals while exploiting their synergistic effect, is also considered as an effective strategy to confront the skyrocketed price of Co ($\$210 \text{ kg}^{-1}$), by using ZIF-8 and economical Mn ($\$1.75 \text{ kg}^{-1}$) and Fe ($\0.89 kg^{-1}) etc. metals.^[189] Therefore, Wang et al. facilely synthesized Cu@Fe - N - C catalyst, employing copper foil during ZIF-8 growth, followed by high temperature pyrolysis (**Fig. 12 d**).^[196] Actually, copper foil introduced Cu^{2+} and Fe^{2+} ($2\text{Fe}^{3+} + \text{Cu} \rightarrow \text{Cu}^{2+} + 2\text{Fe}^{2+}$) while minimizing oxidation of iron species (Fe^{2+} to Fe^{3+}) in the course of ZIF - 8 growth. It can be visualized through TEM micrograph that tiny nanoparticles were dispersed on the carbon matrix (**Fig. 12 e**). From High - resolution TEM (HRTEM), it can be further evaluated that Cu nanoparticles were surrounded by the shells of graphitic carbon as Cu@C. Elemental distribution of Cu, Fe, C and N was further elaborated by the elemental mapping, which depicts that Fe, C and N were thoroughly dispersed uniformly, whereas Cu was dispersed as nanoparticles. By virtue of its bimetallic active sites, large surface area, high level of nitrogen doping, and conductive carbon frameworks, Cu@Fe - N - C, displayed superior ORR performance to that of Pt catalysts in alkaline solution. Notably, Cu@Fe - N - C as a cathode exhibited a higher peak power density (92 mW cm^{-2}) and excellent stability.

As Iron carbide (Fe_3C) is known as uni-functional (ORR) electrocatalyst candidate because it exhibits poor OER activity^[190]. Therefore, Lin and co-researchers incorporated Mn into Fe_3C to modulate the electronic features of Fe_3C and the neighbouring carbon, leading to enhanced ORR and OER and producing Co free, cheaper electrocatalyst.^[3] As shown by **Fig. 12 f**, $\text{Mn}_x\text{Fe}_{3-x}\text{C}$ catalyst, well-armed by carbon layers, displayed high resistance to oxidation and corrosion. Also, N-doped porous carbon firmly anchored the $\text{Mn}_x\text{Fe}_{3-x}\text{C}$ nanoparticles, which efficiently suppressed the dissolution, oxidation and corrosion of binary metal carbide. As per SEM and TEM, $\text{Mn}_{0.9}\text{Fe}_{2.1}\text{C}/\text{NC}$ samples were found as a polyhedral shape (**Fig. 12 g**). HRTEM presented the lattice fringes featuring interspacing of 0.20 nm , attributing to the plane of Fe_3C (031). Moreover, EDS mapping illustrates the homogeneous distribution of N, Mn and Fe. The excellent ORR activity of optimal catalyst is also illustrated by the ORR Tafel slopes (**Fig 12 h**). As a result, the obtained catalyst demonstrated remarkable rate performance and excellent cyclic stability (1000cycles) as depicted by **Fig. 12 i**. Thus the fabrication of ZIFs-derived and Co-free transition metals have also directed the future research towards more economical and scalable production of air electrodes for ZABs.

3.1.2.3 Single metal atom modified carbons

It has already been established that the activity of a catalyst can be accelerated by rising the number of active sites. To this end, single - atom catalysts can be employed in a catalytic system to fully utilize the atomic efficiency based on size and exposure of active sites.^[191] Therefore, downsizing the transition metals to atomic scale increases the accessibility of exposed active sites and leading to the

enhanced intrinsic activity of catalysts.^[192] Nevertheless, the little control over the dispersion causes the migration and agglomeration of atomic species during pyrolysis treatment, which are the major challenges in realizing the single atom catalysts.^[94, 193] Interestingly, ZIFs with nanostructured carbonaceous scaffold enriched with N, based on the coordination bond between N-containing sites and atomically dispersed transition metals offer a rich platform to design single - atom catalysts, while addressing the issues of migration and agglomeration of atomic species.^[72a, 194]

Chen et al. developed Fe based single atomic sites, supported by carbon polyhedron co-doped by P, N and S heteroatoms, obtained through ZIF-8.^[100] The atomic structure of Fe-SAs/NPS-HC catalysts was investigated by X-ray absorption fine structure (XAFS) measurements, revealed that atomically dispersed Fe atoms possess partially positive charges because absorption edge of X-ray absorption near-edge structure (XANES) spectroscopy (**Fig. 13 a**) exists between Fe₂O₃ reference and Fe foil. Moreover, Fourier transform (FT) curve of extended X-ray absorption fine structure (EXAFS) (**Fig. 13 b and c**) and wavelet transform (WT) contour plots (**Fig. 13 d**), ratifying that Fe species existed in atomically dispersed form in Fe-SAs/NPS-HC, which further stabilized by co-ordinating with four N atoms as Fe-N₄ (**Fig. 13 e**). Fe-SAs/NPS-HC catalyst demonstrated excellent ORR activity with a half-wave potential ($E_{1/2}$) of 0.912 V in alkaline media. ORR performance kinetics of Fe-SAs/NPS-HC was elaborated by conducting DFT calculations of free energies of 4e⁻ ORR reaction mechanism (**Fig. 13 f**). Among three catalysts, the intermediates on Fe-SAs/NPS-C demonstrated the weakest binding energy. In addition, the reaction steps for 4e⁻ reduction path were seen on the down-hilled, indicating that ORR activity is likely thermodynamically feasible on Fe-SAs/NPS-C. Furthermore, the differences in charge density (**Fig. 13 g**) and Bader charge (**Fig. 13 h**) unveiled that co-doping of S, P and N atoms is capable of donating electrons to Fe atoms, rendering it less positive (Fe^{δ+}) so that it had the weak binding of adsorbed (OH⁻) species. Consequently, Fe-SAs/NPS-HC catalyst displayed excellent rechargeability for Zn-air battery (**Fig. 13 i**) because it delivered lower charging-discharging potential gap (charging: 2.07V; discharging: 1.11V) and outstanding stability after 500 charging/discharging cycles (200,000 s). Similarly, Zhang and co-workers designed FeN₄ atoms, dispersed in hierarchically porous N-doped carbon after the calcination (900 °C) of ferrocene-encapsulated ZIF-8 as shown in **Fig. 14 (a)**.^[98] Morphological features also revealed the hierarchical porous structure possessing open windows in the spherical voids (**Fig. 14 b**). EXAFS wavelet transforms plot and fitting results also confirmed the existence of Fe atoms as mononuclear centers which coordinated with N (four atoms) as illustrated by **Fig. 14 c and d**. The resultant catalyst displayed excellent ORR catalytic activity with $E_{1/2}$ of 0.875 V and 0.784 V in alkaline and acidic media respectively. Chen's contribution presented Fe based single atom catalyst and doped with several heteroatom (P, N and S) derived through ZIF-8. ^[100] It provided a comprehensive understanding of Fe based single-atom transition metal catalysts consisting of P, N and S heteroatoms

with the help of DFT calculations of free energies. Thus this work will provide a guideline to the new researcher for designing the heteroatom doped single atom catalyst derived through ZIFs for ZABs.

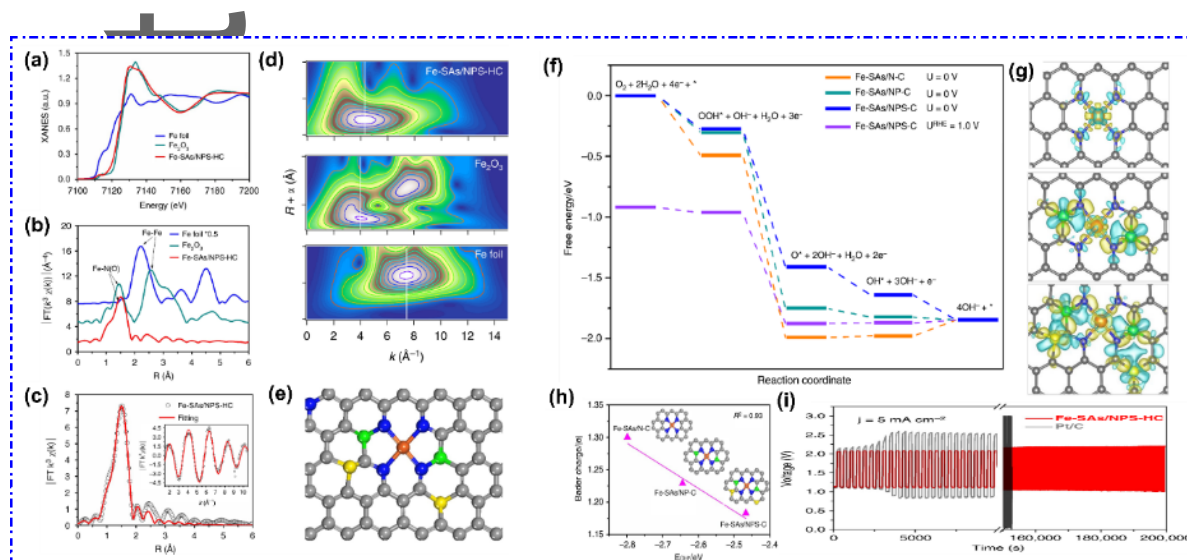


Fig. 13 Atomic structural analysis. Fe *K*-edge X-ray absorption near-edge structure (XANES) spectra (a) and Fe *K*-edge k^3 -weighted Fourier transform (FT) spectra (b) of single Fe atomic sites supported on a N, P and S co-doped hollow carbon (Fe-SAs/NPS-HC), Fe foil and Fe_2O_3 samples, respectively. (c) The corresponding EXAFS; *R* space fitting curves; inset: The corresponding EXAFS *k* space fitting curves of Fe-SAs/NPS-HC. (d) Wavelet transform (WT) of Fe-SAs/NPS-HC in contrast to Fe foil and Fe_2O_3 samples, respectively. (e) Schematic model of Fe-SAs/NPS-HC, Fe (orange), P (green), C (gray), N (blue), and S (yellow). (f) Free energy diagram of ORR on single-atom iron (Fe-SAs)/N-doped carbon (N-C), Fe-SAs/N, P co-doped carbon (NP-C) and Fe-SAs/nitrogen, P, S co-doped carbon (NPS-C) ($U^{\text{RHE}} = U^{\text{NHE}} + 0.0591 \text{ pH}$; $U^{\text{RHE}} = 0 \text{ V}$, $U^{\text{NHE}} = -0.77 \text{ V}$; $U^{\text{RHE}} = 1 \text{ V}$, $U^{\text{NHE}} = 0.23 \text{ V}$). (g) Calculated charge density differences of Fe-SAs/NP-C, Fe-SAs/N-C and Fe-SAs/NPS-C. Blue and yellow areas represent charge density rise and reduction, respectively. The cut-off of the density-difference iso surfaces is equal to 0.01 electrons \AA^{-3} . (N: blue, C: gray, P: green, Fe: orange, S: yellow). (h) Linear correlation between Bader charge of single-atom Fe and OH^* binding energy in Fe-SAs/NP-C, Fe-SAs/N-C and Fe-SAs/NPS-C. (i) Cyclic stabilities of Fe-SAs/NPS-HC-based and 20 wt% Pt/C-based ZABs. Reproduced with permission.^[100] Copyright 2018, Springer Nature

Zang et al. fabricated Co single atoms electrocatalyst wherein Co single atoms were implanted in the flakes of N-doped porous carbon through the carbonization-acidification treatments of ZIF-67 precursors as shown in **Fig. 14 e**.^[99] After the acid leaching, Co metal clusters were removed and led to the single atom catalyst with extra porosity and active surface area. Eventually, they inferred that Co-N_x single atom catalysts demonstrated superior OER/ORR performance (**Fig. 14 f**) and reasonable charging/discharging cyclic stability (180h) as compared to Co-N_x catalysts containing the abundant Co nanoparticles (**Fig. 14 g**). Thus, they established that Co clusters are redundant and have no role in catalysing the ORR as well as OER activities. Similarly, Sun et al. fabricated cobalt single-atom using Urchin-like nanotube hierarchical structures derived from ZIF-67 by “sacrificial template” method.

Excellent bifunctional activity (ORR/OER) leading to the rather lower ΔE value (0.72 V), which stemmed from the coordination of carbon matrix and CoN_4 in the urchin-like architecture ^[43d].

Han et al. synthesized $\text{Fe-N}_x\text{-C}$ single-atom electrocatalyst.^[101] Firstly, Fe-Phen complexes was prepared by the co-ordination of Fe^{2+} ions and 1,10-phenanthroline, followed by the in situ encapsulation in ZIF-8 nano cages, eventually pyrolyzing under inert atmosphere at 900 °C. As per the high resolution XPS spectrum of N, graphitic and pyridinic N coexist in the $\text{Fe-N}_x\text{-C}$ catalyst (Fig. 14 h), wherein Pyridinic N offers coordination sites for atomic Fe (Fe-N_x) whereas graphitic N influences the morphology and electronic configuration of carbon matrix. The N binding states are schematically described in (Fig. 14 i). It is reported that graphitic N contributes positively in upgrading the limiting current density of the $\text{Fe-N}_x\text{-C}$ catalyst towards ORR.^[195] As a result, ΔE for $\text{Fe-N}_x\text{-C}$ catalyst was found to be 0.92 V, which signifies the bifunctional catalytic activity towards OER as well as ORR (Fig. 14 j). However, it is obvious from Tafel slope (Fig. 14 k) that OER activity of $\text{Fe-N}_x\text{-C}$ catalyst is not so impressive which leads to the higher potential gap during the testing of rechargeable Zn-air battery. $\text{Fe-N}_x\text{-C}$ catalyst runs for discharging/charging cycles for 300h at current density of 5 mA cm^{-2} and for 250h at current density of 10 mA cm^{-2} (Fig. 14 l).

Similarly, Ma et al. designed single site Fe-N_x active species distributed in nitrogen-doped porous carbon via pyrolysis of polypyrrole coated graphene@ Fe-Bipy embedded ZIF-8.^[43c] It is worth mention that Fe-N_x species predominantly contributed to ORR, wherein an iron atom was coordinating with six N atoms as illustrated by N1s and Fe_{2p} of XPS (Fig. 14 m). The obtained catalyst demonstrated small charging/discharging potential gap of about 0.78 V at $5 \text{ mA}\cdot\text{cm}^{-2}$ for 40h (220 cycles) together with high power density of around $118 \text{ mW}\cdot\text{cm}^{-2}$. The superior performance may be attributed to the 3D architecture consisting of 2D graphene and ZIF-8 derived porous N-doped carbon with abundant large pores, supplying abundant active sites and excellent electronic conductivity.

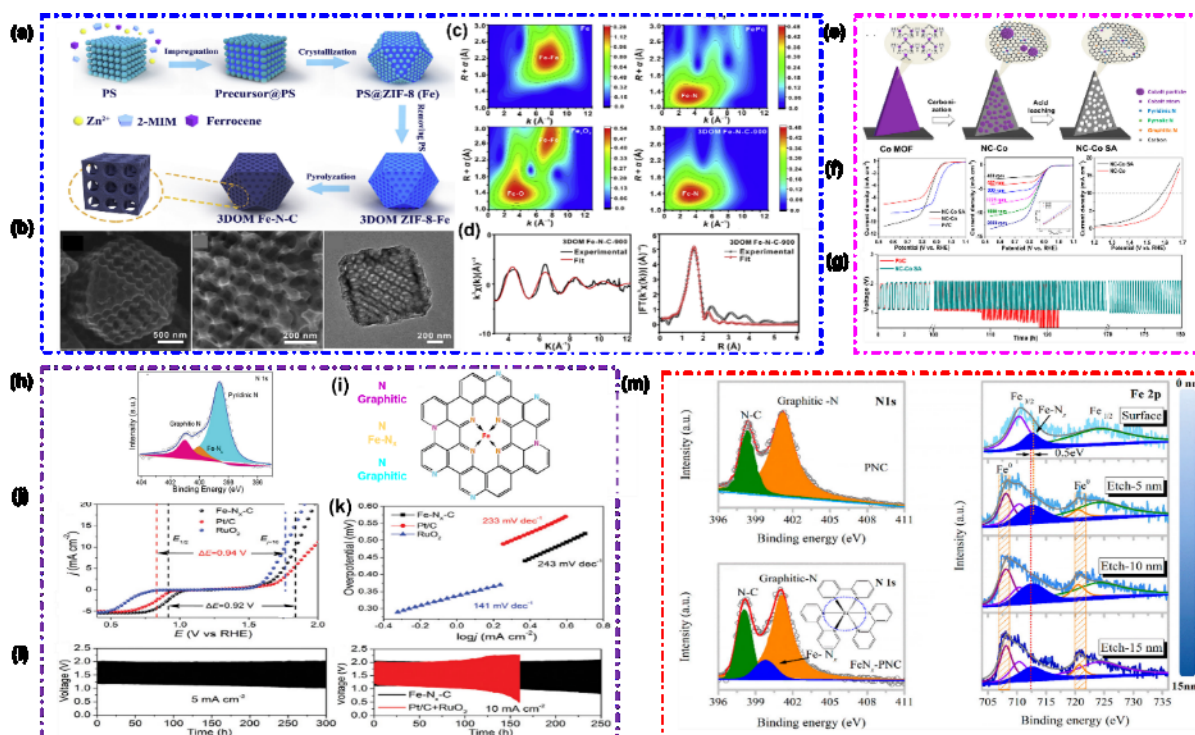


Fig. 14 (a) A series of schematic diagrams for illustrating the synthesis of 3DOM Fe–N–C samples (b) Typical SEM and TEM images of 3DOM Fe–N–C-900. (c) WT-EXAFS of Fe foil, FePc, Fe₂O₃ and 3DOM Fe–N–C-900. (d) The corresponding EXAFS fitting curves of 3DOM Fe–N–C-900 at k space; Fitting of the magnitude of the Fourier transform of the k₂-weighted EXAFS (data-black and fit-red) for the 3DOM Fe–N–C-900 catalyst. Reproduced with permission.^[98] Copyright 2020, Elsevier Ltd. (e) Schematic illustration of fabrication process, local magnification of obtained materials. (f) ORR polarization curves at 1600 rpm, ORR polarization curves of NC-Co SA at various rotation and corresponding Koutecky–Levich plots, Oxygen evolution curves. (g) Stability test of aqueous rechargeable Zn–air batteries using NC-Co SA and Pt/C as the air cathodes. Reproduced with permission.^[99] Copyright 2018, American Chemical Society. (h) XPS spectrum of N 1s. (i) Illustration of N species in the carbon framework (j) Overall polarization curves of Fe - N_x - C, commercial Pt/C, and commercial RuO₂ in 0.1 m KOH; (k) Tafel plots for OER; l) Cycling test at a current density of 5 mA cm⁻² with Fe - N_x - C catalyst and Cycling test at a current density of 10 mA cm⁻² with Fe - N_x - C and Pt/C+RuO₂ mixture catalysts, respectively. Reproduced with permission.^[101] Copyright 2019, WILEY - VCH . (m) XPS spectra of N 1s for PNC and FeN_x-embedded PNC.XPS depth profile of Fe 2p for FeN_x-embedded PNC at different etching depths (0–15 nm). Reproduced with permission.^[43c] Copyright 2018, American Chemical Society.

As it is the general practice to employ the binders for the preparation of cathode materials, however, the binders are usually known as insulators or inactive materials, leading to the poor catalytic performance.^[196] Therefore, it is believed that catalysts directly grown on binder-free conductive substrates may demonstrate several intrinsic benefits such as high conductivity, reduction in diffusion length and controlled micro/nanostructures. To curtail this challenge, Ji et al. directly grown carbon nanoflakes supported Co single atoms on electro-spun 3D carbon nanofiber as a conductive substrates obtained by immersing PAN nanofibers into solution consisting of precursors of ZIF-67.^[103] The field emission scanning electron microscope (FESEM) micrographs demonstrate that Co SA@NCF/CNF film is consisting of several interconnected microfibers extended to the hundred micrometers in length (Fig. 15 a). The inter - fiber pores facilitate the convenient transport of reactants and electrolyte.

Moreover, ZIFs-derived carbon flakes with open mesopores enclosing the carbon nanofibers (**Fig. 15 b**). The bifunctional catalytic activity ($\Delta E = E_{j=10} - E_{1/2}$) of Co SA@NCF/CNF was corresponding to 0.75 V (**Fig. 15 c**), which was smaller than that cobalt cluster based Co NP@NCF/CNF (0.85 V), and even outperformed the state-of-the-art precious metals such as Pt/C: 1.13 V; Ir/C: 0.94 V (**Fig. 15 d**). Thus, the removal of Co clusters efficiently minimizes the metal size and simultaneously increases the surface area of the hierarchically porous structure. As a result, Co clusters removal and easily accessible Co active sites supported by N doped porous carbon exhibited excellent bi-functional activities. In addition, DFT calculations demonstrated that Co single atomic sites supported on conductive substrates had lower OH* hydrogenation barrier in comparison to that of Co clusters, which greatly contributed to the overall ORR/OER performance.

Generally prepared atomically dispersed metal atoms utilize a very low metal mass loading (<1.5%) to get around the agglomeration and maintaining the uniform dispersion by employing the bottom-up strategy.^[82, 193a, 197] Nevertheless, for an ideal single atom catalyst, atomic dispersion should be densely high on a stable substrate. Therefore, Wu et al.^[104] described salt - template strategy for the synthesis of largely populated N - doped and carbon supported monodispersed Co atoms (**Fig. 15 e**). This method was found as effective because they succeeded to manage a larger site fraction of 15.3% of Co atoms, which translated into excellent bi-functional activity. Furthermore, experimental measurements and DFT based simulations emphasized that Co-N₄ active sites on the carbon matrix are responsible for the bifunctional oxygen electrocatalytic activity (**Fig. 15 f and g**). Similarly, to get the higher loading of single atom Fe as high as 3.8 wt% and to ensure the efficient isolation of single Fe atoms, Wei et al. introduced a host-guest strategy (Fe-TPP@rho-ZIF) based on tetraphenylporphyrin iron (Fe-TPP) and ZIF with the rho topology using one-pot solid state grinding synthesis.^[102] Fe-TPP molecules were successfully confined in rho-ZIF instead of conventionally used sod-type ZIF-8 because sod-type ZIF, possessing small pore size (~12 Å)^[198] and is not capable of accommodating large Fe-TPP molecule (~17.2 Å). On the other hand, ZIFs with rho-type topology have larger interior (~22 Å) to accommodate large Fe-TPP molecules (**Fig. 15 h**).^[199] Following the pyrolysis, Fe centres were isolated and atomically dispersed in the carbon matrices, forming Fe-N₄ active sites. The fitting curves in r-space as well as k-space as shown in **Fig. 15 (i) and (j)** also reveal that one isolated Fe atom was found to have coordination with four N atoms, while one O₂ molecule may be adsorbed over the Fe atom normal to Fe-N₄ plane. As a result, benefitting from the outstanding structure and composition, the resultant Fe-N/C demonstrated superb ORR activity and high durability.

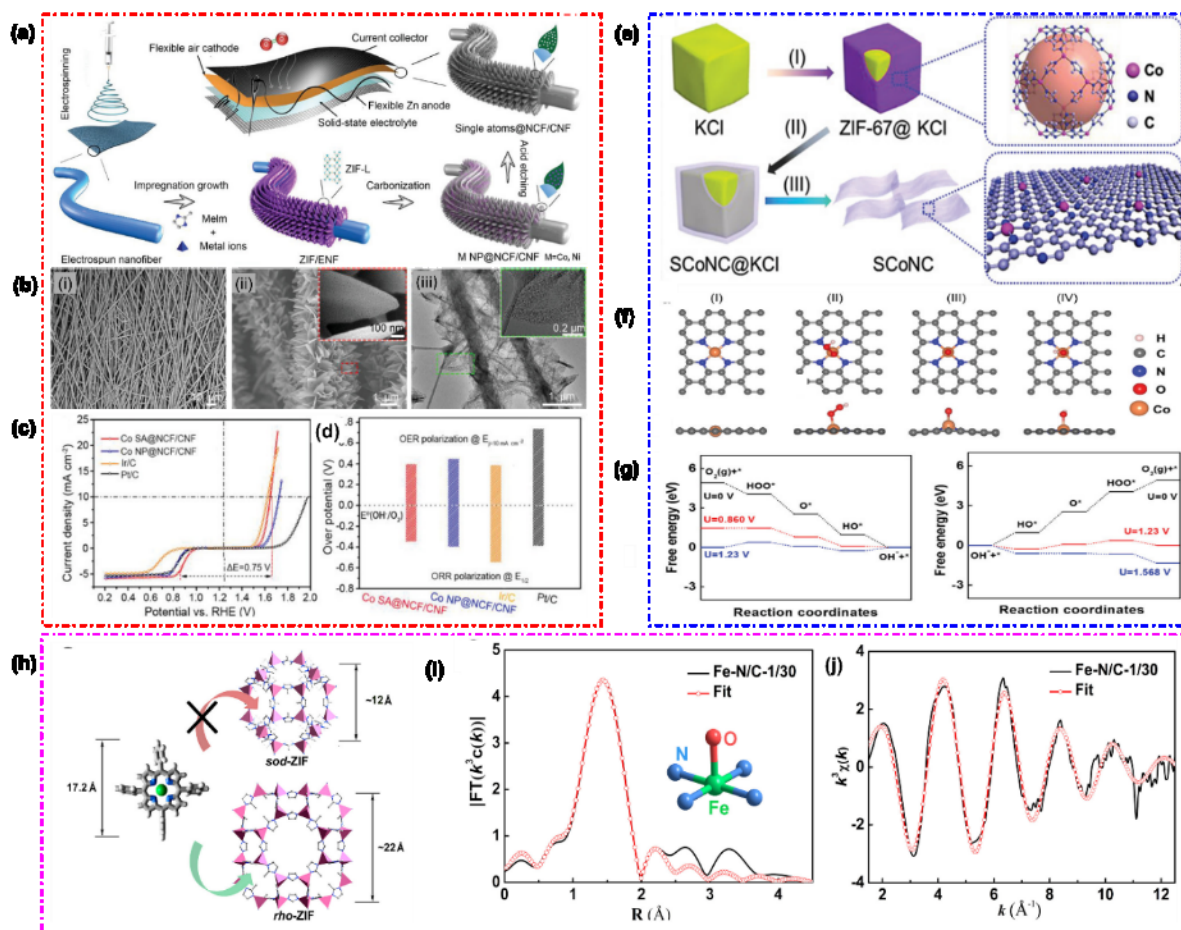


Fig. 15 a) Schematic representation of the “impregnation - carbonization - acidification” process for scalable fabrication of M SA@NCF/CNF film as flexible air cathode in a wearable Zn-air battery (b) (i), (ii) FESEM, (iii) FETEM (c) ORR/OER bifunctional LSV curves of Co SA@NCF/CNF, Co NP@NCF/CNF, Ir/C, and Pt/C. (d) Comparison of oxygen bifunctional catalytic performances of Co SA@NCF/CNF and reference samples. Reproduced with permission.^[103] Copyright 2019, WILEY - VCH. (e) Schematic illustration of the synthetic procedure of the SCoNC catalysts. (f) Top view and side view of the initial structure (I) and structures after adsorption of OOH* (II), O* (III), and OH* (IV), respectively. (g) Free energy for ORR and OER on Co□N₄ structure at different electrode potential U. For ORR, at the equilibrium potential (U = 1.23 V) the reaction steps are uphill in free energy, while at 0.860 V all reaction steps are downhill in free energy. For OER, all water splitting reaction steps become exothermic at potentials above 1.568 V. Reproduced with permission.^[104] Copyright 2019, WILEY - VCH (h) Fe-TPP molecule, sod- and rho-ZIF cages from single-crystal XRD structure with ZnN₄ pink tetrahedra (double-sided arrows indicate their sizes). Fitting curves of the EXAFS of Fe-N/C-1/30 in (i) r-space and (j) k-space. Reproduced with permission.^[102] Copyright 2018, Elsevier Ltd.

3.1.2.4 Alloys/carbon composites

Carbon supported transition metal based alloys have drawn considerable attention owing to their excellent stability, low price and elevated bi-functional (OER/ORR) activity.^[200] Alloys in MOF-derived carbon based electrocatalysts can better tune electronic structure of surrounding carbon atoms

through modulation effect, contributing to enhanced OER as well as ORR activity^[201]. Therefore, ZIFs are the versatile platforms to host Ni-Fe, FeCo, etc. alloys into N-doped porous carbon network.

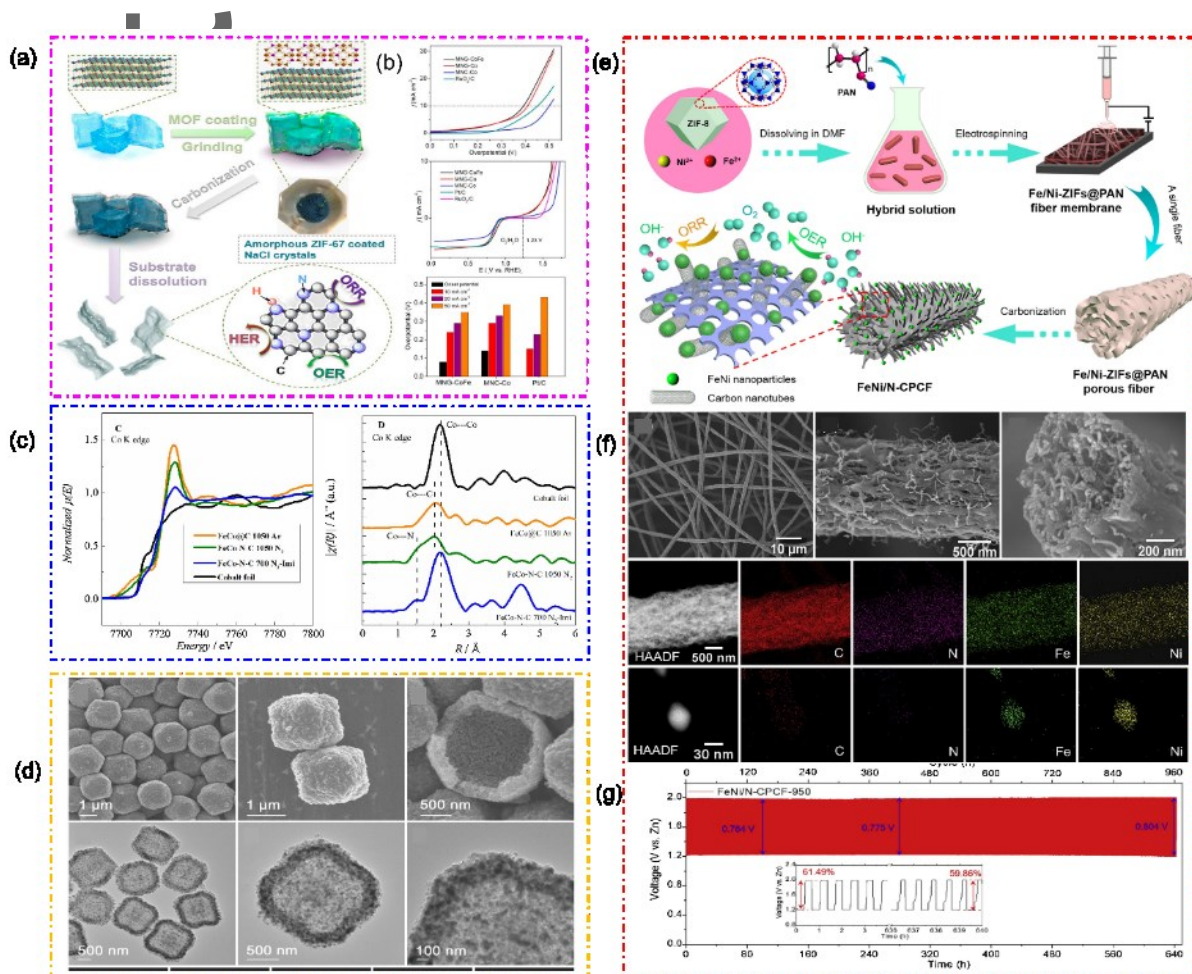


Fig. 16 (a) Synthesis Scheme of mesoporous nitrogen-doped graphene; (b) LSVs for OER with iR compensation; LSVs for both ORR and Overpotential at the different current density and onset potential for HER. Reproduced with permission.^[46a] Copyright 2018, American Chemical Society; (c) XANES- Fourier Transform of the EXAFS oscillations, k^3 -weighted at the Fe (7112 eV) and Co (7709 eV) K edges for some selected electrocatalysts. Reproduced with permission.^[202] Copyright 2019, Elsevier Ltd. (d) FESEM and TEM images of Fe_{0.3}Co_{0.7}/NC cages Reproduced with permission.^[121] Copyright 2018, WILEY - VCH ; (e) Synthesis scheme for the FeNi/N-CPCF membrane and its morphology ; (f) SEM images, HAADF-STEM image, and corresponding EDS elemental mapping of FeNi/N-CPCF-950 (g) Schematic illustration of the liquid ZAB configuration and galvanostatic cycling stability of ZABs with FeNi/N-CPCF-950 catalyst at a current density of 10 mA cm⁻². Reproduced with permission.^[123] Copyright 2019, Elsevier Ltd.

Niu et al. introduced a strategy to develop sheet-like mesoporous nitrogen-doped CoFe alloy nanoparticles encapsulated by graphene (MNG-CoFe) on NaCl substrates, derived from ZIF-67 fibres as a precursor synthesized in solid phase (Fig. 16 a).^[46a] MNG-CoFe catalyst performed as a multifunctional electrode and its electrocatalytic performance was far better than the platinum group metals. MNG-CoFe nanoparticles demonstrated outstanding OER, ORR, and HER activities (Fig. 16 b) as an outcome of higher electrochemical active surface area and optimal properties of graphitization degree and electronic conductivity. Furthermore, these electrocatalysts presented a high power density

and impressive rechargeability. Notably, nitrogen dopants as well as CoFe nanoparticles surrounded by carbon are capable of synergistically upgrading the catalytic performance on the carbon surface. The incorporation of trace Fe element into Co particles enclosed by the N-doped carbon leads to the shortage of electrons in Co 2p orbital. Actually, the electron density of Co 2p orbital decreases when Co NPs were alloyed with Fe because encapsulated Co into carbon layers transfer more electrons to the carbon surface causing the reduction in work function. It is likely that it leads to the rise in activity of surface carbon together with contribution from N, leading to the rise in activity of surface C. ^[106] The potential gap (ΔE) between half-wave potential (ORR) and potential in achieving the 10 mA cm⁻² (OER) was corresponding to 0.64 V, signifying the outstanding bi-functionality. In spite of excellent bi-functional activity, the catalyst was not stable for longer period. Therefore, it is important to enhance the stability of ZIF-derived CoFe alloy to utilise the advantage of phenomenal bi-functional activity. Similarly, Guan et al. presented porous Fe–Co alloy/N - doped carbon cages by using ZIF - 8@FeOOH/ZIF - 67 via “MOF - in - MOF hybrid” confined pyrolysis approach. ^[121] The most prominent feature of this strategy was to simultaneously grow MOF and to encapsulate the functional materials to render highly complex composite of MOF precursors. From the FESEM images of Fe_{0.3}Co_{0.7}/NC particles, the sample preserved its morphology even after the carbonization. It can be further elaborated by the TEM that the caged-shape particles were created by the decomposition of core (ZIF-8) during which Zn was completely evaporated (**Fig. 16 d**). Furthermore, in-situ formed Fe–Co alloy nanoparticles catalyzed the formation of N-doped carbon shell derived from organic species. Fe–Co alloy/N - doped porous carbon cages displayed superior electrochemical performance, attributed to the bimetallic active sites, protected by robust porous N - doped carbon composite.

Galiote et al. also developed FeCo@NC, synthesized by the precursor of ZIF-67 (cobalt nitrate, 2-methyl imidazole) and iron nitrate. ^[202] They substantiated by EXAFS results that high electrocatalytic activity towards ORR approach that of platinum nanoparticles, which may be correlated with the generation of metal coordinated species with N-doped graphitic carbon matrix (derived from 2-methyl imidazole) (**Fig. 16 c**). Actually, the highest ORR activity of FeCo@NC may be endowed with nitrogen-rich 2 MIM molecules because 2 MIM molecules provided well-dispersed metallic species on carbon surface; 2 MIM also supplied high density of nitrogen atoms. ^[203] They reported the outstanding ORR activity of FeCo@NC, which could be credited to the N-rich imidazole molecule. They provided a new insight for the ORR activity of ZIF-67 derived material and for their application in ZABs and other broad application in electrocatalysis. Wu et al. synthesized FeNi alloy by employing MOF precursor and polymer encapsulation method ^[122]. By modulating the Fe loading, carbon nanotube anchored with FeNi alloy nanoparticles were obtained, which subsequently assisted in developing the conductive network for the diffusion of OER/ORR related species. However, the electro-catalytic performance of bimetallic alloys still posing the inferior stability due to dissolution of

metals following the repeated redox operations. To address this issue, Wang et al. embedded the FeNi alloys in nitrogen-doped carbon via electrospinning, which after the carbonization of Fe/Ni-ZIF-8 at 950 °C grafted with bamboo-like CNTs (**Fig. 16 e**).^[123] The microstructure and morphology resultant FeNi/N-CPCF-950 was examined by field-emission scanning electron microscopy (FESEM) (**Fig. 16 f**), which revealed that the fibers of FeNi/N-CPCF-950 were connected with each other. Interestingly, high-resolution SEM image of FeNi/N-CPCF-950 further showed that several CNTs were interwoven on the carbon fiber which enable the charge transport very swiftly. On the other hand, EDS elemental mapping demonstrated the homogeneous dispersion of Ni and Fe N-doped porous carbon network, validated the formation of FeNi alloy. The FeNi alloys was secured from the electrolyte erosion by graphene layers, and N-doped carbon species. N-doped porous carbon is favourable for O₂ transport during charging and discharging process. In case of ORR, it serves as the tentacle to capture O₂ from oxygen saturated electrolyte and absorption on catalysts surface whereas multiple pores and active sites on carbon fibers are useful for OER process.^[204] The synergy among these components generate abundant active sites, while the combination of FeNi alloys and N-doped CNTs-entangled carbon matrix also alter the surface electronic structure and optimize the oxygen adsorption/activation energy, as well as facilitate the effective electron/ion transport. The combination of N-doped CNTs and FeNi alloys developed synergy, which modulated the electronic configuration and adsorption/activation energy for efficient ion/electron transfer. As a result, the obtained catalyst exhibited excellent ORR ($E_{1/2}=0.867$ V) and OER ($E_{j=10\text{ mA cm}^{-2}}=1.585$ V), superseding state-of-the-art Pt/C and RuO₂ catalyst (**Fig. 16 g**). Furthermore, the catalyst also showed outstanding charging-discharging cycling performance (640 h) for 960 cycles at 10 mA cm⁻² with a potential gap of 0.764 V (**Fig. 16 g**). Thus N-doped CNTs and FeNi alloys derived through ZIF-8 stand out among the advanced ZIF-derived air electrodes, demonstrating best OER/ORR performance for their application in rechargeable ZABs. Consequently, this catalyst has enormous potential for its applicability on commercial scale as air electrode in ZABs.

3.1.2.5. Transition metal oxides/carbon composite

Transition metal oxides are favourable electrocatalysts for the OER activity; however, they undergo particle aggregation and exhibit poor electronic conductivity.^[205] In this scenario, ZIFs are the most appropriate choice to tackle these issues. Upon carbonization of ZIFs, finely dispersed nanoparticles of metal oxides prominently exposed while embedding into N- doped porous carbon framework.^[158] For instance, Guan et al. anchored the hollow nanospheres of Co₃O₄ into N-doped porous carbon derived from Co-MOF (precursors of ZIF-67) on carbon cloth.^[94] Onion like carbon coating over the Co nanoparticles restricted the Kirkendall effect, leading to the transformation into hollow polycrystalline Co₃O₄ nanospheres. It can be observed from coloured STEM HAADF/ABF images that the hollow feature (i.e. core) is darker and somewhat irregular with varying shell thickness in different directions

(**Fig. 17 f**). On the other hand, the shell consisting of Co_3O_4 nanosphere is still surrounded by the graphitic layers, implying that the carbon coating in the form of onion was fairly retained during solid Co nanoparticles transformation to hollow Co_3O_4 nanospheres. FFT image illustrates the particular polycrystalline characteristics with the concomitance of polycrystalline Co_3O_4 as well as carbon. NC- Co_3O_4 catalyst demonstrated the bi-functional activities with a high $E_{1/2}$ value corresponding to 0.87 V and around 1.58V to achieve a 10 mA cm^{-2} of current density (OER), making up a voltage gap of 0.71V. Eventually, NC- Co_3O_4 - 90 exhibited outstanding stability without any decline in performance over a period of 120h (**Fig. 17 g**). Similarly, Zhao et al. found porous Co_3O_4 nanoparticle as air electrode followed by the pyrolysis of ZIF-67 at 450 °C in the atmosphere air. The obtained catalyst presented charging-discharging cyclic stability for 50 h at 2 mA cm^{-2} yet it was not so impressive.^[206]

Jiang et al. reported a hybrid tri-phase electrocatalyst consisting of interpenetrating spinel Co_3O_4 and Co nanoparticles anchored in a porous graphitic carbon developed via ion exchange as well as redox reaction between Co^{2+} ions, Zn^{2+} and 2MIM ligands (**Fig. 17 a**).^[207] Three interpenetrating phases, Co metal, Co_3O_4 spinels and N-doped carbon developed highways for the efficient charge and mass transport. The strong coupling through covalent bond between Co metallic species and N protected the Co species against leaching. In addition, defect sites at the interfaces served as atomic-traps to enhance adsorption capacity of O_2 . The resultant catalyst demonstrated low potential of 1.58 V for OER and half wave potential of 0.89 V with a potential gap (ΔE) of 0.69 V (**Fig. 17 b and c**). For Zn-air batteries, the catalyst sustained for charging/discharging cycle for 800 h at 10 mA cm^{-2} , superior to that of benchmark Pt/C catalyst (**Fig. 17 d and e**). In this study, Co_3O_4 spinels embedded in N-doped porous carbon together with interfacial defect sites tangibly contributed to the bi-functional activity of ZABs. It implies that this study provide a new understanding of application of Co_3O_4 spinels and their facile decoration in the N-doped porous carbon network. Thus, this strategy may be recapitulated in other electrocatalysis applications to achieve the OER/ORR bi-functional activity. Recently, bimetallic oxides, such as CoFe, CoMn, FeNi oxides, have been demonstrated extensively the enhanced OER and ORR activities.^[208] Therefore Chong and co-researchers developed $\text{Co}_{1-x}\text{Fe}_x\text{O@NC}$, 1D/2D hierarchical nanostructures through hydrothermal synthesis of coordination growth of 2D $\text{Co}_{1-x}\text{Fe}_x$ -ZIF nanosheets, transformed after the releasing of Co and Fe ions from $\text{Co}_{1-x}\text{Fe}_x$ carbonate hydroxide hydrate 1D nanowires and coordinated with 2MIM ligand, followed by the pyrolysis in N_2 atmosphere as illustrated in **Fig. 17 h**^[93], which can also be witnessed from morphological illustration in **Fig. 17 i**. Moreover, it 1D/2D hierarchical structure retained even after pyrolysis. The lattice fringe of $\text{Co}_{0.68}\text{Fe}_{0.32}\text{O@NC}$ displays interlayer spacing of 2.50 Å corresponding to the plane of (111) and (311) of CoO and Fe_3O_4 respectively. Also, layer spacing of 2.10 Å corresponding to plane of (200) and (400) plane of CoO or the Fe_3O_4 respectively. Interestingly, the voltage gap of resultant catalyst was 0.97 V, which reduced to 0.89 V after 450 charge-discharge cycles (**Fig. 17 j**). Moreover, cycling

This article is protected by copyright. All rights reserved.

durability of $\text{Co}_{0.68}\text{Fe}_{0.32}\text{O@NC}$ was higher in contrast to the Pt/C catalyst. $\text{Co}_{0.68}\text{Fe}_{0.32}\text{O@NC}$ loaded catalyst also demonstrated higher specific capacity ($692 \text{ mAh g}_{\text{Zn}}^{-1}$ @ 5 mA cm^{-2}) and energy density (773 Wh kg^{-1}).

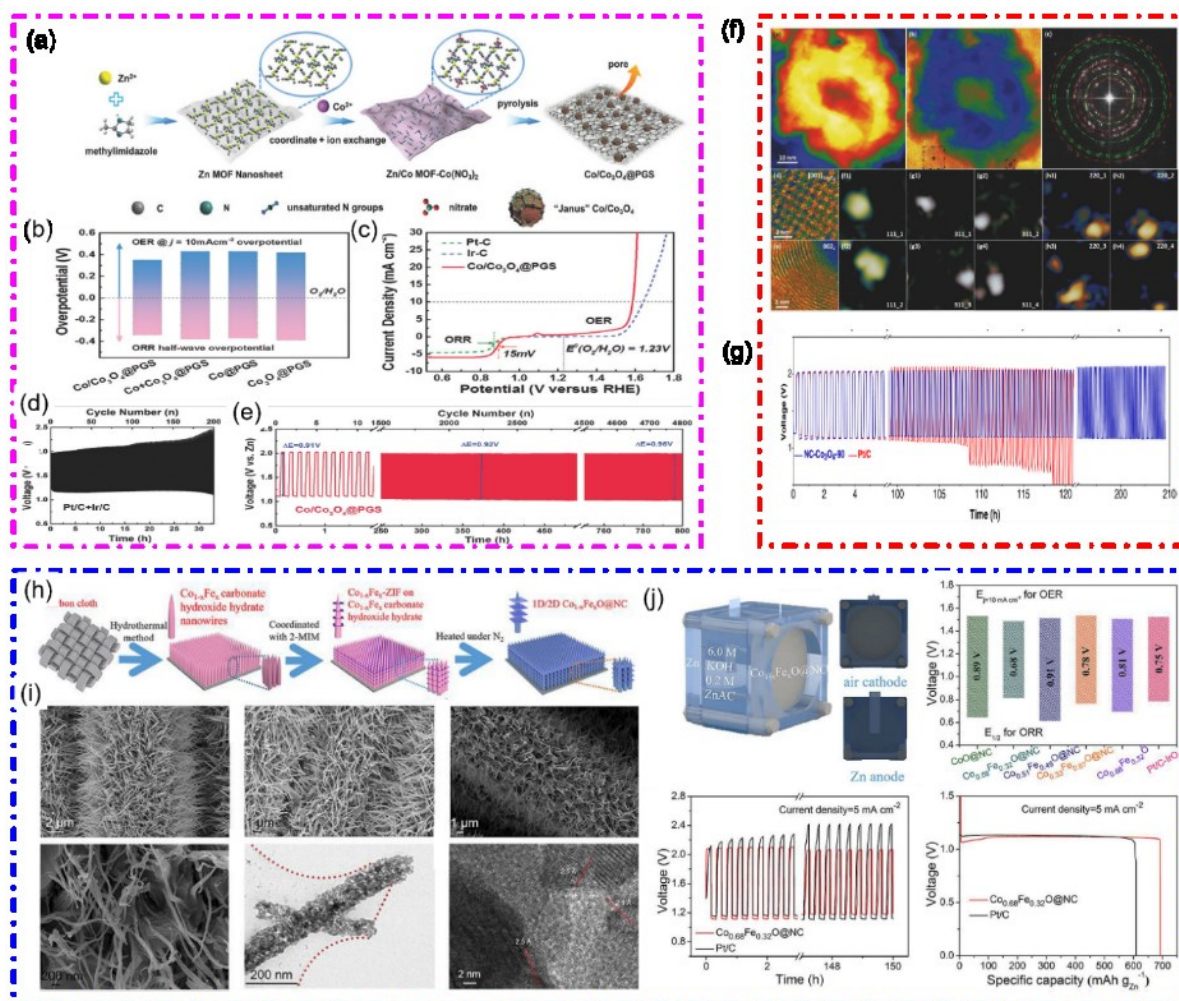


Fig. 17 (a) Representation of synthesis process used to prepare interpenetrating Co_3O_4 and Co nanoparticles implanted in porous graphitized shells ($\text{Co}/\text{Co}_3\text{O}_4\text{@PGS}$). In “Janus” nanoparticles, the green part represents Co_3O_4 and metallic Co represents red part, (b) Potential differences between the $E_{\text{half-wave}}$ for ORR and $E_{j=10}$ for OER for $\text{Co}/\text{Co}_3\text{O}_4\text{@PGS}$ and other products, (c) The entire LSV curves for bifunctional activities within the ORR and OER potential window of $\text{Co}/\text{Co}_3\text{O}_4\text{@PGS}$, Pt/C, and Ir/C at 1600 rpm (d) Zn-air battery performance for the coupled noble-metal Pt/C+Ir/C and (e) $\text{Co}/\text{Co}_3\text{O}_4\text{@PGS}$ catalysts at a current density of 10 mA cm^{-2} . Reproduce with permission.^[207] Copyright 2018, WILEY- VCH. (f) Morphology and structure of the NC- Co_3O_4 - 90 nanoarrays. Colored STEM HAADF/ABF images, FFT image, the reflections from Co_3O_4 and C , lattice image featuring the cubic lattice of Co_3O_4 , Colored IFFT images from different 111/311/220 reflections, (g) Cyclic stability of NC- Co_3O_4 - 90 in rechargeable ZABs. Reproduced with permission.^[94] Copyright 2017, WILEY- VCH. (h) Schematic illustration of $\text{Co}_{0.68}\text{Fe}_{0.32}\text{O@NC}$, (i) SEM of $\text{Co}_{0.68}\text{Fe}_{0.32}$ carbonate hydroxide hydrate, $\text{Co}_{0.68}\text{Fe}_{0.32}\text{-ZIF}$ on $\text{Co}_{0.68}\text{Fe}_{0.32}$ carbonate hydroxide hydrate and $\text{Co}_{0.68}\text{Fe}_{0.32}\text{O@NC}$; TEM of $\text{Co}_{0.68}\text{Fe}_{0.32}\text{O@NC}$ and the lattice fringe of $\text{Co}_{0.68}\text{Fe}_{0.32}\text{O@NC}$ (j) Schematic of the aqueous ZABs; bar plots of the voltage gap between $E_{j=10}$ and $E_{1/2}$; 150 h cycling performance of the fabricated aqueous ZABs at 5 mA cm^{-2} ; specific capacity of ZABs normalized to the mass of consumed zinc at 5 mA cm^{-2} . Reproduced with permission.^[93] Copyright 2020, Elsevier Ltd.

3.1.2.6. CoN4 /carbon composite

In contrast to the metal oxides, transition metal nitrides such as Co₄N^[209] Ni₃N^[210] and Ni₃FeN^[211], are considered to have higher electrical conductivity and chemical stability, leading to efficient charge transfer during OER and ORR activities.^[212] The rise in electrical conductivity resulted from contraction of d bands close to Fermi levels.^[213] Moreover, DFT calculations have unveiled that ORR activity of transition metal nitrides is comparable to that of Pt for oxygen adsorption and O=O bond cleavage^[214]. Moreover, N atoms in metal hosts can modulate the electronic structure of d band, highlighting the electron-donating feature of metal nitrides (e.g. Co₄N).^[215] Actually, the doping of N into the crystal lattice of transition metals imposed strong bond with metal atoms, endowing metal-like features and eventually promoted the electrical conductivities and stabilities.^[216] Again, ZIFs are promising precursor for the synthesis of Co₄N and it develops a synergistic effect with 3D porous structures of carbon, leading to the favorable electroactivity for Zn-air batteries. For instance, Ge et al. synthesized Co₄N nanoparticles embedded in N-doped carbon via successive pyrolysis of ZIF-67 at 900 °C (N₂ atmosphere) and at 350 °C (NH₃ atmosphere) by using the precursors as illustrated in **Fig. 18 (a)**.^[110] Co₄N nanoparticles promoted the electronic conductivity and also contributed in reducing the adsorption free energy of intermediates during OER/ORR activities for the rate determining step (RDS). Furthermore, DFT calculations underscored that nitrogen doping in Co lattice assisted in enhancing the electronic conductivity, suppressing the overpotential and eventually accelerating OER/ORR reaction kinetics **Fig. 18 b**. The uniform dispersion of Co₄N nanoparticles in the carbon box inhibited the agglomeration and led to the high power density (74.3 mW cm⁻²) and outstandingly sustained charging /discharging performance of Zn-air batteries (750 h @ 5 mA cm⁻²) as illustrated in **Fig. 18 c**.

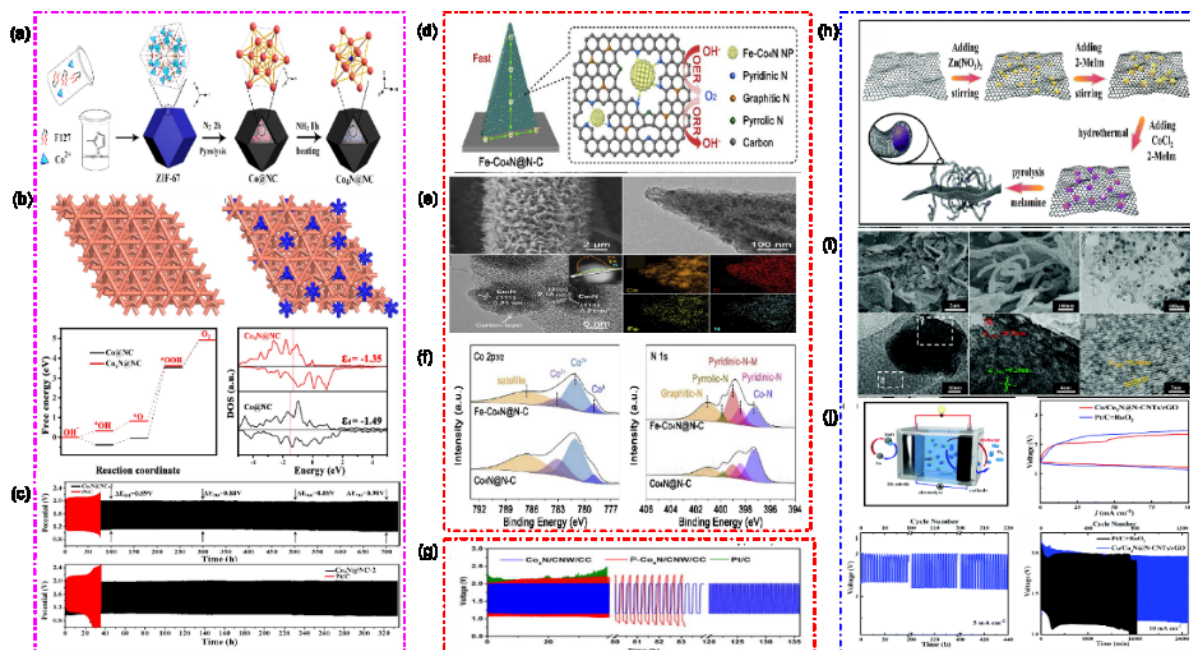


Fig. 18 (a) Illustration of the synthesis procedure of $\text{Co}_4\text{N}@NC$ (b) Free energy diagrams for OER on Co and Co_4N surfaces and DOS of surface Co d orbitals of Co and Co_4N , (c) Cycling stability of $\text{Co}_4\text{N}@NC-2$ and Pt/C at discharge/charge current densities of 5.0 mA cm^{-2} and 10.0 mA cm^{-2} . Reproduced with permission.^[110] Copyright 2020, Elsevier Ltd. (d) Schematic illustration of the Fe- $\text{Co}_4\text{N}@N-C$ nanosheet grown on carbon cloth for dual-functional oxygen reaction; (e) SEM; high-magnification TEM; high-resolution TEM images and corresponding TEM-EDS mapping of the Fe- $\text{Co}_4\text{N}@N-C$ electrocatalyst; (f) High-resolution XPS spectra of N 1s and Co $2p_{3/2}$ of the $\text{Co}_4\text{N}@N-C$ and the Fe- $\text{Co}_4\text{N}@N-C$ electrocatalysts. Reproduced with permission.^[111] Copyright 2019, Elsevier Ltd. (g) Cycling stability at 10 mA cm^{-2} of rechargeable Zn-air batteries with the $\text{Co}_4\text{N}/CNW/CC$ electrode P- $\text{Co}_4\text{N}/CNW/CC$ and Pt/C catalyst on carbon cloth, respectively. Reproduced with permission.^[113] Copyright 2016, American Chemical Society. (h) Synthesis scheme for Co/ $\text{Co}_4\text{N}@N-CNTs/rGO$; (i) SEM images and TEM images of Co/ $\text{Co}_4\text{N}@N-CNTs/rGO$ at various magnifications; (j) Representation of the rechargeable Zn-air battery; Charge/discharge curves of the ZABs with Co/ $\text{Co}_4\text{N}@N-CNTs/rGO$ and Pt/C + RuO_2 cathodes; galvanostatic charge/discharge curves of the Co/ $\text{Co}_4\text{N}@N-CNTs/rGO$ -based ZABs at 5 mA cm^{-2} of current density with a fixed time of 2 h per cycle; cycling stability of the Co/ $\text{Co}_4\text{N}@N-CNTs/rGO$ and Pt/C + RuO_2 -based ZABs at 10 mA cm^{-2} with 20 min per cycle. Reproduced with permission.^[112] Copyright 2019, Royal Society of Chemistry.

Recently, Xu et al. fabricated Fe- $\text{Co}_4\text{N}@N-C$ nanosheets array by in situ growing Co-MOF on carbon cloth using $\text{Co}(\text{NO}_3)_2$ and 2-MIM, followed by the immersion in aqueous solution of $\text{K}_3[\text{Fe}(\text{CN})_6]$ at room temperature (Fig. 18 d).^[111] Morphological analysis depicts that structure of nanosheets array and tipping point of a single nanosheet (Fig. 18 e). As per HRTEM, the graphitization of carbon layers was a bit lower. From the deconvolution of XPS spectra, it can be visualized that the higher oxidation states associated to Co species (Co^{3+} and Co^{2+}) imply the transfer of electron from Co to N atoms (Fig. 18 f). The larger peak area ratio of Co^{3+} [$\text{Co}^{3+}/(\text{Co}^0 + \text{Co}^{2+} + \text{Co}^{3+})$] of Fe- $\text{Co}_4\text{N}@N-C$ (71.3%) of) in contrast with $\text{Co}_4\text{N}@N-C$ of (65.3%) suggesting the upgraded OER performance of $\text{Co}_4\text{N}@N-C$ because Co^{3+} sites are vital for the swift formation of $^*\text{OOH}$, desired key OER intermediates.^[46b, 217] Also, high resolution XPS spectra of N1s represent Co-N bond in Co_4N .

Additional peaks of Pyridinic-N and Pyridinic-N-M species, which actually stemmed from the coordination between metal centres (Fe and Co) and Pyridinic-N, recognized as highly ORR active sites.^[218] The obtained Fe-Co₄N@N-C electrocatalyst demonstrated excellent bi-functional ORR/OER activity and stability. Similarly, Meng et al. fabricated Co₄N and Co nanoparticles encased in N-doped carbon via the carbonization of ZIF-67 string wrapped on the network of polypyrrole nanofibers.^[113] The formation of Co₄N nanoparticles in the N-doped carbon was promoted by the NH₃ released from PPy. Consequently, Co₄N in the electrocatalyst provided high OER activity while N-doped C contributed in achieving good ORR activity, leading to good performance in Zn-air batteries (135h) (**Fig. 18 g**).

Despite a great deal of benefits, pyrolysis of ZIFs has been shown to undergo aggregation of Co and Co₄N particles and demonstrate low surface, which in turn reduces the transportation of reactants and products. As a result, supporting MOFs on conducting carbon like reduced graphene oxide (rGO) found as an effective strategy wherein serve as efficient conductive network with high surface area and MOFs provide the major active sites.^[219] Therefore, Qi et al. developed modified graphene oxide with ZIF-8@ZIF-67 precursor to encapsulate Co/Co₄N nanoparticles into N-doped CNTs and rGO (Co/Co₄N@N-CNTs/rGO) (**Fig. 18 h**).^[112] After the pyrolysis, Co/Co₄N@N-CNTs/rGO exhibited a thin film architecture and several CNTs were uniformly distributed over the rGO surface (**Fig. 18 i**). The encapsulation of Co/Co₄N in CNTs efficiently suppressed the agglomeration of Co/Co₄N particles and developed an intimate contact between the co species and N-CNTs in Co/Co₄N@N-CNTs/rGO. Furthermore, the presence of rGO matrix and Zn evaporation followed by the carbonization considerably led to the rise in surface area of Co/Co₄N@N-CNTs/rGO, which obviously facilitated the exposure of sufficient active sites and excellent ion/electron transport. Consequently, the resultant Co/Co₄N@N-CNTs/rGO exhibited lower discharge/charge overpotentials in comparison with the Pt/C + RuO₂ electrode and charging/discharging cyclic stability with a reasonable potential gap (**Fig. 18 j**). Besides, Co/Co₄N@N-CNTs/rGO exhibited good electrochemical performance and superior mechanical strength under several bending conditions in flexible Zn-air batteries.

3.2 Morphology control

3.2.1 Nanofibers from electrospinning

Generally, the materials derived from virgin ZIFs lack in electrical conductivity and possess poorly exposed active sites as a result of collapse of porous structure, leading to inadequate catalytic performance. To exploit the plenty of catalytic sites in ZIFs-derived carbon, growth of ZIFs onto a polymer substrate could be an efficient strategy to improve the structures of ZIFs-based materials.^[116] For instance, several studies have implemented the electrospinning of ZIFs to be rooted

into polymer fiber to get the advantage of porous, heteroatom- doped carbon nanofiber, exhibited wonderful catalytic performance.^[220] Electrospinning is known as a facile and economical strategy for the synthesis of uniform fibers, possessing high surface area, large length/diameter ratio and superb flexibility.^[221] Upon carbonization of electrospun fibers, the metal efficiently accelerate the fiber graphitization embedded with metal, which contribute in increasing the electrical conductivity, and thus electrochemical performance and stability of the fibers.^[222] Recently, Yao et al. designed polyacrylonitrile and ZIFs derived 3D callistemon-like nanostructure, synthesized by 2-MIM, ZIF-67, ZIF-8, and polyacrylonitrile (PAN) through electrospinning, subsequent to the pyrolysis.^[114] The obtained 3D callistemon-like structure wherein Co nanoparticles were encapsulated within N-CNT apex, possessed multiple active sites with enhanced electrical conductivity and got around the particle aggregation. The catalyst demonstrated excellent tri-functional performance as well as for ZABs.

Similarly, Li et al. utilized electrospun polyacrylonitrile (PAN) fibers for in-situ growth of ZIF-67 microcrystals onto it. Following the pyrolysis, PAN@ZIF-67 precursor yield PAN-derived carbon fibers (C-PAN) @Co/N-C (**Fig. 19 a**).^[115] **Fig. 19 b** features TEM image of carbonized ZIF-67 particles on carbonized PAN together with multiple Co nanoparticles embedded inside the carbonized ZIF-67 corresponding to the lattice fringe spacing of 0.207 nm. The resultant C-PAN) @Co/N-C catalyst offered multiple active sites together with significant flexibility and conductivity endowed by the synergistic coupling.

Guo et al. designed pod-like Co/CoO_x-N-C nanoparticles, obtained after electrospinning of ZIF-67@PAN fibers, followed by the pyrolysis at 800 °C. As it can be observed from SEM morphology that nanofibers were successfully produced (**Fig. 19 f**).^[222b] This one-dimensional, porous pod-like structure endowed the electrocatalysts with excellent features such as high graphitization degree and large N content. The crystal size of ZIF-67 has a crucial role in deciding the morphology and ultimate electrochemical performance. The unique structure of Co/CoO_x-N-C nanoparticles contributed in quick transmission of O₂ and H₂O, which eventually led to the tremendous ORR performance. However, this strategy led to the reduction in surface area and active sites as an outcome of ZIFs encapsulation with polymers.

Therefore, to achieve the high porosity of ZIFs and maximal exposure of active sites, Zhao et al. designed a ZIFs/polyacrylonitrile core/shell structure after the in situ ZIFs growth over the surface of polyacrylonitrile (PAN) fiber (PAN@ZIFs).^[116] Subsequent to the carbonization, this core/shell structure led to CNF@Zn/CoNC, an effective bifunctional electrocatalyst with largely exposed active sites, continuous conductive network and heteroatom- doped carbon nanofiber. The synergistic effect of CNF@Zn/CoNC core-shell structures contributed to an outstanding ORR/OER bifunctional catalytic performance . The evolution of morphology is illustrated in **Fig. 19 c**, wherein two major factors influencing the 1D core-shell structure are elaborated: The sequence of addition of ligands; the

This article is protected by copyright. All rights reserved.

addition of PVP. It was found that by controllable sequence of addition as well as introduction of PVP, an architecture consisting of core-shell PAN@ZIFs fiber coupled with numerous components may be designed.

N- doped iron carbide nanoparticles (e. g. Fe- N-C) are considered as promising electrocatalysts because of their tolerance towards alkaline electrolyte and it offers ample electroactive sites.^[218a, 223] Li et al. developed Fe³C/Fe nanoparticles supported on the N-doped porous carbon nanofibers, through electrospinning of Polyacrylonitrile/ZIF- 8 nanofibers, subsequent to the coating of tannic acid and coordination with Fe³⁺, followed by the calcination treatment, which can be featured in **Fig. 19 d**.^[117] Morphological studies revealed that the as- prepared nanofibers of PAN/ZIF- 8 were mutually well-connected and metallic species evenly anchored on the Fe/N- HCNFs surface. The obtained catalyst presented outstanding ORR and OER performance and higher power density accompanied by excellent long- term stability for 260 cycles (**Fig. 19 e**).

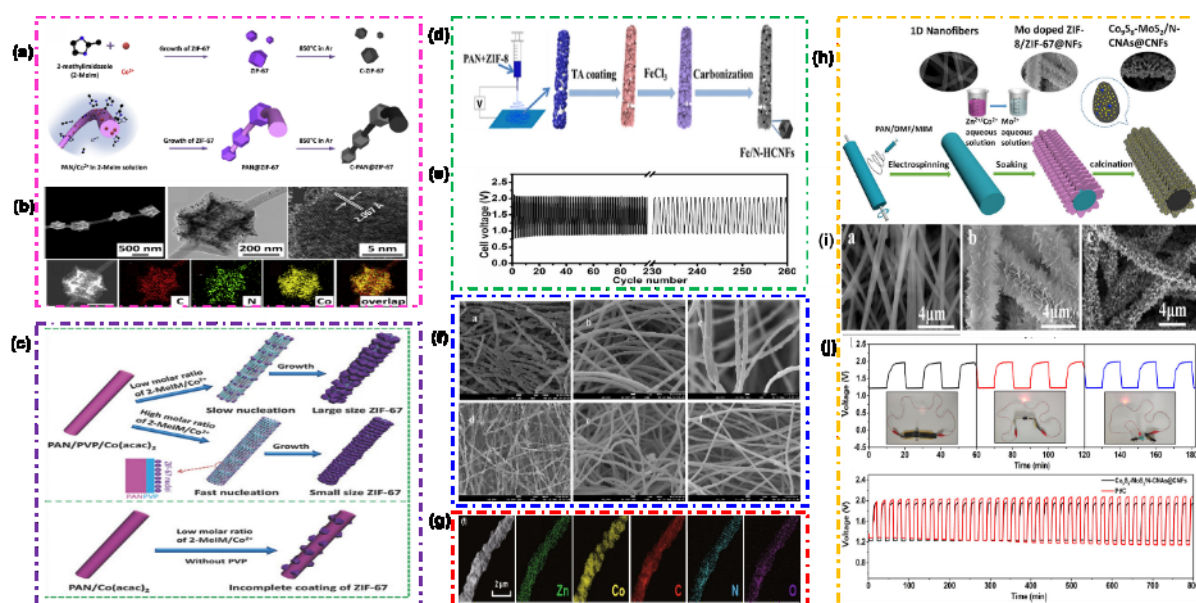


Fig. 19 (a) Schematic illustration of ZIF-67 microcrystals growth in solution, or on a PAN fiber as PAN@ZIF-67 of “gems-on-string” structure, and their respective pyrolyzed products, C-ZIF-67 and C-PAN@ZIF-67. (b) A zoom-in FESEM image of a C-PAN@ZIF-67 fiber. A TEM image of C-PAN@ZIF-67. A HRTEM image of a Co NP in C-PAN@ZIF-67, An HAADF-STEM image and the corresponding STEM-EDS of C-PAN@ZIF-67, showing the distribution of C, N and Co. Reproduced with permission.^[115] Copyright 2019, Elsevier (c) Schematic illustration of morphology evolution in PAN@ZIF- 67 fiber. Reproduced with permission. Reproduced with permission.^[116] Copyright 2018, WILEY- VCH (d) Schematic illustration of synthetic process for Fe/N- HCNFs (e) Galvanostatic pulse cycling at 20 mA cm⁻² for 260 cycles using Fe/N- HCNFs as air electrode. Reproduced with permission. ^[117] Copyright 2019, Wiley- VCH. (f) SEM images of ZIF-67-l @ PAN, ZIF-67-m@PAN, and ZIF-67-s@PAN,

This article is protected by copyright. All rights reserved.

respectively and TEM images. Reproduced with permission.^[222b] Copyright 2018, Elsevier Ltd. (g) STEM mappings of Zn/Co-ZIFs/PAN nanofiber. Reproduced with permission.^[224] Copyright 2019, Springer Nature. (h) Schematic Illustration of the Synthesis Scheme of Co₉S₈-MoS₂/N-CNAs@CNFs; (i) SEM images of PMNFs, polymer Co/Mo@PMNFs, and Co₉S₈-MoS₂/N-CNAs@CNFs; (j) Cycling performance of the battery with the Co₉S₈-MoS₂/N-CNAs@CNFs cathode at different bending angles and Galvanostatic discharge–charge performance of flexible ZBAs. Reproduced with permission.^[119] Copyright 2020, American Chemical Society.

As Co₂P nanoparticles are reported to serve as active species for both OER as well as ORR, whereas Fe₅C₂ nanoparticles are recognized to act as active sites for ORR.^[225] Therefore, Di et al. decorated Co₂P and Fe₅C₂ nanoparticles in the form of core–shell porous carbon nanofibers through in-situ growth of ZIF-67 and electrospinning.^[118] Catalytic active sites of Fe₅C₂ and Co₂P were secured from detachment by graphite carbon. The resultant catalyst demonstrated reasonable OER and excellent ORR activities, which may be credited to the swift diffusion of O₂ molecules and electrolytes diffusion, high conductivity, porosity and easily accessible multiple active sites. Another study also utilized bimetal–heteroatom-doped carbon nanofibers by the pyrolysis of electrospun Zn/Co-ZIFs/PAN nanofibers at 800 °C.^[224] From STEM elemental mapping, it can be observed that ZIF-67 crystals were uniformly distributed and embedded in the PAN fibers (**Fig. 19 g**). The obtained electrocatalyst displayed a high power density as well as high specific capacity. However, the cyclic life of Zn/Co-ZIFs/PAN was not so impressive.

Another interesting study regarding the development of nanofibers in which Zhang et al. fabricated Mo-doped ZIF-8/ZIF-67 grown on electrospun nano fibres. Upon vulcanization at 800°C in Ar/H₂ atmosphere gives Co₉S₈ and MoS₂ nanocrystals carbon flakes supported on carbon nano fibres as the final product (**Fig. 19 h**).^[119] From the morphological analysis (**Fig. 19 i**), a smooth and regular tubular patterns can be visualized. Nano flakes arrays were vertically grown on the tubes after soaking in the reaction mixture. Following the vulcanization, morphological features were significantly retained, though the nano flakes were turned smaller and rougher. Eventually, the composite material exhibited promising activity towards both liquid and all-solid-state Zinc-air batteries, presented brilliant performance even superior to the Pt-based catalysts. It is worth mention that two flexible ZABs connected in series were able to power LED at various bending angles and produced a very stable charge–discharge cycle over a period of 800 min at 5 mA cm⁻² (40 cycles) as depicted in **Fig. 19 j**.

3.2.2 Core/shell structured composite

The core/shell structure is useful strategy to exploit the unique properties of two electrocatalysts in a single one. The core- shell M–N–C material based on ZIFs demonstrated excellent performance for ZABs and superior ORR activity in comparison with materials derived from a single ZIF, such as ZIF- 67 or ZIF- 8 precursor.^[226] For instance, upon carbonization, ZIF-67 yield highly graphitic

carbon (GC) whereas ZIF-8 produces nitrogen-doped carbon (NC). ZIF-67 largely comprised of graphitic carbon, which is known for high stability and good conductivity^[59]. On the other hand, ZIF-8 consist of amorphous carbon, which is less stable and a poor conductor, while it has relatively high surface area and uniform and high N doping.^[79b] Therefore, in order to combine the benefits of these two carbon materials, Wang et al. designed a core/shell composite composed of nitrogen-doped carbon core, whereas graphitic carbon shell (NC@GC) via hydrothermal method using seed-mediated growth strategy employing ZIF- 8@ZIF- 67.^[19] The obtained NC@GC catalyst provided an opportunity to present the unique properties of ZIF- 8 and ZIF- 67 together in a single catalyst, which integrated graphitized Co–N–C shells and highly N- doped porous carbon cores.

Morphological studies of NC@GC reveal that nanotubes and graphitic carbon is likely the outcome of calcination in the presence of cobalt species.^[227] Furthermore, graphitization of amorphous carbon on metal/metal oxide may result in the emergence of bumpy surface, which eventually promoted the electrical conductivity and thus, the catalytic performance.^[79b, 228] NC@GC composite demonstrated far better OER performance for Zn–air batteries and ORR in particular, in comparison with individual ZIF- 67 or ZIF- 8. The enhanced electrochemical properties may be attributed to the N/Co-doping effect, low charge transfer resistance, high surface area and synergistic interaction between GC and NC. Zhang et al. developed a bimetallic Zn, Co- ZIFs and single walled carbon nanohorns electrocatalyst for ORR using different Zn : Co molar ratios and found that increase in Zn proportion leads to the rise in surface area of MOFs derived Co–N–C material.^[229] Nanohorns contributed to create 3D conductive network, which eventually led to the improvement in the performance even comparable to the 20 % Pt/C catalyst and presented outstanding stability and half-cell test and in alkaline solution. They also established a correlation between pore structures and peak power densities.

Typically, ZIFs may also suffer from the deeply buried and unexposed active sites. This issue may be addressed by in situ growing the carbon nanotubes with transition metals at the apex, possessing the core-shell structure corresponding to transition metal embedded in nitrogen doped carbon.^[230] Therefore, Wang and co-workers developed actiniae-like structure with 3D carbon nanotube assembly via carbonizing the mixture of melamine and ZIF-67 as shown in **Fig. 20 b**.^[156b] They obtained the core-shell structure consisting of N-doped carbon nanotubes and Co nanoparticles located at the apex, (Co@N-doped carbon) behaves like a synapse structure (**Fig.20 c**). This configuration is capable of exposing sufficient Co active sites to the electrolyte, while protecting them from corrosion. The resultant catalyst exhibited a small potential gap of 0.68 V and high round-trip efficiency (65.8%) with a performance decay of 0.14V after 40h (**Fig.20 a**). The remarkable rise in rate capability was credited to the formation of a network consisting of interconnected nanotubes network which assisted

in swift electron transport and 1 D accessible electrochemical surface area (magnified image of **Fig. 20 b**).

Wang et al. proposed a composite material based on bimetallic zeolitic imidazolate frameworks (BMZIFs, ZIF-67 and ZIF-8) as a core and Fe/N/C framework as a shell (Fe/N/C@BMZIF) as shown in **Fig. 20 f**.^[167] The N-doped carbon ligaments at the interface between evenly dispersed BMZIFs nanocrystals and Fe/N/C framework expedited the electron cloud migration, promoting the oxygen electrocatalysis. It was interesting to notice that BMZIF and Fe/N/C individually demonstrated mediocre oxygen electro catalytic activity, whereas Fe/N/C@BMZIF composite presented remarkable ORR and OER bi-functional activities even better than Pt/C or IrO₂/C benchmark catalysts for Zn–air batteries, which may be ascribed to the coupling effect between BMZIF and Fe/N/C. In addition, Fe/N/C@BMZIF composite also showed high peak power density of 235 mW cm⁻² for primary batteries. Recently, sulfidation of ZIF-67 polyhedrons led to the excellent OER active catalyst. For instance, Guo et al. developed ZIF-67-derived Co₃S₄@MoS₂ material, which served as bifunctional (OER/ORR) activity.^[231] Following the pyrolysis, these metallic and non-metallic elements can be evenly distributed in the carbon framework, which can significantly promote the surface polarity and electronic conductivity.^[232] Although, these electrocatalysts exhibit catalytic performance comparable to the precious metals based electrocatalysts, however, OER, ORR and HER activities of these electrocatalysts are still limited because of inferior intrinsic activities and inadequate number of active sites.^[232a] Therefore, the fabrication of three-dimensional structures can inhibit the nanomaterials aggregation, leading to higher surface area and more exposure of active sites.^[233]

By virtue of ultrahigh surface area and flexibility, ZIFs give an opportunity to design multifunctional materials. Amiin et al. designed Co–N codoped carbon nanorod array after growing on Ti–metal substrate using ZIF-8 via hydrothermal synthesis strategy.^[46b] As a result, the obtained catalysts had superior OER and ORR activity to that of benchmark IrO₂ and Pt/C catalysts. The origin of activity was deciphered using the DFT studies and post reduction XPS. Furthermore, these electrocatalysts presented low overpotential and excellent energy density in solid state secondary batteries and primary Zn-air batteries. XPS analysis revealed the Co species (**Fig. 20 d**). The optimal oxygen electrode exhibited the highest content of pyridinic N (38.4%), followed by graphitic N (35.3%). The pyridinic N is considered to increase the surface wettability^[234] and onset potential^[53, 235] whereas graphitic N is known to enhance the diffusion-limited properties.^[236] As per Density functional theory (**Fig. 20 e**), the analysis of the highest occupied molecular orbitals (HOMOs) revealed that the coupling of Co and pyridinic N causes higher HOMO energy (–4.647 eV) in contrast with Co and pyrrolic N (–4.765 eV), implying that the coupling of Co and pyridinic N is more conducive to ORR, which is also in agreement with previous reports.^[237] Furthermore, coupling between Co and pyridinic N demonstrated higher density of states, crossing the Fermi level, suggesting higher reactivity as well as larger

electron mobility. Thus, these results reinforced that the coupling of Co and pyri- N species is liable for the enhanced ORR performance.

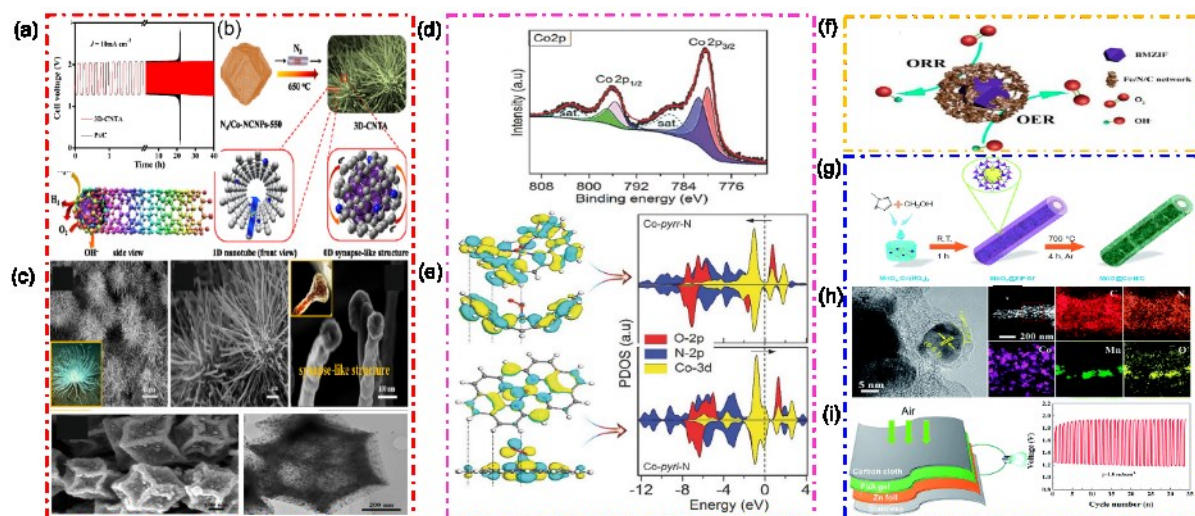


Fig. 20 (a) Galvanostatic charging/discharging cycling performance at current density of 10 mA cm^{-2} of ZABs with the 3D-CNTA or Pt/C as catalysts, respectively. (b) Demonstration of fabrication process of 3D-CNTA. (c) FE-SEM images of 3D-CNTA at different magnifications (the insets are the digital photographs of actiniae and synapse, respectively), TEM images of 3D-CNTA at different magnifications, FE-SEM and TEM images of Co-NCNPs. Reproduced with permission.^[156b] Copyright 2017, Elsevier Ltd. (d) XPS spectra of Co-N_x/C NRA, featuring XPS spectra of C1s and Co 2p. (e) DFT computations of Co-N_x/C NRA catalyst. HOMO spatial distributions of α and β electrons, the isovalue is 0.022 au. Atoms are C- gray, O- red, N- deep blue, Co- light blue and H- white, Projected density of states for model catalysts with pyri- N (down) and pyr- N (top) configurations. Reproduced with permission.^[46b] Copyright 2017, WILEY- VCH. (f) Schematic reaction mechanism of the OER and ORR processes catalyzed by Fe/N/C@BMZIF. FESEM. Reproduced with permission.^[107] Copyright 2017, American Chemical Society. (g) Schematic illustration of the formation of MnO@Co-N/C nanowires (h) Discharge-charge cycling curves at 5 mA cm^{-2} and at 10 mA cm^{-2} of rechargeable Zn-air batteries (i) Schematic structure of a solid state ZABs and discharge-charge cycling curves at a current density of 1 mA cm^{-2} . Reproduced with permission.^[108] Copyright 2018, Royal Society of Chemistry.

Chen et al. rationally designed MnO_2 @ZIF-67, a core/shell precursors to prepare MnO@Co-N/C nanomaterials.^[108] Initially, they synthesized $\alpha\text{-MnO}_2$ nanowires using a facile hydrothermal method (Fig. 20 g). Subsequently, as prepared brown precipitates of $\alpha\text{-MnO}_2$ nanowires poured into the precursors of ZIF-67 to obtain MnO_2 @ZIF-67, followed by the pyrolysis at 700°C , which eventually ended up into highly porous MnO@Co-N/C nanoparticles. Morphological analysis (TEM) also confirmed that the generated nanoparticles were uniformly dispersed in the carbon network and a thin layer of Co-N/C enveloped the hollow nanowire, whereas the lattice fringes attributed to (003) plane of Co (Fig. 20 h). The excellent performances endowed with the synergistic effect arising from the porous Co-N/C and MnO in one-dimensional nanowires, leading to the persistent and easily accessible electrolytes diffusion to the active sites. Furthermore, one-dimensional, hollow MnO_2 nanowires served as template to direct the growth of ZIF-67 polyhedral as a driving force for crystallization. ZIF-67 derived Co-N/C layers

continuously decorated around MnO and provided plentiful Co–N_x active sites, facilitated electron conduction while reducing the aggregation of carbon. Consequently, MnO@Co–N/C nanowires outperformed the benchmark Pt/C catalyst for liquid Zn–air batteries for 600 h @ 5 mA cm⁻² and a distinctive performance for solid-state Zn–air batteries for 35 cycles (**Fig. 20 i**).

Despite using hard templates such as 1D MnO and Te nanowire, 2D graphene nanosheet and 3D melamine sponge as a structure- directing source, the growth of ZIFs was not homogeneous which is a great challenge.^[238] To meet this challenge, Song et al. successfully achieved the homogeneous growth of ZIF- 67 and Zn/Co- ZIF on ZnO.^[109] Furthermore, they also interpreted the ZIF growth mechanism and flexible dimensional control of ZIF growth on ZnO. The development of ZIF- 8 seed on ZnO template was emphasized as the critical step, leading to the homogeneous growth of ZIF materials such as Zn/Co- ZIF, Zn/Fe- ZIF, and ZIF- 7) possessing 1D, 2D, and 3D dimensions. Subsequently, 1D and 2D ZnO@ZIF precursors were transformed into carbon nanoplate and CNTs, which were attached with Fe single atom, ended up into Fe/CNP, which may serve as ORR catalyst. Subsequently, they deposited NiFe- LDH thin layers, known as OER active catalyst, over the surface of Fe/CNP (NiFe- LDH@Fe/CNP) through modified hydrothermal method. The resultant homogeneous core-shell structure displayed a potential gap of only 0.727 V between ORR (E_{1/2}) and OER (E_{j=10}), signifying the excellent bifunctional activity. When the catalyst was loaded as air electrode for Zn–air batteries, delivered a steady discharging/charging voltages for 300 cycles.

3.3 Hybridization

3.3.1 ZIF-based hybrids

As the air electrode for ZABs are bi-functional materials, therefore, the hybridization of two different materials possessing OER or ORR activities is considered as a promising strategy to furnish bi-functional activity. It was also found that in situ growth strategy of MOFs on different templates like layered double hydroxides, 1D ultrathin nanowire, perovskites and 2D graphene are substantially employed to suppress the electronic resistance as well as the loss of electron in the course of electronic transport through the carbon matrix.^[239] In addition to inter-particle resistance, the implication of aggregation of catalytic species may also be avoided by the in situ growth.^[240] Recently, Xie et al. synthesized numerous nanotube vertically grown onto the hollow microtube by the in situ growth of ZIF-67 on polydopamine coated polypropylene after a pyrolysis treatment at 800 °C (**Fig. 21 a**).^[124] They employed high mass loading to meet the requirement of high energy density and high power density for the latest electronic equipment. They obtained high specific

capacity of $781.7 \text{ mAhg}^{-1}_{\text{Zn}}$ and high power density of 160.6 mW cm^{-2} . However, when the zinc-air battery was assembled by applying a thick electrode of high mass loading of 3 mg cm^{-2} , the potential gap was a bit higher with a fluctuating OER/ORR activities, corresponding to 1.17V at a current density of 20 mA cm^{-2} and shorter cyclic life (**Fig. 21 b**). Similarly, Zhang et al. constructed a heterostructure of $\text{Co}_3\text{O}_4\text{-Co}$ and embedded it into ZIF-67 derived polyhedra of Co, N co-doped carbon matrix by in-situ NaBH_4 reduction.^[241] The obtained catalyst exhibited excellent bifunctional performance which may be credited to the charge redistribution of cobalt occurring in the CoN_x . DFT calculations disclosed that CoN_4 and CoO had developed electron coupling which induced a d-band negative shift in Co adsorption sites (CoN_4). Subsequently, it causes to drop the energy barrier significantly associated to the intermediates of O_2^* (ORR) and OH^* (OER), and eventually enhanced the overall catalytic performance. $\text{Co}_3\text{O}_4\text{-Co@NC}$ catalyst demonstrated a small potential gap of ΔE : 0.72V and maintained a stable charging-discharging stability $10 \text{ mA} \cdot \text{cm}^{-2}$ over a period of 200h.

In the same manner, Xiao developed a bimetallic ZnCo-ZIF supported on GO via in situ growth of a bimetallic ZIF GO nanosheets (**Fig. 21 e**).^[125] In contrast to bare ZnCo-ZIF, the designed ZnCo-ZIF@GO hybrid material exhibited excellent bi-functional (ORR and OER) activity in alkaline media. The bi-functional catalytic activity of ZnCo-ZIF@GO was credited to the intimate contact and synergy between GO and ZnCo-ZIF, leading to the multiple catalytically active sites hierarchical porous structure and the promoted ionic conductivity. Nevertheless, OER activity of the optimal catalyst was not so impressive (**Fig. 21 f**), led to the higher overpotential. Zhou developed in situ grown ZIF-67 nanocrystals onto polypyrrole (PPy) nanotubes (**Fig. 21 g**).^[126] PPy nanotubes served as a template, treated by anionic surfactant (Sodium laurylsulfonate) to render the surface of PPy nanotubes as electronegative. In this way, Co^{2+} were strongly anchored onto the surface, which endowed the catalyst with outstanding stability for 500h when applied as an air electrode for ZABs (**Fig. 21 h**).

As the perovskite oxides are recognized to demonstrate excellent OER activities, whereas ZIFs display remarkable ORR properties. Therefore, to furnish bi-functional properties in a single material, Shao group, recently developed a state-of-the-art porous, bi-functional nano-micro-composite, devised by the in situ growth of ZIF-67 polyhedrons onto the $\text{Ba}_{0.5}\text{Sr}_{0.5}\text{Co}_{0.8}\text{Fe}_{0.2}\text{O}_3$ (BSCF) perovskite oxide particles.^[67b] Following the carbonization, BSCF micro sized particles were encapsulated by the Co-N-C matrix ($\text{BSCF@Co-N}_x\text{-C}$) (**Fig. 21 c**). This unique architecture brought up several lucrative features, which translated into superior electrochemical performance: protecting BSCF particles against sintering; exposing plentiful active sites and bridging ZIF-67 derived $\text{Co-N}_x\text{-C}$ species and BSCF perovskites to facilitate the efficient electronic conductivity. BSCF also catalyzed the degree of graphitization of carbon in the course of pyrolysis. As a result, BSCF particles provided OER activity and $\text{Co-N}_x\text{-C}$ matrix delivered ORR activity, leading to the remarkable bi-functional activity and a

This article is protected by copyright. All rights reserved.

stable charge–discharge operation for 300 h (1800 cycles) for rechargeable Zn-air batteries (Fig. 21 d).

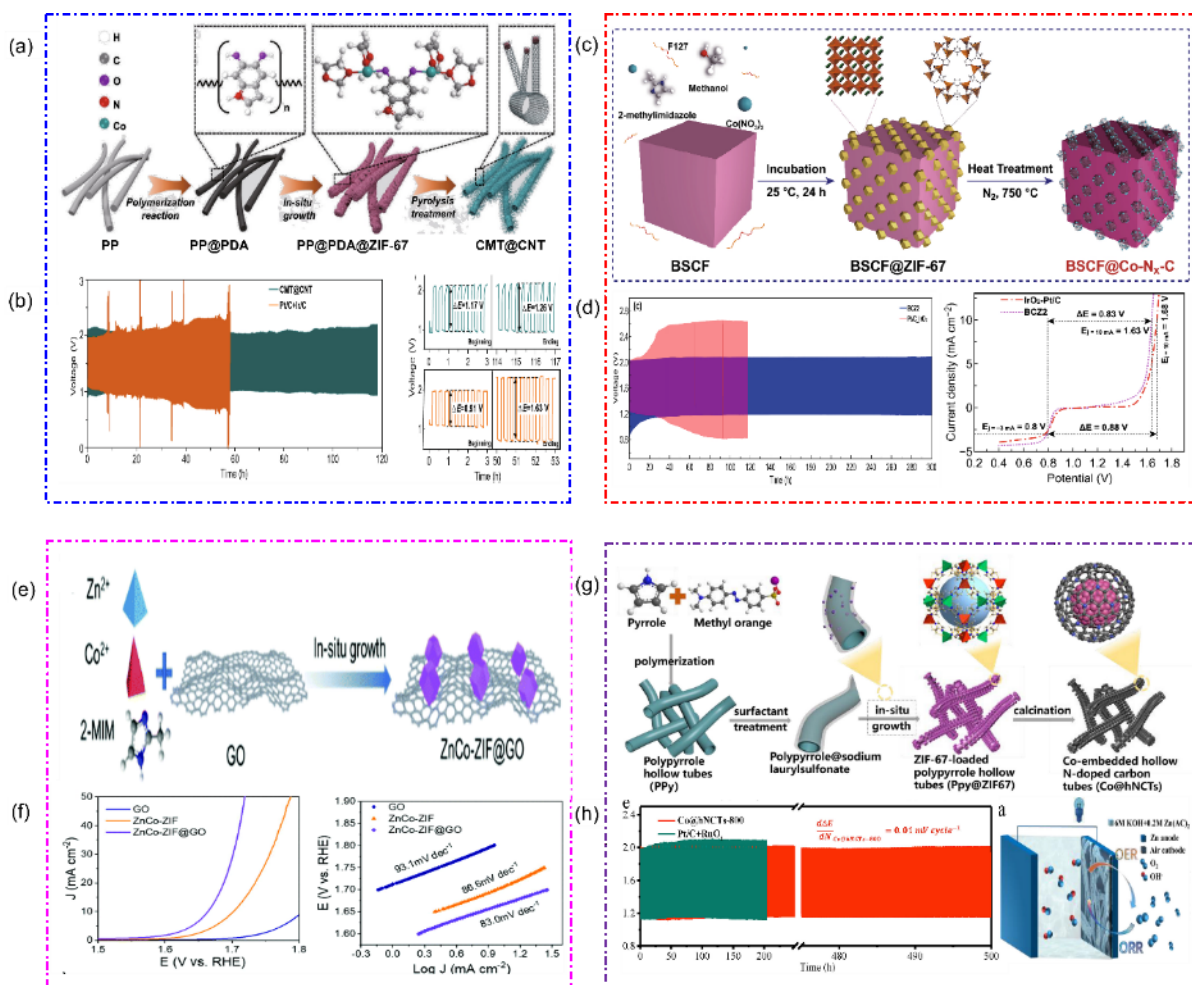


Fig. 21 (a) Schematic description for the preparation of CMT@CNT; (b) Discharge and charge curves of CMT@CNT and Pt/C + Ir/C-based ZABs Reproduced with permission.^[124] Copyright 2020, Springer Nature; (c) A schematic description of in situ growth of ZIF-67 crystals on BSCF surface and carbonization of prepared sample (d) Galvanostatic charge/discharge test based on BCZ2, Pt/C and IrO₂ mixture catalysts tested for Cyclic stability at 5 mA cm⁻² for 300 h and Overall polarization curves of BCZ2 and commercial Pt/C and IrO₂ in 0.1 M KOH. Reproduced with permission.^[67b] Copyright 2020, Springer Nature. (e) Schematic preparation of ZnCo-ZIF@GO; (f) ORR polarization curves in O₂-saturated 0.1 M KOH (rotation speed: 1600 rpm) and their corresponding Tafel plots. Reproduced with permission.^[125] Copyright 2020, Royal Society of Chemistry. (g) Schematic illustration for the synthesis of corn-like Co embedded in hollow N-doped carbon tubes (Co@hNCTs) catalysts; (h) Galvanostatic cycling performance of the Zn-air batteries with different catalysts at a current density of 5 mA cm⁻² (10 min per cycle) and schematic illustration of the Zn-air battery. Reproduced with permission.^[126] Copyright 2020, Elsevier Ltd.

In recent times, spinel-structured oxides have highlighted a great promise to develop electrocatalysts for water splitting after depositing onto the external surface of the carbon materials.^[242] Layered double hydroxide (NiFe, NiCo and CoFe-LDH) are considered as an outstanding precursor for designing spinel-structured oxides such as NiCo₂O₄, CoFe₂O₄, etc.^[243] Generally, spinel-structured

oxides had been found as OER active catalysts, however their ORR activity is inadequate.^[244] To obtain the excellent ORR activity, ZIF-67 derived Co, N-doped porous carbon network may be a favourable precursor. Therefore, Li et al. developed a hybrid NiCo₂O₄/Co,N-CNTs catalyst by depositing NiCo₂O₄ spinel onto the external surface of ZIF-67 (ZIF-67@NiCo₂O₄) as shown in **Fig. 22** (a).^[127] NiCo₂O₄ spinel provided excellent OER activity (**Fig. 22** c and e), whereas Co,N-CNTs derived from ZIF-67 contributed to superb ORR activity (**Fig. 22** d and f). As a result, NiCo₂O₄/Co,N-CNTs nanocages led to an excellent bifunctional activity with reversible oxygen electrode index (ΔE) corresponding to 0.707V (**Fig. 22** b and g) and battery performance for 45h (**Fig. 22** h). Besides, the spinel NiCo₂O₄ also provided the structural integrity to the nanocage frame.

Tan and co-workers also conducted an interesting study, they fabricated a bi-functional air electrode by the introduction of OER active Ni₃Fe nanoparticles into ORR active Co-N-C matrix as a support derived from Co, ZIF-8 through a microwave-assisted method.^[245] The resultant bi-functional electrocatalyst presented 1.54 V and 0.79 V at current densities of 10 mA cm⁻² (OER) and 3 mA cm⁻² (ORR) respectively, constituting ΔE : 0.75 V. When Ni₃Fe nanoparticles dispersed Co-N-C matrix was loaded as an air electrode, demonstrated a cyclic stability for a period of around 70h. Similarly, Li et al. designed a nanorod composite Co₆Mo₆C₂-Co@NC by employing Mopolydopamine@ZIF-67, wherein Co₆Mo₆C₂ is recognized as highly active sites for OER, whereas Co@NC serves as ORR active catalysts.^[246] Consequently, Co₆Mo₆C₂-Co@NC composite displayed remarkably a low overpotential of 268 mV at 10 mA cm⁻² (OER), and a high half-wave potential of 0.803 V (ORR). Moreover, it also demonstrated charge-discharge cycling stability as high as 300 h with no obvious rise in potential gap.

Ahn et al. designed a decoupled hybrid material wherein they introduced a unique hierarchical structure of Fe, N-doped porous carbon nanotubes via in situ growth of ZIF-8 on the surface of porous tellurium nanotube, followed by the incorporation of ultrathin Fe-ion-containing polydopamine ultrathin layer.^[128] The synergistic effects between the uniformly distributed FeN_x moieties and hierarchical dual-porous carbon network with a highly graphitic overlayer (FeN_xC) contributed to ORR catalytic activity. While OER activity was delivered by nickel iron oxyhydroxide catalyst. The resultant decoupled configuration displayed charge-discharge overpotentials comparable to the ORR and OER as delivered by Pt/C and IrO₂ counterparts respectively. However, rather high cost of tellurium makes its application as infeasible on commercial scale. On the other hand, Jin et al. and co-workers developed heteroatom doped Fe-based Fe-N-P carbon material by utilizing LiFePO₄ hazardous wastes.^[247] LiFePO₄ efficiently served as a source of Fe and P and ZIF-8 precursor was used to provide N-doped porous carbon network, thus Fe₂P catalyst was encapsulated by carbon nanotubes. When the resultant catalyst was applied as an air electrode in

ZABs, it demonstrated a peak power density of $140 \text{ mW} \cdot \text{cm}^{-2}$ with a half-wave potential of 0.88 V in alkaline media.

Recently, Yu et al. designed a hybrid material by depositing ZIF-67 onto the CeO_2 surface.^[129] Following the pyrolysis, the hybrid material transformed into $\text{CeO}_2/\text{Co}@N$ -doped carbon. $\text{CeO}_2/\text{Co}@N$ -C exhibited decent ORR and OER catalytic performance as a result of the synergistic effect between CeO_2 and $\text{Co}@N$ -C. CeO_2 led to the creation of multiple Ce^{3+} and oxygen vacancies. Oxygen vacancies are capable of binding O_2 adsorbates stronger than oxide materials sites, and is favourable for the promotion of oxygen electrocatalysis. Moreover, the graphitic and pyridinic N content in the carbon framework eventually accelerated the electron transport.^[248]

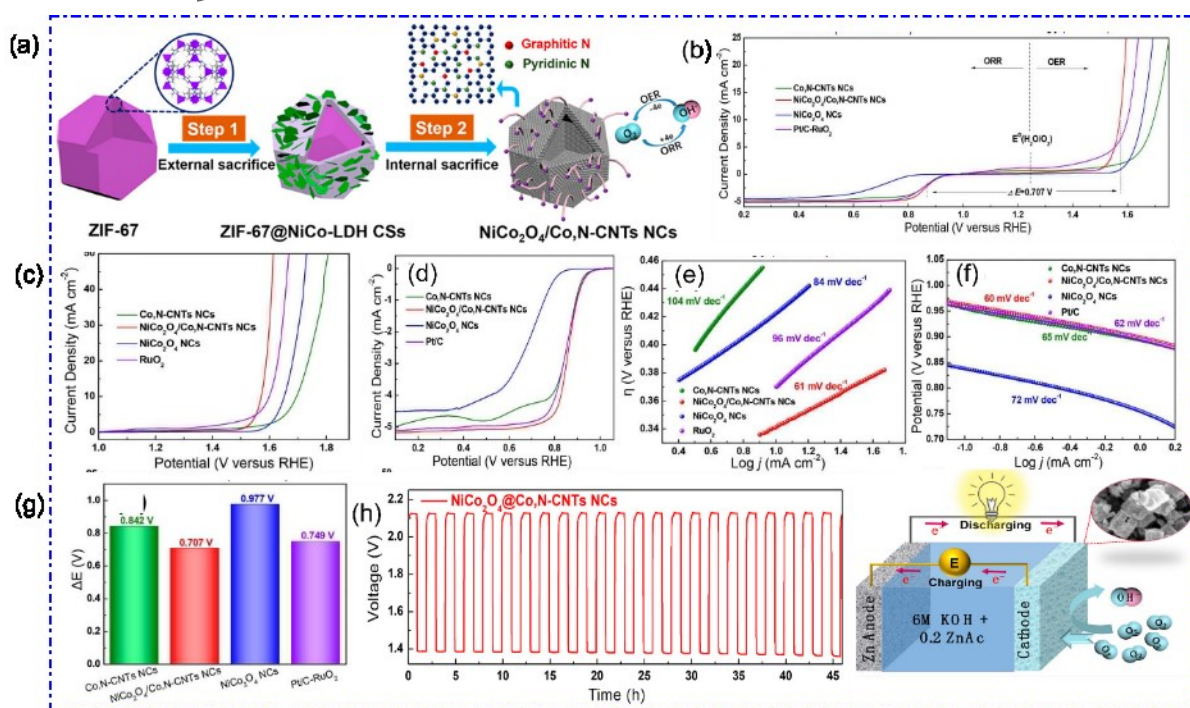


Fig. 22 (a) Schematic illustration for the synthesis of $\text{NiCo}_2\text{O}_4/\text{Co,N-CNTs}$ nanocages. (b) iR-corrected LSV curves of Co,N-CNTs NCs, $\text{NiCo}_2\text{O}_4/\text{Co,N-CNTs}$ NCs, NiCo_2O_4 NCs, and Pt/C-RuO₂ catalysts in the full OER/ORR region; (c,d) iR-corrected LSV curves and corresponding (e,f) Tafel plots of Co,N-CNTs NCs, $\text{NiCo}_2\text{O}_4/\text{Co,N-CNTs}$ NCs, NiCo_2O_4 NCs, Pt/C and RuO₂ at a scan rate of $5 \text{ mV} \cdot \text{s}^{-1}$; (g) Value of ΔE for Co,N-CNTs NCs, $\text{NiCo}_2\text{O}_4/\text{Co,N-CNTs}$ NCs, NiCo_2O_4 NCs, and Pt/C-RuO₂ catalysts derived from ($\Delta E = E_{j_{10}} - E_{j_{1/2}}$); (h) Galvanostatic discharge-charge performance of $\text{NiCo}_2\text{O}_4/\text{Co,N-CNTs}$ NCs at 5 mA cm^{-2} current density with an interval of 1 h. Reproduced with permission.^[127] Copyright 2018, American Chemical Society.

4. Conclusion and perspectives

ZIFs, as a subclass of MOFs, possess fascinating electrochemical features, such as high electrical conductivity, large specific surface area, open pore structure, homogeneous distribution of the elements inside the frameworks on atomic scale, electrochemical stability and so forth, which

qualify them as an efficient air electrodes for ZABs. Upon the pyrolysis of ZIFs, atomically dispersed and prominently exposed transition metal nanoparticles embedded into N heteroatom-doped carbonaceous scaffold are obtained, providing lucrative electrocatalytic features which are feasible for the development of air electrodes for ZABs. For instance, the presence of transition metals like Co and Fe in ZIFs deliver dual advantages: impart the catalytic graphitization effect to the carbon; and it markedly reduces the adsorption free energy of oxygen by promoting the conduction of electrons from carbon to oxygen, thereby leading to the enhanced ORR activity. Likewise, N heteroatoms break the electro-neutrality of neighbouring carbon atoms and generating positive sites, which are beneficial for the adsorption of O₂ molecules, thus contributing to the ORR activity. In case of ZIF-derived materials, it may be applied without additional conducting material e.g. carbon black and it also protects them against corrosion. Moreover, ZIFs are also capable of producing interconnected hierarchical macro-meso-microporous network obtained following the washing/acid etching of NaCl/SiO₂ template. Hierarchical porous network ensures the accessible surface area for the efficient oxygen/electrolyte transport and reduces the mass transfer resistance, thus contributing to the upgraded electrocatalytic activity. Another important characteristic of ZIFs is their allowance of the exceptional structural and chemical tunability which offer a rich platform to design the variety of oxygen electrocatalysts by varying the metal or organic linker precursors or by synthesis conditions. Based on these features, considerable research activities have been conducted for the transformation of ZIFs precursors into various value-added oxygen electrocatalysts and their application as air electrode in ZABs. For instance, N,P, S non-metal element -doped metal-free carbon, transition metal doped carbon, single atom modified carbon, alloy/ carbon composite, transition metal oxide/carbon composite, CoN₄/carbon composite and hybrid materials etc. have been fabricated. These makeovers of ZIFs significantly modify their electrocatalytic properties which help in achieving very promising performance of ZABs. Recently, ZIFs have been demonstrated outstanding ORR performance even superior to that of commercial Pt/C catalyst. In brief, ZIFs based materials have been critically summarized with the perspective of synthesis, morphology, structure and properties and correlated them with the performance indicators of ZABs.

Although ZIF based materials have been made great advances in designing the air electrodes for their application in ZABs, there is still a big room for the improvement, which are likely to allow us for the tremendous research opportunities in the future. It has been found that ZIF-67 and ZIF-8 with SOD topology have been extensively employed for the synthesis of ZIF-based air electrodes. However, the rest of topologies such as RHO, LTA ... etc. have rarely been utilized, thus the potential of all ZIFs as air electrode in ZABs is still unexplored and have not been fully exploited yet. Therefore, there are enormous opportunities for the development of air electrodes from other ZIFs topologies besides SOD. Moreover, it is crucial to correlate the different topologies with electrocatalytic performance and find a relationship between different topologies, their physico-

chemical properties and electrocatalytic activity. Furthermore, it calls for the optimization of the potential ZIFs topology rendering the promising performance in terms of activity and stability as an air electrode for ZABs.

Also, it can be witnessed by the comparative analysis of various morphologies of ZIFs obtained via materials tuning, morphological control or by the hybridization (**Table. 1**), ZIFs lose their typical polyhedral morphology and structural integrity accompanied by the reduction in surface area following the pyrolysis at high temperature. Therefore, it is important to retain their typical polyhedral morphology to fully utilize the potential of morphological features. On the other hand, pyrolysis of ZIFs is vital for the transformation of N-doped porous network into transition metal embedded and N-doped conductive carbon network. Therefore, we have to make a trade-off between electronic conductivity and fascinating polyhedral morphology. As a result, it is inevitable to devise some electron conducting pristine ZIFs. This discovery would enable the deployment of pristine ZIF without sacrificing the high surface area and typical ZIF morphology. Another feasible solution to meet this challenge may be the addition of some conductive type of carbon to the pristine ZIFs.

Despite the fact that ZIF-derived M-N-C air electrodes have exhibited the tremendous ORR activity even superior to that of the commercial Pt/C catalysts, however, their OER activity without fine-tuning is inadequate. Therefore, a long way to go in achieving the OER activity of ZIF-derived M-N-C catalysts comparable to the IrO₂ counterparts. On the other hand, the development of rechargeable ZABs is not feasible unless the air electrode exhibit the bi-functional activity. Thus, ZIF based materials may be coupled with some OER active materials to render hybrid materials possessing excellent bi-functional activity. Moreover, ZIFs may also be coupled with other MOFs, therefore, it could be more worthwhile when ZIFs are hybridized with other OER active MOFs.

As ZIFs possess large aperture of windows and relatively larger interior cages, therefore they may be served as a great platform to host OER active moieties by applying the guest-host strategy. This approach is also useful for immobilizing or encapsulating the large molecules. Additionally, the trapping of OER active guest species could be a beneficial strategy to provide the intimate contact and to have the better control over the size of particles, thereby avoiding the agglomeration. Based on variety of ZIFs topologies, there is huge liberty in designing the host-guest composites. For instance, when ZIFs with SOD topology and pore size of ~12 Å is not capable of hosting large molecules, then ZIFs possessing the RHO topology with pore size of ~22 Å, may be employed to accommodate the larger ones. Similarly, when ZIFs with large window and large pore size is required, the GME topology may be opted.

In-situ growth of ZIFs polyhedrons on different templates was also found as a promising route to suppress the inter-particle resistance and to avoid the aggregation of catalytic species. Thus, this

strategy might be useful for developing the bi-functional electrocatalyst for ZABs. For instance, ZIF-67-derived Co-N-C as ORR active material may be grown on some OER active materials to furnish the bi-functional air electrode to be employed in ZABs.

Recently, metal free carbons have emerged as the substitute to expensive transition metals or precious metal based air electrodes. As ZIF-8 is employed as a precursor to provide metal-free carbon, ZIF derived metal free carbon after the introduction of extrinsic defects (heteroatom doping: N, P, B, S, halogens) have demonstrated remarkable ORR activity. On the other hand, the intrinsic defects (topological defects, edge sites, vacancies and holes) in carbon lattice have been found to have strong impact on charge transfer, electronic configuration and electrocatalytic performance. Therefore, defect-induced carbon has also been found to reveal phenomenal bi-functional activities. However, it was noticed that the induction of intrinsic defects has scarcely been exploited in the ZIF derived carbon. As ZIFs consist of self-doped N, therefore, together with the N-doped carbon, the induction of intrinsic defects through controlled synthesis could substantially enhance the bi-functional activity of air electrode. Moreover, the induction of intrinsic defects in combination with other extrinsic defects (B, P, S, halogens) and even with metal based ZIFs may also be utilized to improve the electrocatalytic activity.

The doping of N and/or P heteroatoms to carbon matrix in the ZIFs have displayed phenomenal electrocatalytic performance. Actually, the N and/or P doping induce more positive sites, which are favourable for the adsorption of oxygen molecules leading to the excellent electrocatalytic activity. On the other hand, these positive sites are also conducive for the adsorption of SO_3^{2-} and NO_2^- anions, which impart poisoning effect to the ZIF electrocatalysts. As a result, the active sites are blocked, yielding unstable catalytic activity for ZABs. Moreover, SO_3^{2-} and NO_2^- species create acidic environment, which is considered detrimental to ZIFs and leading to their degradation. Consequently, it is crucial to confront this challenge without sacrificing the adsorption sites. Also, it is important to enhance the stability of ZIFs in acidic media. This opportunity would also pave the way for their feasibility in acidic ZABs for future applications.

It is customary that the different metals have been mixed in the ZIFs together to enhance their bi-functional activity and/or electrocatalytic properties under different conditions. However, upon pyrolysis, multi-metallic ZIFs more likely yield some materials consisting of mixed phase instead of a single phase. Actually, the calcination of multi-metallic ZIFs at elevated temperature leading to the loss of control over ZIFs synthesis. Eventually, in order to get a single phase material following the pyrolysis, a systematic strategy is required to control the ZIFs synthesis on atomic scale.

Large amount of organic solvents have been generally employed in solvothermal/hydrothermal synthesis as a reaction medium for the synthesis of ZIFs. The solvents used in these synthesis strategies are expensive, toxic, flammable and detrimental to the ecology and

require high energy input. Therefore, it is urgent to quest for some environmentally benign and inexpensive solvents and low heat energy requirement for the large scale production of ZIFs. For this purpose, mechanosynthesis could be a promising substitute to the conventional solvent-based synthesis.

As the Co atoms are capable of exhibiting several oxidation states, which are considered favourable for OER and ORR activities, thereby displaying bi-functional activity. However, when Co containing ZIF (ZIF-67) undergoes pyrolysis, Co species indispensably lose control over the oxidation state upon pyrolysis and reduce to metallic Co species. Therefore it is vital to devise some strategy to control the oxidation state of Co in ZIF-67 for the efficient bi-functional activity of ZABs.

The stable behaviour of ZIFs in different chemical environment, for instance, organic or aqueous provides an impetus for conducting the covalent modifications on organic ligands without deteriorating the underlying topology of ZIF architecture. The functionality, pore size, shape of ZIFs may be controlled by adopting organic linker modification or linker exchange. In this perspective, solvent-assisted linker exchange (SALE) may be regarded as an efficient strategy. In pursuance of SALE reaction, the linkers are exchanged and daughter ZIF carry the original ZIF topology, although secondary linker had already replaced the original ZIF linker, which are infeasible de novo. SALE also incorporates the new properties to daughter ZIF such as active sites, selectivity, control of the catenation, etc. Thus, this stunning feature may also be utilized to impart different functionalities.

When ZIFs based air electrodes were integrated in ZABs, their OER and ORR activities were found as more stable in contrast to the transition metal based counterparts. However, the ORR activity was initially low and then started to rise as time progressed. Despite the great advances, the mechanisms of ORR and OER of ZIF-derived materials are still elusive. Therefore, it is crucial to delve deeper into the electrocatalytic ORR as well as OER mechanism through a combination of in-situ or operando characterizations, molecular simulation and DFT computations, which could furnish instantaneous inspection of complex reactions and disclose the reactivity of ZIF-based air electrodes on atomic scale. These findings would allow the designing of the highly active and stable ZIF-based air electrodes.

All in all, ZIF and ZIF- derived materials have enormous potential to serve as OER/ORR active bi-functional electrocatalyst and for the application in ZABs. Moreover, the development of cost-effective, energy efficient, reproducible and scalable ZIFs would propel their application on industrial scale. This comprehensive overview would provide the recent advances of ZIF-derived with perspective of ZABs and usher the next generation of OER/ORR active electrocatalysts. Besides ZABs, this review would also provide a comprehensive guideline for rationally designing the ZIF

based electrocatalysts for the energy conversion and storage, which are equally important in cross-cutting applications.

Author Manuscr

This article is protected by copyright. All rights reserved.

Table. 2 The performance indicators of ZABs evaluated by applying the ZIF-derived air electrodes

electrode	Battery Electrolyte	Open circuit voltage (OCV)	Onset potential	Peak power density	Specific capacity	Durability
		(V)	(V)	(mW cm ⁻²)	(mA h g Zn ⁻¹)	
Metal free carbon						
CTC-850	6 M KOH+ 0.2 M ZnCl ₂	1.47	0.92	74	730	30 h @5 mA cm ⁻²
NHCC-800	6 M KOH+ 0.2 M Zn(CH ₃ COO) ₂	1.49	0.94	248	-	12 h @10 mA cm ⁻²
PC - 950	6 M KOH	1.44	0.93	197	797	200 h
Single transition metal-doped carbons						
-PHCNTs	6 M KOH+ 0.2 M Zn(CH ₃ COO) ₂	1.40	0.98	125.41	-	673 h @ 5 mA cm ⁻²
CS@CNT	6 M KOH+ 0.2 M Zn(CH ₃ COO) ₂	1.42	0.93	90	798	30 h @ 5 mA cm ⁻²
NCP/rGO-800	6 M KOH	1.47	0.94	186	909	250000 s @ 10 mA cm ⁻²

This is the author manuscript accepted for publication and has undergone full peer review but has not been through the copyediting, typesetting, pagination and proofreading process, which may lead to differences between this version and the [Version of Record](https://doi.org/10.1002/aenm.202100514). Please cite this article as [doi: 10.1002/aenm.202100514](https://doi.org/10.1002/aenm.202100514).

This article is protected by copyright. All rights reserved.

@NCNT	Alkaline	1.50	0.95	138.82	-	16 h
						10 @ mA cm ⁻²
e/N/C	6 M KOH+	1.34	1.06	22.2	928	120 cycles
	0.2 M Zn(CH ₃ COO) ₂					@5 mA cm ⁻²
/NGC-3	6 M KOH+	1.41	0.97	134.4	716	120 h
	0.2 M Zn(CH ₃ COO) ₂					@5 mA cm ⁻²
Co@NC	6 M KOH+	-	0.95	303.7	751.4	100 h
	0.2 M ZnCl ₂					@2 mA cm ⁻²
mNSP - C	6 M KOH+	-	1.0	124	-	80 h
	0.2 M ZnCl ₂					@20 mA cm ⁻²
/NC-800	6 M KOH+	1.40	0.90	114	695	35 h
	0.2 M Zn(CH ₃ COO) ₂					@10 mA cm ⁻²
P-NC-700	6 M KOH+	1.51	0.98	116.5	-	80 h
	0.2 M Zn(CH ₃ COO) ₂					@10 mA cm ⁻²
5Se@NC.	6 M KOH+	1.40	0.912	268	-	30 h
	0.2 M Zn(CH ₃ COO) ₂					@10 mA cm ⁻²
Transition Metal Oxides						
e _{0.32} O@NC	6 M KOH+	1.30	0.92	52 (Flexible ZABs)	673	150 h
	0.2 M Zn(CH ₃ COO) ₂					@5 mA cm ⁻²

Co ₃ O ₄ - 90	6 M KOH+ 0.2 M Zn(CH ₃ COO) ₂	1.44	0.91	82.0	387.2	120 h @10 mA cm ⁻²
Co ₃ O ₄ @PGS	6 M KOH+ 0.2 M Zn(CH ₃ COO) ₂	1.45	0.97	118.27	-	800 h @10 mA cm ⁻²
Co@Fe-N-C	6 M KOH+ 0.2 M Zn(CH ₃ COO) ₂	1.48	1.01	92	-	-
Bimetallic transition metals-doped carbons						
Fe _{2.1} C/NC	6 M KOH+ 0.2 M Zn(CH ₃ COO) ₂	1.5	0.93	160	635	332 h @5 mA cm ⁻²
N - CNTs	6 M KOH+ 0.2 M Zn(CH ₃ COO) ₂	1.37	0.97	101	-	15 h @2 mA cm ⁻²
Single metal atom modified carbons						
M-Fe-N-C	6.0 M KOH	1.45	0.93	235	768.3	100 h @5 mA cm ⁻²
C-Co SA	6 M KOH+ 0.2 M Zn(CH ₃ COO) ₂	1.41	1.0	20.9	-	180h
	6 M KOH+	1.45	0.95	195.0	-	56 h

s/NPS-HC	0.2 M Zn(CH ₃ COO) ₂						
	6 M KOH+	1.51	0.94	96.4	641	300h	
- N _x - C	0.2 M Zn(CH ₃ COO) ₂					@5 mA cm ⁻²	
bedded PNC	6M KOH	1.55	0.997	118	-	40 h	@5 mA cm ⁻²
e-N/C	6 M KOH+	1.53	1.04	121.8	-	50 cycles	
@NCF/CNF	0.2 M Zn(CH ₃ COO) ₂	1.41	0.99	-	-	90 cycles	@10 mA cm ⁻²
C nanosheets	6 M KOH+	1.49	0.96	194	690	20h	
	0.2 M ZnCl ₂						
SA-N-C	6 M KOH+	-	0.94	92.2	634.2	10000	
	0.2 M ZnCl ₂						
		Core/Shell					
-CNTA	6 M KOH+	1.41	0.90	157.3	-	40 h	
	0.2 M Zn(CH ₃ COO) ₂					@10 mA cm ⁻²	

C@BMZIF	6 M KOH+ 0.2 M Zn(CH ₃ COO) ₂	1.48	0.95	235	-	17 h @10 mA cm ⁻²
N _x /C NRA	6 M KOH	1.42	0.94	193.2	-	80 h @ 50 mA cm ⁻²
@Co-N/C	6 M KOH+ 0.2 M Zn(CH ₃ COO) ₂	1.43	0.83	130.3	-	633 h @5 mA cm ⁻²
DH@Fe/CNP	6 M KOH	-	0.91	-	-	30 h @ 1mA cm ⁻²
CoN₄/Carbon composite						
N@NC-2	6 M KOH+ 0.2 M Zn(CH ₃ COO) ₂	1.48	0.93	74.3	769.4	335 h @10 mA cm ⁻²
Co ₄ N@N-C	6 M KOH+ 0.2 M Zn(CH ₃ COO) ₂	1.46	0.89	105	806	40 h @ 5 mA cm ⁻²
@N-CNTs/rGO	6 M KOH	1.45	~0.92	200	783	440 h @ 5 mA cm ⁻² with 2 h per cycle
/CNW/CC	6 M KOH+		~0.9	174	774	135 h

	0.2 M Zn(CH ₃ COO) ₂					@10 mA cm ⁻²
Nanofibers from electrospinning						
CNTs@CNF	6 M KOH	1.42	0.88	260	-	250 h @ 5 mA cm ⁻²
N@ZIF-67	6 M KOH	~1.53	-0.11	63	-	300 cycles @ 5 mA cm ⁻²
Zn/CoNC	6 M KOH+ 0.2 M Zn(CH ₃ COO) ₂	1.46	0.91	140.1	680.2	410 h @2 mA cm ⁻²
N-HCNFs	6 M KOH+ 0.2 M Zn(CH ₃ COO) ₂	1.37	-	50	-	260 cycles @20 mA cm ⁻²
Co-N/P-9	6 M KOH+0.2 M ZnCl ₂	1.39	0.96	-	565	130 cycles @ mA cm ⁻²
MoS ₂ /N- s@CNFs	6 M KOH	1.42	0.98	222	-	40 h @ 5 mA cm ⁻²
Alloys/Carbon composites						
e/N-HCSs	6 M KOH+ 0.2 M Zn(CH ₃ COO) ₂	1.39	0.901	96.5	777.4	160 h @ 5 mA cm ⁻²
IG-CoFe	6 M KOH+	-	0.98	97.7	-	18h

	0.2 M Zn(CH ₃ COO) ₂					@10 mA cm ⁻² h/ cycle
Ni@NCNT	6.0 M KOH+ 0.2 M ZnCl ₂	1.44	0.95	114	-	100 cycle @10 mA cm ⁻²
I-CPCF-950	6 M KOH+ 0.2 M Zn(CH ₃ COO) ₂	1.48	0.96	160.6	751	640 h @10 mA cm ⁻²
ZIFs-based hybrids						
T@CNT	6 M KOH+ 0.2 M Zn(CH ₃ COO) ₂	1.45	~0.95	160.6	781.7	117 h @20 mA cm ⁻²
-ZIF@GO	6 M KOH+ 0.2 M Zn(CH ₃ COO) ₂	1.35	0.89	39.5	-	20 h @10 mA cm ⁻²
NCTs-800	6 M KOH+ 0.2 M Zn(CH ₃ COO) ₂	1.45	~0.95	149	746	500h @ 5 mA cm ⁻²
Co,N-CNTs NCs	6 M KOH+ 0.2 M Zn(CH ₃ COO) ₂	1.45	~0.95	173.7	-	45 h @5 mA cm ⁻² cycling interval of 1 h
@N-doped C	6 M KOH+ 0.2 M Zn(CH ₃ COO) ₂	1.42	0.998	102.7	-	70 h @ 5 mA cm ⁻²

Author Manuscript

CeO ₂ /Co-NC	6 M KOH+	1.40	0.92	164.2	-	400 h
	0.2 M Zn(CH ₃ COO) ₂					@ 5 mA cm ⁻²

Acknowledgements

This work was supported by the Australian Research Council Discovery Project, Grant No. DP200103332 and DP200103315. The authors would like to acknowledge the support provided by the “Australian Government Research Training Program (RTP) Scholarship” at Curtin University, Perth, Australia.

Conflict of Interest

The authors declare no conflict of interest.

Biographies of the authors



Mr. Yasir Arafat is currently pursuing his PhD degree in Chemical Engineering at Curtin University, Australia. His research interests include the fabrication of functional materials for the energy conversion and energy storage systems, viz., reforming reactions, Zn-air batteries, all-solid-state lithium batteries. Currently, the main focus of his research is the development of porous carbon, metal organic frameworks (MOFs), perovskites and their composites for the energy storage systems and deciphering their role in enhancing the performance.



This is the author manuscript accepted for publication and has undergone full peer review but has not been through the copyediting, typesetting, pagination and proofreading process, which may lead to differences between this version and the [Version of Record](#). Please cite this article as [doi: 10.1002/aenm.202100514](#).

This article is protected by copyright. All rights reserved.

Dr. Muhammad Rizwan Azhar received his PhD degree in Chemical Engineering from Curtin University in 2018. After graduation joined Edith Cowan University as Research Fellow and currently working on fundamental applied research projects on Water-Energy Nexus. His current research focuses on synthesis of Metal Organic Frameworks (MOFs), porous carbons, perovskite/MOFs composite for water treatment and energy applications. He has keen interest in integrating academic research into product/process oriented outcomes through collaborations with industry and government agencies.



Mr. Yijun Zhong is currently a PhD candidate at Curtin University, Australia. His research focuses on developing functional materials for high-efficient energy storage, e.g., lithium/sodium-ion batteries, lithium-sulfur batteries, and zinc-based batteries. His primary interests lie in understanding the effect of structure, composition, and morphology on catalytic and electrochemical properties of these materials.



Prof. Moses Tade is a John Curtin Distinguished Professor in Chemical Engineering at Curtin University. He has reputation nationally and worldwide for his research in chemical engineering and specifically in process systems engineering (PSE). He has significantly contributed to bridging the gap between theoretical work and industrial practice of PSE over an extensive academic career. He has received substantial funding for his work from industry and the Australian Research Council;

This article is protected by copyright. All rights reserved.

Author Manuscript

supervised over 60 PhD students, several Master students and postdocs; included in the Highly Cited Researcher Lists (Clarivate Web of Science, 2019 and 2020) in the Cross Discipline Research field.



Prof. Zongping Shao is a professor of chemical engineering at Curtin University, Australia and Nanjing Tech University, China. He obtained his PhD from Dalian Institute of Chemical Physics, China in 2000. He worked as a visiting scholar at Institut de Recherches Sur La Catalyse, CNRS, France and postdoc at California Institute of Technology, USA from 2000 till 2005. His research interests include mixed conducting membranes for oxygen permeation, solid oxide fuel cells, room-temperature electrocatalysts, advanced energy storage devices including lithium/sodium-(ion) batteries, metal-air batteries and supercapacitors, etc. He has published more than 650 international journal papers with a total citation of >36000 and an H-index of 89 (Google Scholar). He was selected as one of the highly cited researchers (2014, 2017-2020) by Clarivate Analytics and as one of the highly cited Chinese researchers by Elsevier China (2015-2019).

References

- [1] a) A. S. Al-Fatesh, Y. Arafat, S. O. Kasim, A. A. Ibrahim, A. E. Abasaheed, A. H. Fakeeha, *Appl. Catal. B* **2021**, *280*, 119445; b) H. Ren, W. Wang, S. Woo Joo, Y. Sun, C. Gu, *Mater. Res. Bull.* **2019**, *111*, 34; c) A. Patil, V. Patil, D. Wook Shin, J.-W. Choi, D.-S. Paik, S.-J. Yoon, *Mater. Res. Bull.* **2008**, *43*, 1913; d) A. S. Al-Fatesh, Y. Arafat, A. A. Ibrahim, S. O. Kasim, A. Alharthi, A. H. Fakeeha, A. E. Abasaheed, G. Bonura, F. Frusteri, *Catalysts* **2019**, *9*, 473.
- [2] a) T. C. Mendes, C. Nguyen, A. J. Barlow, P. V. Cherepanov, M. Forsyth, P. C. Howlett, D. R. MacFarlane, *Sustain. Energy Fuels* **2020**, *4*, 2322; b) A. S. Al-Fatesh, Y. Arafat, A. A. Ibrahim, H. Atia, A. H. Fakeeha, U. Armbruster, A. E. Abasaheed, F. Frusteri, *Appl. Catal., A* **2018**, *567*, 102; c) A. S. Al-Fatesh, Y. Arafat, H. Atia, A. A. Ibrahim, Q. L. M. Ha, M. Schneider, M. M-Pohl, A. H. Fakeeha, *J. CO₂ Util.* **2017**, *21*, 395.
- [3] C. Lin, X. Li, S. S. Shinde, D.-H. Kim, X. Song, H. Zhang, J.-H. Lee, *ACS Appl. Energy Mater.* **2019**, *2*, 1747.
- [4] P. Ralon, M. Taylor, A. Ilas, H. Diaz-Bone, K. Kairies, *International Renewable Energy Agency: Abu Dhabi, UAE* **2017**.
- [5] Y. Zhong, X. Xu, J.-P. Veder, Z. Shao, *Iscience* **2020**, *23*, 100943.
- [6] a) G. Fu, Y. Chen, Z. Cui, Y. Li, W. Zhou, S. Xin, Y. Tang, J. B. Goodenough, *Nano Lett.* **2016**, *16*, 6516; b) P. G. Bruce, S. A. Freunberger, L. J. Hardwick, J.-M. Tarascon, *Nat. Mater.* **2012**, *11*, 19; c) Z. P. Cano, M. G. Park, D. U. Lee, J. Fu, H. Liu, M. Fowler, Z. Chen, *J. Phys. Chem. C* **2018**, *122*, 20153; d) K. Kim, Y.-H. Cho, S. W. Eom, H.-S. Kim, J. H. Yeum, *Mater. Res. Bull.* **2010**, *45*, 262; e) P. Tan, B. Chen, H. Xu, H. Zhang, W. Cai, M. Ni, M. Liu, Z. Shao, *Energy Environ. Sci.* **2017**, *10*, 2056; f) X. Xu, W. Wang, W. Zhou, Z. Shao, *Small Methods* **2018**, *2*, 1800071.
- [7] a) J. S. Lee, S. Tai Kim, R. Cao, N. S. Choi, M. Liu, K. T. Lee, J. Cho, *Adv. Energy Mater.* **2011**, *1*, 34; b) S. S. Shinde, C.-H. Lee, A. Sami, D.-H. Kim, S.-U. Lee, J.-H. Lee, *ACS nano* **2017**, *11*, 347; c) Y. Zhong, X. Xu, P. Liu, R. Ran, S. P. Jiang, H. Wu, Z. Shao, *Adv. Energy Mater.* **2020**, *10*, 2002992.
- [8] a) Y. Li, H. Dai, *Chem. Soc. Rev.* **2014**, *43*, 5257; b) J. Fu, F. M. Hassan, J. Li, D. U. Lee, A. R. Ghannoum, G. Lui, M. A. Hoque, Z. Chen, *Adv. Mater.* **2016**, *28*, 6421.
- [9] a) J. Yin, Y. Li, F. Lv, Q. Fan, Y.-Q. Zhao, Q. Zhang, W. Wang, F. Cheng, P. Xi, S. Guo, *ACS nano* **2017**, *11*, 2275; b) R. Cao, J. S. Lee, M. Liu, J. Cho, *Adv. Energy Mater.* **2012**, *2*, 816.
- [10] a) B. Y. Xia, Y. Yan, N. Li, H. B. Wu, X. W. D. Lou, X. Wang, *Nat. Energy* **2016**, *1*, 1; b) S. Shinde, C. Lee, A. Sami, D. Kim, S. Lee, J. Lee, *Liu, W. Li, L. Duan, X. Li, L. Ji, Z. Geng, K. Huang, L. Lu, L. Zhou, Z. Liu, W. Chen, L. Liu, S. Feng, Y. Zhang, Nano Lett* **2015**, *15*, 5137.
- [11] a) J.-K. Sun, Q. Xu, *Energy & Environmental Science* **2014**, *7*, 2071; b) H. Furukawa, K. E. Cordova, M. O'Keeffe, O. M. Yaghi, *Science* **2013**, *341*, 1230444; c) G. Xu, P. Nie, H. Dou, B. Ding, L. Li, X. Zhang, *Mater. Today* **2017**, *20*, 191; d) W. Liu, X.-B. Yin, *Trends Analyt. Chem.* **2016**, *75*, 86.
- [12] a) P. C. Lemaire, J. Zhao, P. S. Williams, H. J. Walls, S. D. Shepherd, M. D. Losego, G. W. Peterson, G. N. Parsons, *ACS Appl. Mater. Interfaces* **2016**, *8*, 9514; b) F. Zheng, Y. Yang, Q. Chen, *Nat. Commun.* **2014**, *5*, 1.
- [13] M. Wu, G. Zhang, M. Wu, J. Prakash, S. Sun, *Energy Stor. Mater.* **2019**, *21*, 253.
- [14] a) W. Gan, D. Zhou, L. Zhou, Z. Zhang, J. Zhao, *Electrochimica Acta* **2015**, *182*, 430; b) P. Pei, K. Wang, Z. Ma, *Applied Energy* **2014**, *128*, 315; c) M. Wu, Q. Tang, F. Dong, Y. Wang,

- D. Li, Q. Guo, Y. Liu, J. Qiao, *Phys. Chem. Chem. Phys.* **2016**, *18*, 18665; d) F. R. McLarnon, E. J. Cairns, *J. Electrochem. Soc.* **1991**, *138*, 645.
- [15] P. Sapkota, H. Kim, *J. Ind. Eng. Chem.* **2009**, *15*, 445.
- [16] P. Chen, K. Zhang, D. Tang, W. Liu, F. Meng, Q. Huang, J. Liu, *Front. Chem.* **2020**, *8*.
- [17] X. Cai, L. Lai, J. Lin, Z. Shen, *Mater. Horizons* **2017**, *4*, 945.
- [18] a) D. M. See, R. E. White, *J. Chem. Eng. Data* **1997**, *42*, 1266; b) C. K. Dyer, P. T. Moseley, Z. Ogumi, D. A. Rand, B. Scrosati, J. Garche, *Encyclopedia of electrochemical power sources*, Elsevier Science & Technology, **2009**.
- [19] Z. Wang, Y. Lu, Y. Yan, T. Y. P. Larissa, X. Zhang, D. Wu, H. Zhang, Y. Yang, X. Wang, *Nano Energy* **2016**, *30*, 368.
- [20] V. Caramia, B. Bozzini, *Mater. Renew. Sustain. Energy* **2014**, *3*, 28.
- [21] a) M. Xu, D. G. Ivey, Z. Xie, W. Qu, *J. Power Sources* **2015**, *283*, 358; b) Y. N. Jo, H. S. Kim, K. Prasanna, P. R. Ilango, W. J. Lee, S. W. Eom, C. W. Lee, *Ind Eng Chem Res* **2014**, *53*, 17370; c) Y. N. Jo, K. Prasanna, S. H. Kang, P. R. Ilango, H. S. Kim, S. W. Eom, C. W. Lee, *J. Ind. Eng. Chem.* **2017**, *53*, 247.
- [22] M. Wang, W. Wang, T. Qian, S. Liu, Y. Li, Z. Hou, J. B. Goodenough, P. M. Ajayan, C. Yan, *Adv. Mater.* **2019**, *31*, 1803339.
- [23] A. R. Mainar, O. Leonet, M. Bengoechea, I. Boyano, I. de Meatza, A. Kvasha, A. Guerfi, J. Alberto Blázquez, *Int. J. Energy Res.* **2016**, *40*, 1032.
- [24] G. Janani, Y. Chae, S. Surendran, Y. Sim, W. Park, J. K. Kim, U. Sim, *Appl. Sci.* **2020**, *10*, 3165.
- [25] J.-S. Lee, S. Tai Kim, R. Cao, N.-S. Choi, M. Liu, K. T. Lee, J. Cho, *Adv. Energy Mater.* **2011**, *1*, 34.
- [26] C. Debiemme - Chouvy, J. Vedel, M. C. Bellissent - Funel, R. Cortes, *J. Electrochem. Soc.* **1995**, *142*, 1359.
- [27] D. Schröder, U. Krewer, *Electrochim. Acta* **2014**, *117*, 541.
- [28] S. Hosseini, S. Masoudi Soltani, Y.-Y. Li, *Chem. Eng. J.* **2021**, *408*, 127241.
- [29] J. Fu, Z. P. Cano, M. G. Park, A. Yu, M. Fowler, Z. Chen, *Adv. Mater.* **2017**, *29*, 1604685.
- [30] Z. Zhao, X. Fan, J. Ding, W. Hu, C. Zhong, J. Lu, *ACS Energy Lett.* **2019**, *4*, 2259.
- [31] Y. Arafat, M. R. Azhar, Y. Zhong, M. O. Tadé, Z. Shao, *Mater. Res. Bull.* **2021**, *140*, 111315.
- [32] X. Chen, Z. Zhou, H. E. Karahan, Q. Shao, L. Wei, Y. Chen, *Small* **2018**, *14*, 1801929.
- [33] Z.-L. Wang, D. Xu, J.-J. Xu, X.-B. Zhang, *Chem. Soc. Rev.* **2014**, *43*, 7746.
- [34] D. Yang, L. Zhang, X. Yan, X. Yao, *Small Methods* **2017**, *1*, 1700209.
- [35] M. Wu, Q. Tang, F. Dong, Z. Bai, L. Zhang, J. Qiao, *J. Catal.* **2017**, *352*, 208.
- [36] a) X. Xu, C. Su, W. Zhou, Y. Zhu, Y. Chen, Z. Shao, *Adv. Sci.* **2016**, *3*, 1500187; b) Y. Pan, X. Xu, Y. Zhong, L. Ge, Y. Chen, J.-P. M. Veder, D. Guan, R. O'Hayre, M. Li, G. Wang, H. Wang, W. Zhou, Z. Shao, *Nat. Commun.* **2020**, *11*, 2002; c) X. Xu, Y. Pan, Y. Zhong, R. Ran, Z. Shao, *Mater. Horizons* **2020**, *7*, 2519.
- [37] a) *Chem. Rev.* **2012**, *112*, 673; b) H.-C. J. Zhou, S. Kitagawa, *Chem. Soc. Rev.* **2014**, *43*, 5415; c) M. Gomar, S. Yeganegi, *Materials Science and Engineering: C* **2019**, *97*, 461; d) A. Zanon, F. Verpoort, *Coord. Chem. Rev.* **2017**, *353*, 201.
- [38] O. Yaghi, G. Li, *Angew. Chem. Int. Ed.* **1995**, *34*, 207.
- [39] a) H.-L. Jiang, B. Liu, Y.-Q. Lan, K. Kuratani, T. Akita, H. Shioyama, F. Zong, Q. Xu, *J. Am. Chem. Soc.* **2011**, *133*, 11854; b) J. Zhou, R. Li, X. Fan, Y. Chen, R. Han, W. Li, J. Zheng, B. Wang, X. Li, *Energy Environ. Sci.* **2014**, *7*, 2715.
- [40] a) T. Devic, C. Serre, in *Ordered Porous Solids*, Elsevier, **2009**, pp. 77; b) X. Wang, L. Ge, Q. Lu, J. Dai, D. Guan, R. Ran, S.-C. Weng, Z. Hu, W. Zhou, Z. Shao, *J. Power Sources* **2020**, *468*, 228377.
- [41] a) D. Zhao, J.-L. Shui, L. R. Grabstanowicz, C. Chen, S. M. Commet, T. Xu, J. Lu, D.-J. Liu, *Adv. Mater.* **2014**, *26*, 1093; b) Z.-S. Wu, L. Chen, J. Liu, K. Parvez, H. Liang, J. Shu, H. Sachdev, R. Graf, X. Feng, K. Müllen, *Adv. Mater.* **2014**, *26*, 1450.
- [42] a) H. Deng, C. J. Doonan, H. Furukawa, R. B. Ferreira, J. Towner, C. B. Knobler, B. Wang, O. M. Yaghi, *Science* **2010**, *327*, 846; b) M. O'Keeffe, O. M. Yaghi, *Chem. Rev.* **2012**, *112*, 675.

- [43] a) L. Jiao, Y. Wang, H.-L. Jiang, Q. Xu, *Adv. Mater.* **2018**, *30*, 1703663; b) M. Wu, K. Wang, M. Yi, Y. Tong, Y. Wang, S. Song, *ACS Catal.* **2017**, *7*, 6082; c) L. Ma, S. Chen, Z. Pei, Y. Huang, G. Liang, F. Mo, Q. Yang, J. Su, Y. Gao, J. A. Zapien, C. Zhi, *ACS Nano* **2018**, *12*, 1949; d) X. Sun, S. Sun, S. Gu, Z. Liang, J. Zhang, Y. Yang, Z. Deng, P. Wei, J. Peng, Y. Xu, C. Fang, Q. Li, J. Han, Z. Jiang, Y. Huang, *Nano Energy* **2019**, *61*, 245.
- [44] V. M. A. Melgar, J. Kim, M. R. Othman, *J. Ind. Eng. Chem.* **2015**, *28*, 1.
- [45] Y. Guan, J. Shi, M. Xia, J. Zhang, Z. Pang, A. Marchetti, X. Wang, J. Cai, X. Kong, *Appl. Surf. Sci.* **2017**, *423*, 349.
- [46] a) W. Niu, Y. Yang, *ACS Appl. Energy Mater.* **2018**, *1*, 2440; b) I. S. Amiin, X. Liu, Z. Pu, W. Li, Q. Li, J. Zhang, H. Tang, H. Zhang, S. Mu, *Adv. Funct. Mater.* **2018**, *28*, 1704638.
- [47] K. S. Park, Z. Ni, A. P. Côté, J. Y. Choi, R. Huang, F. J. Uribe-Romo, H. K. Chae, M. O’Keeffe, O. M. Yaghi, *Proceedings of the National Academy of Sciences* **2006**, *103*, 10186.
- [48] E. D. Miensah, M. M. Khan, J. Y. Chen, X. M. Zhang, P. Wang, Z. X. Zhang, Y. Jiao, Y. Liu, Y. Yang, *Crit. Rev. Env. Sci. Technol.* **2020**, *50*, 1874.
- [49] a) S. Dutta, Z. Liu, H. Han, A. Indra, T. Song, *ChemElectroChem* **2018**, *5*, 3571; b) P. Z. Moghadam, T. Islamoglu, S. Goswami, J. Exley, M. Fantham, C. F. Kaminski, R. Q. Snurr, O. K. Fafha, D. Fairen-Jimenez, *Nat. Commun.* **2018**, *9*, 1; c) W. Lu, Z. Wei, Z.-Y. Gu, T.-F. Liu, J. Park, J. Park, J. Tian, M. Zhang, Q. Zhang, T. Gentle III, *Chem. Soc. Rev.* **2014**, *43*, 5561.
- [50] H. Furukawa, K. E. Cordova, M. O’Keeffe, O. M. Yaghi, *Science* **2013**, *341*.
- [51] K. Gong, F. Du, Z. Xia, M. Durstock, L. Dai, *Science* **2009**, *323*, 760.
- [52] H. B. Yang, J. Miao, S.-F. Hung, J. Chen, H. B. Tao, X. Wang, L. Zhang, R. Chen, J. Gao, H. M. Chen, *Sci. Adv.* **2016**, *2*, e1501122.
- [53] Y. Liu, Y. Shen, L. Sun, J. Li, C. Liu, W. Ren, F. Li, L. Gao, J. Chen, F. Liu, *Nat. Commun.* **2016**, *7*, 1.
- [54] D. Yu, Q. Qian, L. Wei, W. Jiang, K. Goh, J. Wei, J. Zhang, Y. Chen, *Chem. Soc. Rev.* **2015**, *44*, 647.
- [55] C. Tang, H. F. Wang, X. Chen, B. Q. Li, T. Z. Hou, B. Zhang, Q. Zhang, M. M. Titirici, F. Wei, *Adv. Mater.* **2016**, *28*, 6845.
- [56] a) S. Han, X. Hu, J. Wang, X. Fang, Y. Zhu, *Adv. Energy Mater.* **2018**, *8*, 1800955; b) L. Kong, J. Zhu, W. Shuang, X. H. Bu, *Adv. Energy Mater.* **2018**, *8*, 1801515; c) L. Lai, J. R. Potts, D. Zhan, L. Wang, C. K. Poh, C. Tang, H. Gong, Z. Shen, J. Lin, R. S. Ruoff, *Energy Environ. Sci.* **2012**, *5*, 7936; d) H. Jiang, J. Gu, X. Zheng, M. Liu, X. Qiu, L. Wang, W. Li, Z. Chen, X. Ji, J. Li, *Energy Environ. Sci.* **2019**, *12*, 322; e) H. B. Yang, J. Miao, S.-F. Hung, J. Chen, H. B. Tao, X. Wang, L. Zhang, R. Chen, J. Gao, H. M. Chen, L. Dai, B. Liu, *Sci. Adv.* **2016**, *2*, e1501122; f) D. Guo, R. Shibuya, C. Akiba, S. Saji, T. Kondo, J. Nakamura, *Science* **2016**, *351*, 361.
- [57] a) L. Zhang, Z. Su, F. Jiang, L. Yang, J. Qian, Y. Zhou, W. Li, M. Hong, *Nanoscale* **2014**, *6*, 6590; b) Y. Li, Z. Yan, Q. Wang, H. Ye, M. Li, L. Zhu, X. Cao, *Electrochim. Acta* **2018**, *282*, 224.
- [58] a) I. S. Amiin, Z. Pu, X. Liu, K. A. Owusu, H. G. R. Monestel, F. O. Boakye, H. Zhang, S. Mu, *Adv. Funct. Mater.* **2017**, *27*, 1702300; b) I. S. Amiin, Z. Pu, X. Liu, K. A. Owusu, H. G. R. Monestel, F. O. Boakye, H. Zhang, S. Mu, *Adv. Funct. Mater.* **2017**, *27*, 1702300.
- [59] J. Tang, R. R. Salunkhe, J. Liu, N. L. Torad, M. Imura, S. Furukawa, Y. Yamauchi, *J. Am. Chem. Soc.* **2015**, *137*, 1572.
- [60] a) J. C. Tan, T. D. Bennett, A. K. Cheetham, M. L. Klein, *Proceedings of the National Academy of Sciences of the United States of America* **2010**, *107*, 9938; b) Y. Q. Tian, Y. M. Zhao, Z. X. Chen, G. N. Zhang, L. H. Weng, D. Y. Zhao, *Chem. Eur. J.* **2007**, *13*, 4146; c) X. Deng, S. Zhu, J. Li, F. He, E. Liu, C. He, C. Shi, Q. Li, L. Ma, N. Zhao, *Carbon* **2019**, *143*, 728; d) A. Phan, C. J. Doonan, F. J. Uribe-Romo, C. B. Knobler, M. O’Keeffe, O. M. Yaghi, *Acc. Chem. Res.* **2010**, *43*, 58.
- [61] J. Zhang, Y. Tan, W.-J. Song, *Microchimica Acta* **2020**, *187*, 234.
- [62] a) J. Liu, D. Zhu, C. Guo, A. Vasileff, S.-Z. Qiao, *Adv. Energy Mater.* **2017**, *7*, 1700518; b) Y. Zhang, R. Zhu, Y. Cui, J. Zhong, X. Zhang, J. Chen, *Nanotechnology* **2014**, *25*, 135607; c)

- K. S. Park, Z. Ni, A. P. Côté, J. Y. Choi, R. Huang, F. J. Uribe-Romo, H. K. Chae, M. O'Keeffe, O. M. Yaghi, *Proc Natl Acad Sci U S A* **2006**, *103*, 10186.
- [63] a) A. Phan, C. J. Doonan, F. Uribe-Romo, C. B. Knobler, *Acc. Chem. Res* **2010**, *43*, 58; b) B. Wang, A. P. Côté, H. Furukawa, M. O'Keeffe, O. M. Yaghi, *Nature* **2008**, *453*, 207.
- [64] R. Banerjee, H. Furukawa, D. Britt, C. Knobler, M. O'Keeffe, O. M. Yaghi, *J. Am. Chem. Soc.* **2009**, *131*, 3875.
- [65] G. Zhong, D. Liu, J. Zhang, *J. Mater. Chem. A* **2018**, *6*, 1887.
- [66] A. Aijaz, N. Fujiwara, Q. Xu, *J. Am. Chem. Soc.* **2014**, *136*, 6790.
- [67] a) J. Meng, C. Niu, L. Xu, J. Li, X. Liu, X. Wang, Y. Wu, X. Xu, W. Chen, Q. Li, Z. Zhu, D. Zhao, L. Mai, *Journal of the American Chemical Society* **2017**, *139*, 8212; b) Y. Arafat, M. R. Azhar, Y. Zhong, X. Xu, M. O. Tadé, Z. Shao, *Nanomicro Lett.* **2020**, *12*, 130; c) A. Bähr, G.-h. Moon, H. Tüysüz, *ACS Appl. Energy Mater.* **2019**, *2*, 6672.
- [68] a) Z. Pei, H. Li, Y. Huang, Q. Xue, Y. Huang, M. Zhu, Z. Wang, C. Zhi, *Energy & Environmental Science* **2017**, *10*, 742; b) H.-W. Liang, W. Wei, Z.-S. Wu, X. Feng, K. Müllen, *Journal of the American Chemical Society* **2013**, *135*, 16002.
- [69] a) S. Bhattacharyya, B. Konkena, K. Jayaramulu, W. Schuhmann, T. K. Maji, *J. Mater. Chem. A* **2017**, *5*, 13573; b) X. Li, Q. Jiang, S. Dou, L. Deng, J. Huo, S. Wang, *J. Mater. Chem. A* **2016**, *4*, 15836.
- [70] Y. V. Kaneti, S. Dutta, M. S. A. Hossain, M. J. A. Shiddiky, K.-L. Tung, F.-K. Shieh, C.-K. Tsung, K. C.-W. Wu, Y. Yamauchi, *Adv. Mater.* **2017**, *29*, 1700213.
- [71] J. Xue, Y. Li, J. Hu, *J. Mater. Chem. A* **2020**, *8*, 7145.
- [72] a) Y. Chen, S. Ji, Y. Wang, J. Dong, W. Chen, Z. Li, R. Shen, L. Zheng, Z. Zhuang, D. Wang, Y. Li, *Angew. Chem. Int. Ed.* **2017**, *56*, 6937; b) J. Wang, Z. Huang, W. Liu, C. Chang, H. Tang, Z. Li, W. Chen, C. Jia, T. Yao, S. Wei, *J. Am. Chem. Soc.* **2017**, *139*, 17281.
- [73] L. Liu, W. Yang, D. Gu, X. Zhao, Q. Pan, *Front. Chem.* **2019**, *7*, 607.
- [74] L. Yang, X. Zeng, W. Wang, D. Cao, *Adv. Funct. Mater.* **2018**, *28*, 1704537.
- [75] X. Cao, C. Tan, M. Sindoro, H. Zhang, *Chem. Soc. Rev.* **2017**, *46*, 2660.
- [76] E. Zhang, Y. Xie, S. Ci, J. Jia, P. Cai, L. Yi, Z. Wen, *J. Mater. Chem. A* **2016**, *4*, 17288.
- [77] a) S. Bhattacharjee, M.-S. Jang, H.-J. Kwon, W.-S. Ahn, *Catal. Surv. from Asia* **2014**, *18*, 101; b) B. Chen, Z. Yang, Y. Zhu, Y. Xia, *J. Mater. Chem. A* **2014**, *2*, 16811; c) L. Zhou, X. Deng, Q. Lu, G. Yang, W. Zhou, Z. Shao, *Energy Fuels* **2020**, *34*, 11527.
- [78] L. Wang, Y. Guan, X. Qiu, H. Zhu, S. Pan, M. Yu, Q. Zhang, *Chem. Eng. J.* **2017**, *326*, 945.
- [79] a) B. You, N. Jiang, M. Sheng, W. S. Drisdell, J. Yano, Y. Sun, *ACS Catal.* **2015**, *5*, 7068; b) Y.-Z. Chen, C. Wang, Z.-Y. Wu, Y. Xiong, Q. Xu, S.-H. Yu, H.-L. Jiang, *Adv. Mater.* **2015**, *27*, 5010.
- [80] a) X. Chen, K. Shen, J. Chen, B. Huang, D. Ding, L. Zhang, Y. Li, *Chem. Eng. J.* **2017**, *330*, 736; b) S. S. A. Shah, L. Peng, T. Najam, C. Cheng, G. Wu, Y. Nie, W. Ding, X. Qi, S. Chen, Z. Wei, *Electrochim. Acta* **2017**, *251*, 498; c) P. Yin, T. Yao, Y. Wu, L. Zheng, Y. Lin, W. Liu, H. Ju, J. Zhu, X. Hong, Z. Deng, G. Zhou, S. Wei, Y. Li, *Angew. Chem. Int. Ed.* **2016**, *55*, 10800.
- [81] J. Wu, L. Hu, N. Wang, Y. Li, D. Zhao, L. Li, X. Peng, Z. Cui, L.-J. Ma, Y. Tian, X. Wang, *Applied Catalysis B: Environmental* **2019**, *254*, 55.
- [82] H. Wei, K. Huang, D. Wang, R. Zhang, B. Ge, J. Ma, B. Wen, S. Zhang, Q. Li, M. Lei, C. Zhang, J. Irawan, L.-M. Liu, H. Wu, *Nat. Commun.* **2017**, *8*, 1490.
- [83] Y. Guan, Y. Li, S. Luo, X. Ren, L. Deng, L. Sun, H. Mi, P. Zhang, J. Liu, *Appl. Catal. B* **2019**, *256*, 117871.
- [84] D. Chen, J. Yu, Z. Cui, Q. Zhang, X. Chen, J. Sui, H. Dong, L. Yu, L. Dong, *Electrochim. Acta* **2020**, *331*, 135394.
- [85] J.-J. Cai, Q.-Y. Zhou, B. Liu, X.-F. Gong, Y.-L. Zhang, K. Goh, D.-M. Gu, L. Zhao, X.-L. Sui, Z.-B. Wang, *Nanoscale* **2020**, *12*, 973.
- [86] D. Chen, J. Ji, Z. Jiang, M. Ling, Z. Jiang, X. Peng, *J. Power Sources* **2020**, *450*, 227660.
- [87] J. Li, Y. Kang, D. Liu, Z. Lei, P. Liu, *ACS Appl. Mater. Interfaces* **2020**, *12*, 5717.
- [88] M. Huo, B. Wang, C. Zhang, S. Ding, H. Yuan, Z. Liang, J. Qi, M. Chen, Y. Xu, W. Zhang, H. Zheng, R. Cao, *Chem. Eur. J.* **2019**, *25*, 12780.

- [89] S. H. Ahn, A. Manthiram, *Small* **2017**, *13*, 1702068.
- [90] L. Feng, R. Ding, Y. Chen, J. Wang, L. Xu, *J. Power Sources* **2020**, *452*, 227837.
- [91] H. Zhang, Z. Yang, X. Wang, S. Yan, T. Zhou, C. Zhang, S. G. Telfer, S. Liu, *Nanoscale* **2019**, *11*, 17384.
- [92] T. Meng, J. Qin, S. Wang, D. Zhao, B. Mao, M. Cao, *J. Mater. Chem. A* **2017**, *5*, 7001.
- [93] Y. Chong, Z. Pan, M. Su, X. Yang, D. Ye, Y. Qiu, *Electrochim. Acta* **2020**, *363*, 137264.
- [94] C. Guan, A. Sumboja, H. Wu, W. Ren, X. Liu, H. Zhang, Z. Liu, C. Cheng, S. J. Pennycook, J. Wang, *Adv. Mater.* **2017**, *29*, 1704117.
- [95] Y. Jiang, Y. P. Deng, J. Fu, D. U. Lee, R. Liang, Z. P. Cano, Y. Liu, Z. Bai, S. Hwang, L. Yang, *Adv. Energy Mater.* **2018**, *8*, 1702900.
- [96] Z. Wang, H. Jin, T. Meng, K. Liao, W. Meng, J. Yang, D. He, Y. Xiong, S. Mu, *Adv. Funct. Mater.* **2018**, *28*, 1802596.
- [97] T. Wang, Z. Kou, S. Mu, J. Liu, D. He, I. S. Amiinu, W. Meng, K. Zhou, Z. Luo, S. Chaemchuen, F. Verpoort, *Adv. Funct. Mater.* **2018**, *28*, 1705048.
- [98] X. Zhang, X. Han, Z. Jiang, J. Xu, L. Chen, Y. Xue, A. Nie, Z. Xie, Q. Kuang, L. Zheng, *Nano Energy* **2020**, *71*, 104547.
- [99] W. Zang, A. Sumboja, Y. Ma, H. Zhang, Y. Wu, S. Wu, H. Wu, Z. Liu, C. Guan, J. Wang, S. J. Pennycook, *ACS Catal.* **2018**, *8*, 8961.
- [100] Y. Chen, S. Ji, S. Zhao, W. Chen, J. Dong, W.-C. Cheong, R. Shen, X. Wen, L. Zheng, A. I. Rykov, S. Cai, H. Tang, Z. Zhuang, C. Chen, Q. Peng, D. Wang, Y. Li, *Nat. Commun.* **2018**, *9*, 5422.
- [101] J. Han, X. Meng, L. Lu, J. Bian, Z. Li, C. Sun, *Adv. Funct. Mater.* **2019**, *29*, 1808872.
- [102] W. Wei, X. Shi, P. Gao, S. Wang, W. Hu, X. Zhao, Y. Ni, X. Xu, Y. Xu, W. Yan, H. Ji, M. Cao, *Nano Energy* **2018**, *52*, 29.
- [103] D. Ji, L. Fan, L. Li, S. Peng, D. Yu, J. Song, S. Ramakrishna, S. Guo, *Adv. Mater.* **2019**, *31*, 1808267.
- [104] J. Wu, H. Zhou, Q. Li, M. Chen, J. Wan, N. Zhang, L. Xiong, S. Li, B. Y. Xia, G. Feng, M. Liu, L. Huang, *Adv. Energy Mater.* **2019**, *9*, 1900149.
- [105] L. Zhou, P. Zhou, Y. Zhang, B. Liu, P. Gao, S. Guo, *J. Energy Chem.* **2021**, *55*, 355.
- [106] J. Deng, P. Ren, D. Deng, X. Bao, *Angew. Chem. Int. Ed.* **2015**, *54*, 2100.
- [107] M. Wang, T. Qian, J. Zhou, C. Yan, *ACS Appl. Mater. Interfaces* **2017**, *9*, 5213.
- [108] Y.-N. Chen, Y. Guo, H. Cui, Z. Xie, X. Zhang, J. Wei, Z. Zhou, *J. Mater. Chem. A* **2018**, *6*, 9716.
- [109] X. Song, S. Chen, L. Guo, Y. Sun, X. Li, X. Cao, Z. Wang, J. Sun, C. Lin, Y. Wang, *Adv. Energy Mater.* **2018**, *8*, 1801101.
- [110] H. Ge, G. Li, J. Shen, W. Ma, X. Meng, L. Xu, *Appl. Catal. B* **2020**, *275*, 119104.
- [111] Q. Xu, H. Jiang, Y. Li, D. Liang, Y. Hu, C. Li, *Appl. Catal. B* **2019**, *256*, 117893.
- [112] H. Qi, Y. Feng, Z. Chi, Y. Cui, M. Wang, J. Liu, Z. Guo, L. Wang, S. Feng, *Nanoscale* **2019**, *11*, 21943.
- [113] F. Meng, H. Zhong, D. Bao, J. Yan, X. Zhang, *J. Am. Chem. Soc.* **2016**, *138*, 10226.
- [114] X. Yao, J. Li, Y. Zhu, L. Li, W. Zhang, *Compos. B. Eng.* **2020**, *193*, 108058.
- [115] B. Li, K. Igawa, J. Chai, Y. Chen, Y. Wang, D. W. Fam, N. N. Tham, T. An, T. Konno, A. Sng, Z. Liu, H. Zhang, Y. Zong, *Energy Stor. Mater.* **2020**, *25*, 137.
- [116] Y. Zhao, Q. Lai, J. Zhu, J. Zhong, Z. Tang, Y. Luo, Y. Liang, *Small* **2018**, *14*, 1704207.
- [117] Q. Li, J. Zhao, M. Wu, C. Li, L. Han, R. Liu, *ChemistrySelect* **2019**, *4*, 722.
- [118] J. Di, J. Guo, N. Wang, G. Ma, *ACS Sustain. Chem. Eng.* **2019**, *7*, 7716.
- [119] W. Zhang, X. Zhao, Y. Zhao, J. Zhang, X. Li, L. Fang, L. Li, *ACS Appl. Mater. Interfaces* **2020**, *12*, 10280.
- [120] J. Li, Y. Kang, W. Wei, X. Li, Z. Lei, P. Liu, *Chem. Eng. J.* **2021**, *407*, 127961.
- [121] B. Y. Guan, Y. Lu, Y. Wang, M. Wu, X. W. Lou, *Adv. Funct. Mater.* **2018**, *28*, 1706738.
- [122] M. Wu, B. Guo, A. Nie, R. Liu, *J. Colloid Interface Sci.* **2020**, *561*, 585.
- [123] Z. Wang, J. Ang, J. Liu, X. Y. D. Ma, J. Kong, Y. Zhang, T. Yan, X. Lu, *Appl. Catal. B* **2020**, *263*, 118344.
- [124] W. Xie, J. Li, Y. Song, S. Li, J. Li, M. Shao, *Nanomicro Lett.* **2020**, *12*, 97.

- [125] Y. Xiao, B. Guo, J. Zhang, C. Hu, R. Ma, D. Wang, J. Wang, *Dalton Trans.* **2020**, 49, 5730.
- [126] Q. Zhou, Z. Zhang, J. Cai, B. Liu, Y. Zhang, X. Gong, X. Sui, A. Yu, L. Zhao, Z. Wang, Z. Chen, *Nano Energy* **2020**, 71, 104592.
- [127] J. Li, S. Lu, H. Huang, D. Liu, Z. Zhuang, C. Zhong, *ACS Sustain. Chem. Eng.* **2018**, 6, 10021.
- [128] S. H. Ahn, X. Yu, A. Manthiram, *Adv. Mater.* **2017**, 29, 1606534.
- [129] Y. Yu, X. Peng, U. Ali, X. Liu, Y. Xing, S. Xing, *Inorg. Chem. Front.* **2019**, 6, 3255.
- [130] Y. Sun, Y. Guan, X. Wu, W. Li, Y. Li, L. Sun, H. Mi, Q. Zhang, C. He, X. Ren, *Nanoscale* **2021**, 13, 3227.
- [131] a) J.-T. Ren, G.-G. Yuan, C.-C. Weng, L. Chen, Z.-Y. Yuan, *ChemCatChem* **2018**, 10, 5297; b) T.-Y. Ma, L. Liu, Z.-Y. Yuan, *Chem. Soc. Rev.* **2013**, 42, 3977; c) Y. Meng, D. Voiry, A. Goswami, X. Zou, X. Huang, M. Chhowalla, Z. Liu, T. Asefa, *J. Am. Chem. Soc.* **2014**, 136, 13554; d) J.-T. Ren, Z.-Y. Yuan, *ChemCatChem* **2018**, 10, 3260; e) Q. Lu, J. Yu, X. Zou, K. Liao, P. Tan, W. Zhou, M. Ni, Z. Shao, *Adv. Funct. Mater.* **2019**, 29, 1904481.
- [132] a) Y. P. Zhu, Y. Jing, A. Vasileff, T. Heine, S.-Z. Qiao, *Adv. Energy Mater.* **2017**, 7, 1602928; b) W. Wei, H. Liang, K. Parvez, X. Zhuang, X. Feng, K. Müllen, *Angew. Chem. Int. Ed.* **2014**, 53, 1570.
- [133] Y. Li, H. Xu, H. Huang, L. Gao, Y. Zhao, T. Ma, *Electrochim. Acta* **2017**, 254, 148.
- [134] a) M. Jiang, X. Cao, D. Zhu, Y. Duan, J. Zhang, *Electrochimica Acta* **2016**, 196, 699; b) Y. Li, L. Li, L. Zhu, L. Gu, X. Cao, *Chemical Communications* **2016**, 52, 5520; c) Q. Lai, Y. Zhao, Y. Liang, J. He, J. Chen, *Adv. Funct. Mater.* **2016**, 26, 8334.
- [135] a) R. Li, Z. Wei, X. Gou, *ACS Catal.* **2015**, 5, 4133; b) H. Kim, K. Lee, S. I. Woo, Y. Jung, *Phys. Chem. Chem. Phys.* **2011**, 13, 17505.
- [136] a) Y. Zhao, L. Yang, S. Chen, X. Wang, Y. Ma, Q. Wu, Y. Jiang, W. Qian, Z. Hu, *J. Am. Chem. Soc.* **2013**, 135, 1201; b) F. Hou, Y. Li, Y. Gao, S. Hu, B. Wu, H. Bao, H. Wang, B. Jiang, *Mater. Res. Bull.* **2019**, 110, 18.
- [137] a) T. Y. Ma, J. Ran, S. Dai, M. Jaroniec, S. Z. Qiao, *Angew. Chem. Int. Ed.* **2015**, 54, 4646; b) J. Zhang, Z. Zhao, Z. Xia, L. Dai, *Nature Nanotechnology* **2015**, 10, 444.
- [138] Y. Li, H. Zhang, Y. Wang, P. Liu, H. Yang, X. Yao, D. Wang, Z. Tang, H. Zhao, *Energy Environ. Sci.* **2014**, 7, 3720.
- [139] Z. Yao, H. Nie, Z. Yang, X. Zhou, Z. Liu, S. Huang, *Chemical Communications* **2012**, 48, 1027.
- [140] Q. Ju, R. Ma, Y. Pei, B. Guo, Q. Liu, T. Zhang, M. Yang, J. Wang, *Mater. Res. Bull.* **2020**, 125, 110770.
- [141] D. Yu, Y. Xue, L. Dai, *J. Phys. Chem. Lett.* **2012**, 3, 2863.
- [142] J. Zhang, Z. Zhao, Z. Xia, L. Dai, *Nat. Nanotechnol.* **2015**, 10, 444.
- [143] Y. Qian, Z. Hu, X. Ge, S. Yang, Y. Peng, Z. Kang, Z. Liu, J. Y. Lee, D. Zhao, *Carbon* **2017**, 111, 641.
- [144] a) J.-K. Sun, Q. Xu, *Chem. Commun.* **2014**, 50, 13502; b) J. Li, Q.-L. Zhu, Q. Xu, *Chem. Commun.* **2015**, 51, 10827; c) S. Dutta, A. Bhaumik, K. C. W. Wu, *Energy Environ. Sci.* **2014**, 7, 3574; d) K. Mi, Y. Jiang, J. Feng, Y. Qian, S. Xiong, *Adv. Funct. Mater.* **2016**, 26, 1571; e) L. Estevez, R. Dua, N. Bhandari, A. Ramanujapuram, P. Wang, E. P. Giannelis, *Energy Environ. Sci.* **2013**, 6, 1785.
- [145] S. H. Ahn, M. J. Klein, A. Manthiram, *Adv. Energy Mater.* **2017**, 7, 1601979.
- [146] a) Y. Qian, T. An, K. E. Birgersson, Z. Liu, D. Zhao, *Small* **2018**, 14, 1704169; b) Y. Wang, L. Tao, Z. Xiao, R. Chen, Z. Jiang, S. Wang, *Adv. Funct. Mater.* **2018**, 28, 1705356.
- [147] X. Zheng, X. Cao, Z. Sun, K. Zeng, J. Yan, P. Strasser, X. Chen, S. Sun, R. Yang, *Appl. Catal. B* **2020**, 118967.
- [148] J. Yan, X. Zheng, C. Wei, Z. Sun, K. Zeng, L. Shen, J. Sun, M. H. Rummeli, R. Yang, *Carbon* **2021**, 171, 320.
- [149] Q. Lai, Y. Zhao, Y. Liang, J. He, J. Chen, *Adv. Funct. Mater.* **2016**, 26, 8334.

- [150] a) M. Liu, J. Li, *ACS Appl. Mater. Interfaces* **2016**, *8*, 2158; b) L. Shang, H. Yu, X. Huang, T. Bian, R. Shi, Y. Zhao, G. I. Waterhouse, L. Z. Wu, C. H. Tung, T. Zhang, *Adv. Mater.* **2016**, *28*, 1668.
- [151] C. Xuan, B. Hou, W. Xia, Z. Peng, T. Shen, H. L. Xin, G. Zhang, D. Wang, *J. Mater. Chem. A* **2018**, *6*, 10731.
- [152] a) G. Fu, Z. Cui, Y. Chen, Y. Li, Y. Tang, J. B. Goodenough, *Adv. Energy Mater.* **2017**, *7*, 1601172; b) W. Wang, W. Chen, P. Miao, J. Luo, Z. Wei, S. Chen, *ACS Catal.* **2017**, *7*, 6144; c) L.-X. Zuo, W.-J. Wang, R.-B. Song, J.-J. Lv, L.-P. Jiang, J.-J. Zhu, *ACS Sustain. Chem. Eng.* **2017**, *5*, 10275.
- [153] K. Mamtani, D. Jain, D. Dogu, V. Gustin, S. Gunduz, A. C. Co, U. S. Ozkan, *Appl. Catal. B* **2018**, *220*, 88.
- [154] M. Yang, X. Hu, Z. Fang, L. Sun, Z. Yuan, S. Wang, W. Hong, X. Chen, D. Yu, *Adv. Funct. Mater.* **2017**, *27*, 1701971.
- [155] a) Q. Shi, S. Fu, C. Zhu, J. Song, D. Du, Y. Lin, *Materials Horizons* **2019**; b) S. Liu, Z. Wang, S. Zhou, F. Yu, M. Yu, C.-Y. Chiang, W. Zhou, J. Zhao, J. Qiu, *Adv. Mater.* **2017**, *29*, 1700874.
- [156] a) S. Dou, X. Li, L. Tao, J. Huo, S. Wang, *Chem. Commun.* **2016**, *52*, 9727; b) S. Wang, J. Qin, T. Meng, M. Cao, *Nano Energy* **2017**, *39*, 626; c) H. B. Aiyappa, S. N. Bhange, V. P. Sivasankaran, S. Kurungot, *ChemElectroChem* **2017**, *4*, 2928; d) Z. Li, M. Shao, Q. Yang, Y. Tang, M. Wei, D. G. Evans, X. Duan, *Nano Energy* **2017**, *37*, 98.
- [157] a) Z. Zhu, C. Chen, M. Cai, Y. Cai, H. Ju, S. Hu, M. Zhang, *Mater. Res. Bull.* **2019**, *114*, 161; b) J. Guo, S. Gadipelli, Y. Yang, Z. Li, Y. Lu, D. J. Brett, Z. Guo, *J. Mater. Chem. A* **2019**, *7*, 3544; c) B. Ni, C. Ouyang, X. Xu, J. Zhuang, X. Wang, *Adv. Mater.* **2017**, *29*, 1701354.
- [158] J.-C. Li, X.-T. Wu, L.-J. Chen, N. Li, Z.-Q. Liu, *Energy* **2018**, *156*, 95.
- [159] B. Y. Xia, Y. Yan, N. Li, H. B. Wu, X. W. Lou, X. Wang, *Nature Energy* **2016**, *1*, 15006.
- [160] Y. Jiang, H. Liu, X. Tan, L. Guo, J. Zhang, S. Liu, Y. Guo, J. Zhang, H. Wang, W. Chu, *ACS Appl. Mater. Interfaces* **2017**, *9*, 25239.
- [161] X. Xu, J. Tang, H. Qian, S. Hou, Y. Bando, M. S. A. Hossain, L. Pan, Y. Yamauchi, *ACS Appl. Mater. Interfaces* **2017**, *9*, 38737.
- [162] Y. Pan, D. Heryadi, F. Zhou, L. Zhao, G. Lestari, H. Su, Z. Lai, *CrystEngComm* **2011**, *13*, 6937.
- [163] Z. Liang, C. Zhang, H. Yuan, W. Zhang, H. Zheng, R. Cao, *Chem. Commun.* **2018**, *54*, 7519.
- [164] a) G. Jia, W. Zhang, G. Fan, Z. Li, D. Fu, W. Hao, C. Yuan, Z. Zou, *Angew. Chem. Int. Ed.* **2017**, *56*, 13781; b) J. Deng, P. Ren, D. Deng, L. Yu, F. Yang, X. Bao, *Energy Environ. Sci.* **2014**, *7*, 1919; c) W.-J. Jiang, L. Gu, L. Li, Y. Zhang, X. Zhang, L.-J. Zhang, J.-Q. Wang, J.-S. Hu, Z. Wei, L.-J. Wan, *J. Am. Chem. Soc.* **2016**, *138*, 3570.
- [165] Y.-N. Hou, Z. Zhao, Z. Yu, Y. Tang, X. Wang, J. Qiu, *Chem. Commun.* **2017**, *53*, 7840.
- [166] a) C. Guo, Y. Zhang, Y. Guo, L. Zhang, Y. Zhang, J. Wang, *Chem. Commun.* **2018**, *54*, 252; b) V. Armel, J. Hannauer, F. Jaouen, *Catalysts* **2015**, *5*, 1333; c) T. Rodenas, I. Luz, G. Prieto, B. Seoane, H. Miro, A. Corma, F. Kapteijn, F. X. L. i Xamena, J. Gascon, *Nat. Mater.* **2015**, *14*, 48.
- [167] a) W. Gu, M. Wu, J. Sun, J. Xu, T. Zhao, *J. Mater. Chem. A* **2019**, *7*, 20132; b) W. Wang, Q. Jia, S. Mukerjee, S. Chen, *ACS Catal.* **2019**, *9*, 10126.
- [168] a) Y. Li, T. Liu, W. Yang, Z. Zhu, Y. Zhai, W. Gu, C. Zhu, *Nanoscale* **2019**, *11*, 19506; b) Y. Mun, S. Lee, K. Kim, S. Kim, S. Lee, J. W. Han, J. Lee, *J. Am. Chem. Soc.* **2019**, *141*, 6254; c) Y. Wang, J. Wang, D. Wei, M. Li, *ACS Appl. Mater. Interfaces* **2019**, *11*, 35755.
- [169] Y. Deng, X. Tian, B. Chi, Q. Wang, W. Ni, Y. Gao, Z. Liu, J. Luo, C. Lin, L. Ling, F. Cheng, Y. Zhang, S. Liao, S. Zhang, *Chem. Eng. J.* **2020**, *390*, 124479.
- [170] X.-L. Chen, L.-S. Ma, W.-Y. Su, L.-F. Ding, H.-B. Zhu, H. Yang, *Electrochim. Acta* **2020**, *331*, 135273.
- [171] J. K. Nørskov, J. Rossmeisl, A. Logadottir, L. Lindqvist, J. R. Kitchin, T. Bligaard, H. Jónsson, *The Journal of Physical Chemistry B* **2004**, *108*, 17886.
- [172] S. H. Noh, M. H. Seo, X. Ye, Y. Makinose, T. Okajima, N. Matsushita, B. Han, T. Ohsaka, *J. Mater. Chem. A* **2015**, *3*, 22031.

- [173] H. Yu, A. Fisher, D. Cheng, D. Cao, *ACS Appl. Mater. Interfaces* **2016**, *8*, 21431.
- [174] Q. Lai, J. Zhu, Y. Zhao, Y. Liang, J. He, J. Chen, *Small* **2017**, *13*, 1700740.
- [175] C. Zhang, H. Yang, D. Zhong, Y. Xu, Y. Wang, Q. Yuan, Z. Liang, B. Wang, W. Zhang, H. Zheng, T. Cheng, R. Cao, *J. Mater. Chem. A* **2020**, *8*, 9536.
- [176] a) A. M. El - Sawy, I. M. Mosa, D. Su, C. J. Guild, S. Khalid, R. Joesten, J. F. Rusling, S. L. Suib, *Adv. Energy Mater.* **2016**, *6*, 1501966; b) Z. Ma, S. Dou, A. Shen, L. Tao, L. Dai, S. Wang, *Angew. Chem. Int. Ed.* **2015**, *54*, 1888; c) K. P. Singh, E. J. Bae, J.-S. Yu, *J. Am. Chem. Soc.* **2015**, *137*, 3165; d) L. Yang, S. Jiang, Y. Zhao, L. Zhu, S. Chen, X. Wang, Q. Wu, J. Ma, Y. Ma, Z. Hu, *Angew. Chem. Int. Ed.* **2011**, *50*, 7132.
- [177] a) N. Cheng, L. Ren, X. Xu, Y. Du, S. X. Dou, *Adv. Energy Mater.* **2018**, *8*, 1801257; b) B. Y. Guan, L. Yu, X. W. D. Lou, *Energy Environ. Sci.* **2016**, *9*, 3092; c) G. Li, S. Zhao, Y. Zhang, Z. Tang, *Adv. Mater.* **2018**, *30*, 1800702; d) A. Indra, T. Song, U. Paik, *Adv. Mater.* **2018**, *30*, 1705146.
- [178] a) Y. Li, B. Jia, Y. Fan, K. Zhu, G. Li, C.-Y. Su, *Adv. Energy Mater.* **2018**, *8*, 1702048; b) S. Liu, X. Zhang, G. Wang, Y. Zhang, H. Zhang, *ACS Appl. Mater. Interfaces* **2017**, *9*, 34269; c) W. Luo, B. Wang, C. G. Heron, M. J. Allen, J. Morre, C. S. Maier, W. F. Stickle, X. Ji, *Nano Lett.* **2014**, *14*, 2225.
- [179] X. Li, Q. Jiang, S. Dou, L. Deng, J. Huo, S. Wang, *J. Mater. Chem. A* **2016**, *4*, 15836.
- [180] S. Dilpazir, R. Liu, M. Yuan, M. Imran, Z. Liu, Y. Xie, H. Zhao, G. Zhang, *J. Mater. Chem. A* **2020**, *8*, 10865.
- [181] X. Sun, Q. Gong, Y. Liang, M. Wu, N. Xu, P. Gong, S. Sun, J. Qiao, *ACS Appl. Mater. Interfaces* **2020**, *12*, 38202.
- [182] L. Wen, Y. Sun, C. Zhang, J. Yu, X. Li, X. Lyu, W. Cai, Y. Li, *ACS Appl. Energy Mater.* **2018**, *1*, 3835.
- [183] H. Zheng, X. Huang, H. Gao, G. Lu, A. Li, W. Dong, G. Wang, *Appl. Surf. Sci.* **2019**, *479*, 1254.
- [184] D. Jiang, W. Ma, Y. Zhou, Y. Xing, B. Quan, D. Li, *J. Colloid Interface Sci.* **2019**, *550*, 10.
- [185] a) M. Y. Zu, P. F. Liu, C. Wang, Y. Wang, L. R. Zheng, B. Zhang, H. Zhao, H. G. Yang, *ACS Energy Lett.* **2018**, *3*, 78; b) X. Ma, H. Meng, M. Cai, P. K. Shen, *J. Am. Chem. Soc.* **2012**, *134*, 1954.
- [186] X. Duan, S. Ren, N. Pan, M. Zhang, H. Zheng, *J. Mater. Chem. A* **2020**, *8*, 9355.
- [187] A. Pendashteh, S. M. F. Vilela, I. Krivtsov, D. Ávila-Brandé, J. Palma, P. Horcajada, R. Marcilla, *J. Power Sources* **2019**, *427*, 299.
- [188] C. Lai, X. Liu, Y. Wang, C. Cao, Y. Yin, B. Wu, X. Liu, S. Yang, T. Liang, *J. Power Sources* **2020**, *472*, 228470.
- [189] P. C. Vesborg, T. F. Jaramillo, *RSC Adv.* **2012**, *2*, 7933.
- [190] R. Nandan, K. Nanda, *J. Mater. Chem. A* **2017**, *5*, 16843.
- [191] X. Li, H. Rong, J. Zhang, D. Wang, Y. Li, *Nano Res.* **2020**, *13*, 1842.
- [192] a) P. He, X. Y. Yu, X. W. Lou, *Angew. Chem. Int. Ed.* **2017**, *56*, 3897; b) H. Fei, J. Dong, Y. Feng, C. S. Allen, C. Wan, B. Voloskiy, M. Li, Z. Zhao, Y. Wang, H. Sun, *Nat. Catal.* **2018**, *1*, 63; c) L. Zhang, Y. Jia, G. Gao, X. Yan, N. Chen, J. Chen, M. T. Soo, B. Wood, D. Yang, A. Du, *Chem* **2018**, *4*, 285; d) C. Zhu, S. Fu, Q. Shi, D. Du, Y. Lin, *Angew. Chem. Int. Ed.* **2017**, *56*, 13944.
- [193] a) P. Liu, Y. Zhao, R. Qin, S. Mo, G. Chen, L. Gu, D. M. Chevrier, P. Zhang, Q. Guo, D. Zang, B. Wu, G. Fu, N. Zheng, *Science* **2016**, *352*, 797; b) B. Y. Guan, L. Yu, X. W. Lou, *Adv. Sci.* **2017**, *4*, 1700247.
- [194] a) H. Fei, J. Dong, M. J. Arellano-Jiménez, G. Ye, N. Dong Kim, E. L. G. Samuel, Z. Peng, Z. Zhu, F. Qin, J. Bao, M. J. Yacaman, P. M. Ajayan, D. Chen, J. M. Tour, *Nat. Commun.* **2015**, *6*, 8668; b) H. Fei, J. Dong, Y. Feng, C. S. Allen, C. Wan, B. Voloskiy, M. Li, Z. Zhao, Y. Wang, H. Sun, P. An, W. Chen, Z. Guo, C. Lee, D. Chen, I. Shakir, M. Liu, T. Hu, Y. Li, A. I. Kirkland, X. Duan, Y. Huang, *Nat. Catal.* **2018**, *1*, 63; c) H. T. Chung, D. A. Cullen, D. Higgins, B. T. Sneed, E. F. Holby, K. L. More, P. Zelenay, *Science* **2017**, *357*, 479.

- [195] a) H.-W. Liang, X. Zhuang, S. Brüller, X. Feng, K. Müllen, *Nat. Commun.* **2014**, *5*, 1; b) J. Zhu, H. Zhou, C. Zhang, J. Zhang, S. Mu, *Nanoscale* **2017**, *9*, 13257.
- [196] a) Q. Liu, Y. Wang, L. Dai, J. Yao, *Adv. Mater.* **2016**, *28*, 3000; b) J. Fu, F. M. Hassan, J. Li, D. U. Lee, A. R. Ghannoum, G. Lui, M. A. Hoque, Z. Chen, *Adv. Mater.* **2016**, *28*, 6421; c) T.-Y. Ma, S. Dai, S. Z. Qiao, *Mater. Today* **2016**, *19*, 265.
- [197] a) Z. Li, D. Wang, Y. Wu, Y. Li, *Natl. Sci. Rev.* **2018**, *5*, 673; b) J. Zhang, Y. Zhao, X. Guo, C. Chen, C.-L. Dong, R.-S. Liu, C.-P. Han, Y. Li, Y. Gogotsi, G. Wang, *Nat. Catal.* **2018**, *1*, 985; c) Y. Qu, Z. Li, W. Chen, Y. Lin, T. Yuan, Z. Yang, C. Zhao, J. Wang, C. Zhao, X. Wang, F. Zhou, Z. Zhuang, Y. Wu, Y. Li, *Nat. Catal.* **2018**, *1*, 781; d) B. Qiao, A. Wang, X. Yang, L. F. Allard, Z. Jiang, Y. Cui, J. Liu, J. Li, T. Zhang, *Nat. Chem.* **2011**, *3*, 634; e) N. Cheng, S. Stambula, D. Wang, M. N. Banis, J. Liu, A. Riese, B. Xiao, R. Li, T.-K. Sham, L.-M. Liu, G. A. Botton, X. Sun, *Nat. Commun.* **2016**, *7*, 13638; f) D. A. Reed, B. K. Keitz, J. Oktawiec, J. A. Mason, T. Runčevski, D. J. Xiao, L. E. Darago, V. Crocellà, S. Bordiga, J. R. Long, *Nature* **2017**, *550*, 96.
- [198] R. Banerjee, A. Phan, B. Wang, C. Knobler, H. Furukawa, M. O'Keeffe, O. M. Yaghi, *Science* **2008**, *319*, 939.
- [199] S. Fu, C. Zhu, D. Su, J. Song, S. Yao, S. Feng, M. H. Engelhard, D. Du, Y. Lin, *Small* **2018**, *14*, 1703118.
- [200] a) C.-Y. Su, H. Cheng, W. Li, Z.-Q. Liu, N. Li, Z. Hou, F.-Q. Bai, H.-X. Zhang, T.-Y. Ma, *Adv. Energy Mater.* **2017**, *7*, 1602420; b) C. Li, M. Wu, R. Liu, *Appl. Catal. B* **2019**, *244*, 150; c) X. Liu, L. Wang, P. Yu, C. Tian, F. Sun, J. Ma, W. Li, H. Fu, *Angew. Chem. Int. Ed.* **2018**, *57*, 16166; d) G. Nam, Y. Son, S. O. Park, W. C. Jeon, H. Jang, J. Park, S. Chae, Y. Yoo, J. Ryu, M. G. Kim, *Adv. Mater.* **2018**, *30*, 1803372; e) W. Niu, S. Pakhira, K. Marcus, Z. Li, J. L. Mendoza - Cortes, Y. Yang, *Adv. Energy Mater.* **2018**, *8*, 1800480.
- [201] J. Zhu, M. Xiao, Y. Zhang, Z. Jin, Z. Peng, C. Liu, S. Chen, J. Ge, W. Xing, *ACS Catal.* **2016**, *6*, 6335.
- [202] N. A. Galote, F. E. R. Oliveira, F. H. B. Lima, *Appl. Catal. B* **2019**, *253*, 300.
- [203] a) J. Maruyama, N. Fukui, M. Kawaguchi, I. Abe, *J. Power Sources* **2008**, *182*, 489; b) J. Maruyama, I. Abe, *Chem. Commun.* **2007**, 2879.
- [204] Q. Lu, J. Yu, X. Zou, K. Liao, P. Tan, W. Zhou, M. Ni, Z. Shao, *Adv. Funct. Mater.* **2019**, *29*, 1904481.
- [205] a) F. M. Sapountzi, J. M. Gracia, C. J. Weststrate, H. O. A. Fredriksson, J. W. Niemantsverdriet, *Prog. Energy Combust. Sci.* **2017**, *58*, 1; b) Y. Xue, S. Sun, Q. Wang, Z. Dong, Z. Liu, *J. Mater. Chem. A* **2018**, *6*, 10595; c) M. Shao, Q. Chang, J.-P. Dodelet, R. Chenitz, *Chem. Rev.* **2016**, *116*, 3594.
- [206] Q. Zhao, X. Xu, Y. Jin, Q. Zhang, J. Liu, H. Wang, *J. Nanopart. Res.* **2020**, *22*, 299.
- [207] Y. Jiang, Y.-P. Deng, J. Fu, D. U. Lee, R. Liang, Z. P. Cano, Y. Liu, Z. Bai, S. Hwang, L. Yang, D. Su, W. Chu, Z. Chen, *Adv. Energy Mater.* **2018**, *8*, 1702900.
- [208] a) X. T. Wang, T. Ouyang, L. Wang, J. H. Zhong, T. Ma, Z. Q. Liu, *Angew. Chem.* **2019**, *131*, 13425; b) C. Xiao, X. Lu, C. Zhao, *Chem. Commun.* **2014**, *50*, 10122.
- [209] P. Chen, K. Xu, Z. Fang, Y. Tong, J. Wu, X. Lu, X. Peng, H. Ding, C. Wu, Y. Xie, *Angew. Chem. Int. Ed.* **2015**, *54*, 14710.
- [210] K. Xu, P. Chen, X. Li, Y. Tong, H. Ding, X. Wu, W. Chu, Z. Peng, C. Wu, Y. Xie, *J. Am. Chem. Soc.* **2015**, *137*, 4119.
- [211] Y. Wang, C. Xie, D. Liu, X. Huang, J. Huo, S. Wang, *ACS Appl. Mater. Interfaces* **2016**, *8*, 18652.
- [212] a) Y. Wang, D. Liu, Z. Liu, C. Xie, J. Huo, S. Wang, *Chem. Commun.* **2016**, *52*, 12614; b) B. Cao, G. M. Veith, R. E. Diaz, J. Liu, E. A. Stach, R. R. Adzic, P. G. Khalifah, *Angew. Chem. Int. Ed.* **2013**, *52*, 10753.
- [213] a) X. Jia, Y. Zhao, G. Chen, L. Shang, R. Shi, X. Kang, G. I. Waterhouse, L. Z. Wu, C. H. Tung, T. Zhang, *Adv. Energy Mater.* **2016**, *6*, 1502585; b) M. Jiang, Y. Li, Z. Lu, X. Sun, X. Duan, *Inorg. Chem. Front.* **2016**, *3*, 630.

- [214] a) M. Sun, D. Davenport, H. Liu, J. Qu, M. Elimelech, J. Li, *J. Mater. Chem. A* **2018**, *6*, 2527; b) C. Guo, Y. Li, W. Liao, Y. Liu, Z. Li, L. Sun, C. Chen, J. Zhang, Y. Si, L. Li, *J. Mater. Chem. A* **2018**, *6*, 13050.
- [215] a) S. Peng, F. Gong, L. Li, D. Yu, D. Ji, T. Zhang, Z. Hu, Z. Zhang, S. Chou, Y. Du, *J. Am. Chem. Soc.* **2018**, *140*, 13644; b) S. Peng, X. Han, L. Li, S. Chou, D. Ji, H. Huang, Y. Du, J. Liu, S. Ramakrishna, *Adv. Energy Mater.* **2018**, *8*, 1800612; c) Q. Wang, L. Shang, R. Shi, X. Zhang, G. I. Waterhouse, L.-Z. Wu, C.-H. Tung, T. Zhang, *Nano Energy* **2017**, *40*, 382.
- [216] a) L. Chen, Y. Zhang, X. Liu, L. Long, S. Wang, X. Xu, M. Liu, W. Yang, J. Jia, *Carbon* **2019**, *151*, 10; b) B. Zhang, C. Xiao, S. Xie, J. Liang, X. Chen, Y. Tang, *Chem. Mater.* **2016**, *28*, 6934; c) K. R. Yoon, K. Shin, J. Park, S.-H. Cho, C. Kim, J.-W. Jung, J. Y. Cheong, H. R. Byon, H. M. Lee, I.-D. Kim, *ACS nano* **2018**, *12*, 128.
- [217] H.-x. Zhong, K. Li, Q. Zhang, J. Wang, F.-l. Meng, Z.-j. Wu, J.-m. Yan, X.-b. Zhang, *NPG Asia Materials* **2016**, *8*, e308.
- [218] a) J. Zhao, N. Fu, R. Liu, *ACS Appl. Mater. Interfaces* **2018**, *10*, 28509; b) L. Yang, L. Shi, D. Wang, Y. Lv, D. Cao, *Nano Energy* **2018**, *50*, 691.
- [219] a) X. Zheng, Y. Cao, D. Liu, M. Cai, J. Ding, X. Liu, J. Wang, W. Hu, C. Zhong, *ACS Appl. Mater. Interfaces* **2019**, *11*, 15662; b) M. Jahan, Q. Bao, K. P. Loh, *J. Am. Chem. Soc.* **2012**, *134*, 6707; c) W. Zhang, X. Yao, S. Zhou, X. Li, L. Li, Z. Yu, L. Gu, *Small* **2018**, *14*, 1800423.
- [220] a) J. Shui, C. Chen, L. Grabstanowicz, D. Zhao, D.-J. Liu, *Proceedings of the National Academy of Sciences* **2015**, *112*, 10629; b) C. Liu, J. Wang, J. Li, J. Liu, C. Wang, X. Sun, J. Shen, W. Han, L. Wang, *J. Mater. Chem. A* **2017**, *5*, 1211.
- [221] X. Lu, C. Wang, Y. Wei, *Small* **2009**, *5*, 2349.
- [222] a) Q. Niu, J. Guo, B. Chen, J. Nie, X. Guo, G. Ma, *Carbon* **2017**, *114*, 250; b) J. Guo, B. Chen, Q. Hao, J. Nie, G. Ma, *Appl. Surf. Sci.* **2018**, *456*, 959.
- [223] a) C. Xiao, X. Chen, Y. Tang, *Nanotechnology* **2017**, *28*, 225401; b) T. Sun, B. Tian, J. Lu, C. Su, *J. Mater. Chem. A* **2017**, *5*, 18933; c) L. Cao, Z.-h. Li, Y. Gu, D.-h. Li, K.-m. Su, D.-j. Yang, B.-w. Cheng, *J. Mater. Chem. A* **2017**, *5*, 11340; d) G. Ren, X. Lu, Y. Li, Y. Zhu, L. Dai, L. Jiang, *ACS Appl. Mater. Interfaces* **2016**, *8*, 4118.
- [224] Q. Niu, B. Chen, J. Guo, J. Nie, X. Guo, G. Ma, *Nanomicro Lett.* **2019**, *11*, 8.
- [225] a) C.-Z. Yuan, S.-L. Zhong, Y.-F. Jiang, Z. K. Yang, Z.-W. Zhao, S.-J. Zhao, N. Jiang, A.-W. Xu, *J. Mater. Chem. A* **2017**, *5*, 10561; b) E. Hu, X.-Y. Yu, F. Chen, Y. Wu, Y. Hu, X. W. Lou, *Adv. Energy Mater.* **2018**, *8*, 1702476; c) J. Li, G. Liu, B. Liu, Z. Min, D. Qian, J. Jiang, J. Li, *Int. J. Hydrogen Energy* **2018**, *43*, 1365.
- [226] Y. Zhong, X. Xu, W. Wang, Z. Shao, *Batteries & Supercaps*, *0*.
- [227] a) J. Xiao, C. Chen, J. Xi, Y. Xu, F. Xiao, S. Wang, S. Yang, *Nanoscale* **2015**, *7*, 7056; b) G. Wu, N. H. Mack, W. Gao, S. Ma, R. Zhong, J. Han, J. K. Baldwin, P. Zelenay, *ACS Nano* **2012**, *6*, 9764.
- [228] a) B. Li, X. Ge, F. W. T. Goh, T. S. A. Hor, D. Geng, G. Du, Z. Liu, J. Zhang, X. Liu, Y. Zong, *Nanoscale* **2015**, *7*, 1830; b) Y. Su, Y. Zhu, H. Jiang, J. Shen, X. Yang, W. Zou, J. Chen, C. Li, *Nanoscale* **2014**, *6*, 15080; c) H. Yu, L. Shang, T. Bian, R. Shi, G. I. N. Waterhouse, Y. Zhao, C. Zhou, L.-Z. Wu, C.-H. Tung, T. Zhang, *Adv. Mater.* **2016**, *28*, 5080; d) W. Xia, R. Zou, L. An, D. Xia, S. Guo, *Energy Environ. Sci.* **2015**, *8*, 568.
- [229] J. Zhang, C. Wu, M. Huang, Y. Zhao, J. Li, L. Guan, *ChemCatChem* **2018**, *10*, 1336.
- [230] a) B. Y. Xia, Y. Yan, N. Li, H. B. Wu, X. W. Lou, X. Wang, *Nat. Energy* **2016**, *1*, 15006; b) E. Zhang, Y. Xie, S. Ci, J. Jia, P. Cai, L. Yi, Z. Wen, *J. Mater. Chem. A* **2016**, *4*, 17288; c) Z. Tao, T. Wang, X. Wang, J. Zheng, X. Li, *ACS Appl. Mater. Interfaces* **2016**, *8*, 35390; d) W. Zhou, J. Lu, K. Zhou, L. Yang, Y. Ke, Z. Tang, S. Chen, *Nano Energy* **2016**, *28*, 143.
- [231] Y. Guo, J. Tang, H. Qian, Z. Wang, Y. Yamauchi, *Chem. Mater.* **2017**, *29*, 5566.
- [232] a) S. Gao, H. Chen, Y. Liu, G.-D. Li, R. Gao, X. Zou, *Inorganic Chemistry Frontiers* **2019**, *6*, 940; b) L. Huang, D. Chen, G. Luo, Y. R. Lu, C. Chen, Y. Zou, C. L. Dong, Y. Li, S. Wang, *Adv. Mater.* **2019**, *31*, 1901439.

- [233] a) Y. S. Cheng, M. Ling, B. B. Jiang, F. H. Wu, Z. H. Zhao, X. N. Li, P. F. He, X. W. Wei, *ChemElectroChem* **2019**, *6*, 748; b) Y. Gong, L. Wang, H. Xiong, M. Shao, L. Xu, A. Xie, S. Zhuang, Y. Tang, X. Yang, Y. Chen, *J. Mater. Chem. A* **2019**, *7*, 13671.
- [234] D. Yu, K. Goh, H. Wang, L. Wei, W. Jiang, Q. Zhang, L. Dai, Y. Chen, *Nat. Nanotechnol.* **2014**, *9*, 555.
- [235] K. Sakaushi, A. Lyalin, S. Tominaka, T. Taketsugu, K. Uosaki, *ACS nano* **2017**, *11*, 1770.
- [236] Y. Li, W. Zhou, H. Wang, L. Xie, Y. Liang, F. Wei, J.-C. Idrobo, S. J. Pennycook, H. Dai, *Nat. Nanotechnol.* **2012**, *7*, 394.
- [237] S. Ishihara, J. Labuta, W. Van Rossom, D. Ishikawa, K. Minami, J. P. Hill, K. Ariga, *Phys. Chem. Chem. Phys.* **2014**, *16*, 9713.
- [238] a) Z.-D. Huang, Z. Gong, Q. Kang, Y. Fang, X.-S. Yang, R. Liu, X. Lin, X. Feng, Y. Ma, D. Wang, **2017**, *1*, 1975; b) G. Huang, F. Zhang, X. Du, Y. Qin, D. Yin, L. Wang, *ACS nano* **2015**, *9*, 1592; c) X. Xu, M. Wang, Y. Liu, T. Lu, L. Pan, *J. Mater. Chem. A* **2016**, *4*, 5467.
- [239] a) W. Zhang, Z.-Y. Wu, H.-L. Jiang, S.-H. Yu, *J. Am. Chem. Soc.* **2014**, *136*, 14385; b) Z. Li, M. Shao, L. Zhou, R. Zhang, C. Zhang, M. Wei, D. G. Evans, X. Duan, *Adv. Mater.* **2016**, *28*, 2337; c) J. Wei, Y. Hu, Y. Liang, B. Kong, J. Zhang, J. Song, Q. Bao, G. P. Simon, S. P. Jiang, H. Wang, *Adv. Funct. Mater.* **2015**, *25*, 5768; d) X. Wang, Q. Weng, Y. Yang, Y. Bando, D. Golberg, *Chem. Soc. Rev.* **2016**, *45*, 4042.
- [240] a) Y. Liang, Y. Li, H. Wang, J. Zhou, J. Wang, T. Regier, H. Dai, *Nat. Mater.* **2011**, *10*, 780; b) Y. Cao, Z. Wei, J. He, J. Zang, Q. Zhang, M. Zheng, Q. Dong, *Energy Environ. Sci.* **2012**, *5*, 9765; c) T. Y. Ma, S. Dai, M. Jaroniec, S. Z. Qiao, *J. Am. Chem. Soc.* **2014**, *136*, 13925.
- [241] Z. Zhang, Y. Tan, T. Zeng, L. Yu, R. Chen, N. Cheng, S. Mu, X. Sun, *Nano Res.* **2020**.
- [242] a) P. Moni, S. Hyun, A. Vignesh, S. Shanmugam, *Chem. Commun.* **2017**, *53*, 7836; b) C. Tang, H.-S. Wang, H.-F. Wang, Q. Zhang, G.-L. Tian, J.-Q. Nie, F. Wei, *Adv. Mater.* **2015**, *27*, 4516.
- [243] a) P. Wu, S. Cheng, M. Yao, L. Yang, Y. Zhu, P. Liu, O. Xing, J. Zhou, M. Wang, H. Luo, M. Liu, *Adv. Funct. Mater.* **2017**, *27*, 1702160; b) J. Shi, K. Lei, W. Sun, F. Li, F. Cheng, J. Chen, *Nano Res.* **2017**, *10*, 3836.
- [244] W. Wang, L. Kuai, W. Cao, M. Huttula, S. Ollikkala, T. Ahopelto, A.-P. Honkanen, S. Huotari, M. Yu, B. Geng, *Angew. Chem. Int. Ed.* **2017**, *56*, 14977.
- [245] J. Tan, T. Thomas, J. Liu, L. Yang, L. Pan, R. Cao, H. Shen, J. Wang, J. Liu, M. Yang, *Chem. Eng. J.* **2020**, *395*, 125151.
- [246] Y. Li, Z. Yin, M. Cui, S. Chen, T. Ma, *Mater. Today Energy* **2020**, *18*, 100565.
- [247] H. Jin, H. Zhou, P. Ji, C. Zhang, J. Luo, W. Zeng, C. Hu, D. He, S. Mu, *Nano Res.* **2020**, *13*, 818.
- [248] A. Sivanantham, P. Ganesan, S. Shanmugam, *Appl. Catal. B* **2018**, *237*, 1148.

Biographies of the authors



Mr. Yasir Arafat is currently pursuing his PhD degree in Chemical Engineering at Curtin University, Australia. His research interests include the fabrication of functional materials for the energy conversion and energy storage systems, viz., reforming reactions, Zn-air batteries, all-solid-state lithium batteries. Currently, the main focus of his research is the development of porous carbon, metal organic frameworks (MOFs), perovskites and their composites for the energy storage systems and deciphering their role in enhancing the performance.



Dr. Muhammad Rizwan Azhar received his PhD degree in Chemical Engineering from Curtin University in 2018. After graduation joined Edith Cowan University as Research Fellow and currently working on fundamental applied research projects on Water-Energy Nexus. His current research focuses on synthesis of Metal Organic Frameworks (MOFs), porous carbons, perovskite/MOFs composite for water treatment and energy applications. He has keen interest in integrating academic research into product/process oriented outcomes through collaborations with industry and government agencies.



Mr. Yijun Zhong is currently a PhD candidate at Curtin University, Australia. His research focuses on developing functional materials for high-efficient energy storage, e.g., lithium/sodium-ion batteries, lithium-sulfur batteries, and zinc-based batteries. His primary interests lie in understanding the effect of structure, composition, and morphology on catalytic and electrochemical properties of these materials.

This article is protected by copyright. All rights reserved.



Prof. Moses Tade is a John Curtin Distinguished Professor in Chemical Engineering at Curtin University. He has reputation nationally and worldwide for his research in chemical engineering and specifically in process systems engineering (PSE). He has significantly contributed to bridging the gap between theoretical work and industrial practice of PSE over an extensive academic career. He has received substantial funding for his work from industry and the Australian Research Council; supervised over 60 PhD students, several Master students and postdocs; included in the Highly Cited Researcher Lists (Clarivate Web of Science, 2019 and 2020) in the Cross Discipline Research field.



Prof. Zongping Shao is a professor of chemical engineering at Curtin University, Australia and Nanjing Tech University, China. He obtained his PhD from Dalian Institute of Chemical Physics, China in 2000. He worked as a visiting scholar at Institut de Recherches Sur La Catalyse, CNRS, France and postdoc at California Institute of Technology, USA from 2000 till 2005. His research interests include mixed conducting membranes for oxygen permeation, solid oxide fuel cells, room-temperature electrocatalysts, advanced energy storage devices including lithium/sodium-(ion) batteries, metal-air batteries and supercapacitors, etc. He has published more than 650 international journal papers with a total citation of >36000 and an H-index of 89 (Google Scholar). He was selected

as one of the highly cited researchers (2014, 2017-2020) by Clarivate Analytics and as one of the highly cited Chinese researchers by Elsevier China (2015-2019).

Short text (ToC)

Zeolitic imidazolate frameworks (ZIFs), a subclass of metal organic frameworks have been emerged as a new generation of oxygen electrocatalysts for Zn-air batteries (ZABs). The desired functionalities into ZIFs have been further indoctrinated by materials tuning, morphological control, or by hybridization. Here, the recent advances of ZIFs as air electrodes for ZABs have been critically surveyed, the major challenges and future prospects are discussed.